論文 / 著書情報
Article / Book Information

題目(和文)	地球マントル中における沈み込んだ海洋地殻の密度と弾性
Title(English)	Density and elasticity of subducted oceanic crust in the Earth's mantle
著者(和文)	西原遊
Author(English)	Yu Nishihara
出典(和文)	学位:理学博士, 学位授与機関:東京工業大学, 報告番号:甲第5306号, 授与年月日:2003年3月26日, 学位の種別:課程博士, 審査員:
Citation(English)	Degree:Doctor of Science, Conferring organization: Tokyo Institute of Technology, Report number:甲第5306号, Conferred date:2003/3/26, Degree Type:Course doctor, Examiner:
学位種別(和文)	博士論文
Type(English)	Doctoral Thesis

Density and elasticity of subducted oceanic crust in the Earth's mantle

by

Yu Nishihara

Doctoral Thesis

Earth and Planetary Sciences, Tokyo Institute of Technology, 2-12-1 Ookayama, Meguroku, Tokyo 152-8551, Japan

E-mail: yuu@geo.titech.ac.jp
Tel: +81-3-5734-2338
Fax: +81-3-5734-3538

February, 2003

Abstract

From early stage of the Earth history (~4.5Ga), basaltic crust bas been generated at mid oceanic ridges and subducted as the upper most part of the oceanic plate into the deep mantle. If the production rate of the modern oceanic plates and the thickness of the basaltic crust are maintained through the Earth history, subducted basalt should be equal to ca. 10% of the mass of whole mantle. The basaltic material, which is rich in pyroxene and garnet components, should be the source of the most important chemical heterogeneity in the olivine-rich peridotitic Earth mantle. In order to clarify the behavior of the oceanic crust in the mantle, we investigated density and elasticity of the oceanic crust and ambient mantle at high-pressure and high-temperature.

Omphacitic clinopyroxene, which consists essentially of solid solution of a diopside and jadeite, is the major mineral phase in subducted oceanic crust at 3–15 GPa. In chapter 1, thermal equation of state of eclogitic omphacite were determined by in situ X-ray diffraction experiments up to 10 GPa and 1000 K using the MAX-III multi-anvil press of KEK. The derived elastic parameters are generally consistent with the interpolations from those for end-member clinopyroxenes.

In chapters 2 and 3, thermal equation of state of $(Mg_{0.91}Fe_{0.09})_2SiO_4$ ringwoodite and majorite with MORB composition were determined by in situ X-ray diffraction experiments up to 21 GPa and 1273 K using SPEED-1500 multi-anvil press of SPring-8. These minerals are the most dominant phases in the mantle transition zone in pyrolitic mantle and the oceanic crust, respectively. The derived thermoelastic parameters for $(Mg_{0.91}Fe_{0.09})_2SiO_4$ ringwoodite are generally consistent with previous studies on Mg_2SiO_4 ringwoodite. However, as well as measurements at 0 GPa, the present equation of state yields significantly higher thermal expansivity than that derived by diamond anvil experiments on Mg_2SiO_4 ringwoodite to 30 GPa and 700 K. The derived thermoelastic parameters for MORB majorite are very similar to that of pyrope.

In chapter 4, the density and seismic velocities of the oceanic crust and ambient mantle up to 2900 km depth condition were calculated by using previously reported phase equilibrium data of MORB (for the oceanic crust) and pyrolite (for the ambient mantle) and the newly determined thermoelastic parameters of related minerals. Behavior of the oceanic crust entrained within mantle plume is considered by calculation base on Stokes' law using the derived densities. At the depths of ~1400–2100 km, P- and S-wave velocities of the oceanic crust show drastic decrease due to the second-order transformation of stishovite (rutile-type to $CaCl_2$-type). The expected low velocity of oceanic crust is consistent with the low velocity of the recently reported seismic scattering bodies in the mid lower mantle.

Contents

Chapter 1
Thermal equation of state of omphacite

Abstract

In situ synchrotron X-ray diffraction experiments were conducted using the MAX-III multi-anvil press of KEK on an omphacite ($Di_{63}Jd_{37}$), for which Di =$Ca(Mg,Fe)Si_2O_6$ and Jd = $NaAlSi_2O_6$. Pressure-volume-temperature data were collected at up to 10 GPa and 1000 K. A fit to the high-temperature Birch-Murnaghan equation of state yielded an isothermal bulk modulus K_{T0} = 126(1) GPa, an assumed pressure derivative of the bulk modulus K'_T = 4.0, a temperature derivative of the bulk modulus $(\partial K_T/\partial T)_P$ = –0.015(4) GPa K^{-1}, and a volumetric thermal expansivity $\alpha = 2.2(1) \times 10^{-5}$ K^{-1}, when the equation of state of NaCl by Brown (1999) is adopted for the pressure scale. The derived K_{T0} value is consistent with the linear interpolations from K_{T0} values for diopside and jadeite in the literature.

1-1 Introduction

Subducted mid oceanic ridge basalt (MORB), which is rich in components of pyroxene and garnet, may be the source of the most important chemical heterogeneity in the olivine-rich Earth's mantle. It is well understood that the MORB component exists as eclogite at pressure conditions of 3–15 GPa (e.g. Irifune et al., 1986). Omphacitic clinopyroxene, which consists essentially of solid solution of a diopside ($CaMgSi_2O_6$) and jadeite ($NaAlSi_2O_6$), is the major mineral phase in eclogite. Knowledge of the physical properties of omphacite is very important in clarifying the behavior of subducted MORB in the deep mantle.

Some experimental results have been reported for density changes of omphacites at high-temperature or high-pressure (McCormick et al., 1989; Pavese et al., 2000, 2001). McCormick et al. (1989) conducted room-temperature compression experiments to 6 GPa with the diamond

anvil cell using a liquid pressure medium on both vacancy-rich and vacancy-poor natural omphacites, and Pavese et al. (2001) reported similar experiments to 13 GPa on a *P2*/*n*-omphacite. Pavese et al. (2000) recorded thermal expansive properties on the same *P2*/*n*-omphacite that was used in Pavese et al. (2001). Thermal equation of states on some end-member clinopyroxenes have also been investigated (e.g. diopside; Zhao et al., 1998, jadeite; Zhao et al., 1997). However, simultaneous in situ measurements of thermoelastic properties of omphacite at high-pressure and high-temperature are still needed to derive complete equation of state for this mineral.

In this study, pressure (*P*)-volume (*V*)-temperature (*T*) relations of synthetic omphacite are measured at pressure and temperature conditions up to 10 GPa and 1000 K with synchrotron radiation, and the thermal equation of state was determined. The results are compared to previously reported thermoelastic parameters of omphacites and end-member pyroxenes.

1-2 Experimental procedures

Samples

Based on the results of the previous phase equilibrium experiments on the MORB composition, we synthesized omphacite to have an appropriate chemical composition for an eclogitic clinopyroxene. Chemical compositions of clinopyroxene in MORB at 5 GPa and 1773 K (Aoki and Takahashi, 2002), and at 5.6 GPa and 1473 K (Irifune et al., 1986) are shown in Table 1-1. Although the experimental conditions and starting compositions are similar, compositions of these two clinopyroxenes significantly differ in SiO_2 and Al_2O_3. This may be due to the different states of the starting materials (dried natural MORB in Aoki and Takahashi, 2002 vs. glass in Irifune et al., 1986). Reagents were mixed to match the former composition. Trace elements were ignored and reagents of SiO_2, Al_2O_3, Fe_2O_3, MgO, $CaCO_3$ and Na_2CO_3 were used. The mixture was ground and heated slowly from 873 to 1173 K and kept at 1173 K for more than 12 hours for decarbonation. The decarbonated sample was then melted for 10 min at 1622 K at

the fayalite-magnetite-quartz buffer in a one atmosphere furnace. The quenched glass was confirmed to be homogeneous by microprobe analysis. Omphacite was synthesized from the glass by using a 1000-ton multi-anvil press SPI-1000 at the Magma Factory, Tokyo Institute of Technology. The glass was enclosed in a Re foil capsule (3.2 mm in diameter, 3.4 mm in length), and experimental conditions were P = 5 GPa, T = 1773 K and t = 30 min. Experimental techniques and the cell assembly used in the synthesis experiments are similar to those of Takahashi et al. (1993) and Tsuruta and Takahashi (1998).

Chemical analyses were made with a JEOL-8800 microprobe. Accelerating voltage and beam current of 15 kV and 12 nA, respectively, were used with counting times of 10 s on the peak and 5 s on the background on either side of the peak. Standards used were: SiO_2-wollastonite, Al_2O_3-crundum, FeO-hematite, MgO-periclase, CaO-wollastonite, Na_2O-natural albite. Microprobe observation showed that most of the recovered sample consisted of omphacite, although minor amounts of garnet and coesite were also identified. Weight ratios of omphacite, garnet and coesite were calculated to be 87%, 10% and 4%, respectively, on the basis of mass balance equations. Chemical composition of the synthesized omphacite is listed in Table 1-2. The omphacite has lower Al_2O_3 and FeO contents than the model clinopyroxene (Aoki and Takahashi, 2002, Table 1-1). This pyroxene contains relatively high content of Ca-Eskola end-member (9 mol% $Ca_{0.5}\square_{0.5}AlSi_2O_6$). After the *P*-*V*-*T* experiments, chemical compositions of the omphacites were examined, and no changes were detected.

Angular dispersive X-ray powder diffraction with CrKα radiation was carried out for the synthesized sample at ambient conditions. The results also showed the existence of minor garnet and coesite with omphacite. The unit cell parameters of the omphacite were calculated to be a = 9.607(2) Å, b = 8.774(2) Å, c = 5.254(2) Å, β = 106.85(4)° and V = 423.8(2) Å^3 from the positions of 20 diffraction peaks. It is well known that the order-disorder phase transition occurs in omphacite (e.g. Carpenter, 1980). It is quite difficult to distinguish between *C*2/*c*- and *P*2/*n*–

omphacites from powder X-ray diffraction, because all the reflections due to ordering are very weak (Clark and Papike, 1968). *P*2/*n*-omphacite is stable only at low temperature (<~700 °C, Carpenter, 1980). Judged from its chemical composition and our synthesis conditions, the space group of our omphacite is *C*2/*c* rather than *P*2/*n*. These two structures are quite similar and the phase transition would have no significant effect on *P-V-T* data.

P-V-T experiments

P-V-T experiments were conducted using the MAX-Ⅲ multi-anvil apparatus installed at the synchrotron beam line (BL14C2) in the Photon Factory at the National Laboratory for High Energy Accelerator Research Organization, Tsukuba, Japan. Six sintered diamond anvils (4 × 4 mm^2 truncation size) were used for high-pressure generation. Fig. 1-1 shows the schematic cross section of the cell assembly. A cubic pressure medium (7 × 7 × 7 mm^3) made of a mixture of boron and epoxy resin (weight ratio 4:1) with tubular graphite heater was used. Powdered omphacite and a mixture of NaCl and BN (weight ratio 6:1) were packed into the BN sample chamber separately. Temperature was measured with a W5%Re-W26%Re thermocouple, and pressure was determined by the thermal equation of state of NaCl (Decker, 1971; Brown, 1999).

A solid-state detector connected to a multi-channel analyzer was used for data collection. The multi-channel analyzer was calibrated with the characteristic X-rays of Mo, Ag, Dy, Ta, Au and Bi. The diffracted X-rays from the sample were collected at fixed 2θ angle of ~6.0 ° by the energy dispersive method. The 2θ angle was calibrated by the unit cell volume of NaCl. The incident X-ray beam was collimated to 0.05 mm and 0.2 mm in the vertical and horizontal dimensions, respectively. Three thin slits between the sample and the detector, 0.05 and 0.2 mm in the vertical dimension and 0.5 mm in horizontal, were used for elimination of the diffracted X-rays from the pressure medium. The X-ray diffraction data were collected at the positions 0.2 mm above and below the thermocouple junction for the sample and the pressure marker, respectively.

Typical exposure times for collecting the diffraction patterns of the sample and pressure marker were 600 and 300 s, respectively. The fluctuation of temperature indicated by the thermocouple was within 5 K. Fig. 1-2 shows an example of the diffraction spectrum of omphacite. The unit cell parameters were calculated from peak positions by the least-squares technique. Because of overlapping of diffraction peaks from both omphacite and other materials, the number of reflections used was limited to 8–11 in this calculation. The use of 8 to 11 peaks to fix the lattice parameters of a monoclinic symmetry compound results a bit in an under-estimation of *a*, *b*, *c*, and β. Pressure was determined from observed cell volume of NaCl by using the pressure scales of Brown (1999) and Decker (1971). The cell volumes of NaCl were calculated from four diffraction lines; 200, 220, 222 and 400. The errors in the calculated pressures were estimated from the difference of calculated pressure from different peaks of NaCl. The estimated errors were 0.04 GPa on average, and 0.15 GPa at the maximum.

Two *P*-*V*-*T* runs (Run#1 and Run#2) were conducted. The sample was compressed to the desired pressure at room temperature and heated to the maximum temperature (1000 K) in order to release non-hydrostatic stress. The X-ray diffraction data of both the sample and the pressure marker were collected at fixed temperatures of 100 K intervals under constant ram load. After the data collection at room temperature, the sample was further compressed, and the heating and data collection cycle was repeated again. The procedure was repeated for up to 7 temperature excursions in two runs. Fig. 1-3 shows the *P*-*T* paths in the two experiments. In Fig. 1-3, pressure values calculated by the Brown (1999) equation of state (EOS) are indicated. Brown's EOS yields a revised pressure scale for NaCl proposed as an update to the 30-year-old work of Decker (1971). As mentioned by Brown (1999), the pressure differences between these two scales are larger at higher pressure and lower temperature. Although the pressure differences are not so large (<0.3 GPa), they affect significantly the derived EOS of omphacite. In this study, the pressure values based on the Brown's pressure scale are used after comparison with those based

on Decker's scale.

1-3 Results and discussion

Thermal equation of state

Unit cell parameters of omphacite at various *P-T* conditions are shown in Table 1-3. Only the data collected on cooling (and data at ambient conditions), which are considered to be closer to hydrostatic conditions, are listed in Table 1-3 and used in subsequent calculations. Fig. 1-4 shows the volume data measured at 300, 500, 700, 900 and 1000 K.

The high-temperature Birch-Murnaghan (HTBM) equation of state is often used to fit the *P-V-T* data (e.g. Funamori et al., 1996; Wang et al., 1998). The equation of state is given by the following expression:

$$P = 3/2K_T\left[\left(V_{0T}/V\right)^{7/3} - \left(V_{0T}/V\right)^{5/3}\right]\left\{1 + 3/4\left(K'_T - 4\right)\left[\left(V_{0T}/V\right)^{2/3} - 1\right]\right\} \quad (1)$$

where K_T, V_{0T}, V, and K'_T are the isothermal bulk modulus, zero-pressure volume, high-pressure volume and pressure derivative of K_T. Temperature effects for K_T and V_{0T} are expressed as follows:

$$K_T = K_{T0} + \left(\partial K_T/\partial T\right)_P\left(T - 300\right) \quad (2)$$

$$V_{0T} = V_0 \exp\left[\int_{300}^{T} \alpha \mathrm{d}T\right] \quad (3)$$

where $(\partial K_T/\partial T)_P$ and α are the temperature derivative of the bulk modulus and the volumetric thermal expansion at atmospheric pressure, respectively. The α, K'_T and $(\partial K_T/\partial T)_P$ are assumed to be constant. In the case of angle dispersive X-ray diffraction, the observed diffraction lines are

relatively sharp and the overlap of diffraction lines is not so heavy, compared with the case of energy dispersive X-ray diffraction. Thus, the V_{0T} value determined by the angle dispersive method is expected to be more accurate. In following calculations, V_{0T} is fixed to be the value determined by angle dispersive X-ray diffraction (V_{0T} = 423.8 Å^3).

The experimental *P*-*V*-*T* data (Table 1-3) were fitted to HTBM equation of state, and results are listed in Table 1-4. The fits without constraint on K'_T yielded relatively high values of K'_T ($K'_T \approx 7$). However, the limited pressure range and limited precision of volume data in our experiments prevent resolving the K'_T value confidently. We also calculated the equation of state by fixing K'_T to be 4 and 5. K'_T = 4 is the most common value for silicate minerals and corresponds to a second order Birch Murnaghan equation of state. Similar to this study, Zhao et al. (1997, 1998) conducted *P*-*V*-*T* experiments on jadeite and diopside, and their results showed $K'_T \approx 5$. For comparison with these previous studies, the K'_T was also fixed to be 5 in the calculation. The same calculations were carried out based on the two pressure scales for NaCl (Brown, 1999; Decker, 1971).

Calculated thermal expansivity α does not change significantly with the value chosen for K'_T. However, the calculated bulk modulus and its temperature derivative depend strongly on the assumed K'_T value. The tradeoff between K_{T0} and K'_T are indicated in Fig. 1-5. It is well recognized that the calculated K_{T0} value decreases with increasing K'_T. The $(\partial K_T/\partial T)_P$ also shows a significant co-relation with K'_T, and we could not constrain it strictly. Because Brown's scale calculates slightly higher pressure than Decker's scale, the bulk moduli based on Brown's scale are larger than those based on Decker's scale at the same K'_T. The thermal expansivity α does not change significantly with the choice of pressure scale. In Fig. 1-4, the isothermal compression curves calculated from the fitted thermoelastic parameters (Brown's pressure scale, K'_T = 4) are illustrated. The differences between the experimental results and calculated compression curves are generally within experimental uncertainties (error bars in Fig. 1-4).

Fig. 1-6 shows variations of the isothermal bulk modulus K_T for omphacite with temperature at K'_T = 4.0. Symbols show the calculated isothermal bulk moduli obtained by fitting well the data at each temperature to the Birch-Murnaghan equation of state. Lines are the results of fits to HTBM equation of state for all of the data. Decrease of K_T with increasing temperature is represented by linear expression. In Fig. 1-6, both data based on Brown (1999)'s scale and Decker (1971)'s scale are plotted. Because the differences of pressure values between these two pressure scales are smaller at higher temperatures, the difference of bulk modulus decreases with increasing temperature. As indicated in Table 1-4, this feature is expressed as larger absolute value of $(\partial K_T/\partial T)_P$ when Brown's scale is used.

Comparison with other pyroxenes

Elastic properties of pyroxenes have been investigated by some experimental methods. Most of the studies are based on X-ray diffraction (XRD) at high-pressure and Brillouin scattering at ambient conditions. By the XRD at high-*P*, the compression curve is obtained, and the isothermal bulk modulus and its pressure derivative can be determined. Mostly, the calculated bulk moduli and their pressure derivatives are highly dependent on each other because of the limited experimental pressure range and the precision of volume data as described for present results (Table 1-4 and Fig. 1-5). By the single-crystal Brillouin scattering, the elastic constants are derived, and the adiabatic bulk and shear moduli at ambient conditions can be determined. The relation between isothermal and adiabatic bulk moduli (K_T and K_S, respectively) is expressed as follows: $K_T = K_S/(1 + \alpha\gamma_G T)$ where α and γ_G are thermal expansivity and the Grüneisen parameter. Because the term $\alpha\gamma_G T$ is estimated to be ~0.01 for pyroxenes at 300 K and the difference between K_T and K_S at ambient conditions is similar in size to experimental uncertainties for bulk moduli, K_T and K_S, and are not distinguished in the following discussion.

As described above, the choice of pressure scale significantly affects the derived bulk

modulus in the high-*P* XRD studies. Most of previous studies are based on Decker (1971)'s NaCl pressure scale or on the ruby scale (e.g. Piermarini et al., 1975; Mao et al., 1986). The ruby scale is tied to the Decker scale since Piermarini et al. (1975) calibrated ruby fluorescence wavelength shifts against NaCl volumes determined by X-ray diffraction. The ultrahigh pressure ruby calibrations (e.g. Mao et al., 1986) use a functional representation that forces a match to the Piermarini et al.'s pressure derivative at low pressures. Thus, previous results on other pyroxenes are comparable with the present results based on Decker's scale.

The comparison of the bulk modulus at the ambient condition K_0 and its pressure derivative K' for some end-member pyroxenes (diopside; $CaMgSi_2O_6$, hedenbergite; $CaFeSi_2O_6$, jadeite; $NaAlSi_2O_6$ and orthoenstatite; $Mg_2Si_2O_6$) and omphacites is shown in Fig. 1-5. Data plotted in the left-hand box are the results from Brillouin scattering measurements and their K' are not determined. All the data in the right-hand box are the results from high-pressure XRD except for a datum of orthoenstatite (obtained by ultrasonic interferometry; Flesch et al., 1998). The stiffer sample would be plotted toward the upper right in the diagram. Othoenstatite, which has a different crystal structure, is characterized by relatively low K_0 and high K' values compared to monoclinic pyroxenes. Diopside and hedenbergite have similar compressibilities. The variation in the results shown by high-pressure XRD of diopside (Levien and Prewitt, 1981; McCormick et al. 1989; Zhang et al., 1997; Zhao et al., 1998) may show a tradeoff between K_0 and K'. Only two results of K_0 for jadeite are reported and they differ significantly (143(2) GPa, Brillouin scattering by Kandelin and Weidner, 1988b, 125(4) GPa at $K' = 5.0$, high-*P* XRD by Zhao et al., 1997). The reason for the disagreement is not clear. However, it can be concluded that jadeite is the most incompressible pyroxene end-member.

If we use $Ca(Mg,Fe)Si_2O_6$ and $(Mg,Fe)_2Si_2O_6$ as end-membes, alternative to $Ca_2Si_2O_6$, $Mg_2Si_2O_6$ and $Fe_2Si_2O_6$, the contents of both components in our omphacite are 47.8(27) and 10.3(16) mol%, respectively. In this case, the dominant components are $Ca(Mg,Fe)Si_2O_6$ and

$NaAlSi_2O_6$. The contents of Di + Jd are 76 mol% in the clinopyroxene solid solution, and Di and Jd represent $Ca(Mg,Fe)Si_2O_6$ and $NaAlSi_2O_6$, respectively. If we ignore the other components and normalize to 100%, composition of our omphacite can be expressed as $Di_{63}Jd_{37}$. Assuming a linear relationship between K_0 and composition, and using the results from Brillouin scattering on diopside (K_{S0} = 113(1) GPa; Levien et al., 1979) and jadeite (K_{S0} = 143(2) GPa; Kandelin and Weidner, 1988b) to interpolate the bulk modulus for $Di_{63}Jd_{37}$, one calculates $K_0 \approx 124$ GPa. The same interpolation by using the results from high-pressure and high-temperature XRD (diopside; K_{T0} = 109(4) GPa; Zhao et al., 1998, jadeite; K_{T0} = 125(4) GPa; Zhao et al., 1997) yields $K_0 \approx 115$ GPa. These are generally consistent with the results of the present experiments (see Table 1-4).

Omphacites in Fig. 1-5 are expressed as $Di_{24}Jd_{76}$ (OM1; vacancy-rich omphacite by McCormick et al., 1989, 75 mol% Di + Jd content), $Di_{34}Jd_{66}$ (OM2 and 3; McCormick et al., 1989 and Bhagat et al., 1992, 88 mol%) and $Di_{51}Jd_{49}$ (OM4; *P*2/*n*-omphacite by Pavese et al., 2001, 91 mol%). OM2 and OM3 have identical compositions.

McCormick et al. (1989) performed single crystal XRD experiments at high pressures on diopside, OM1 and OM2 by using a multiple crystal mount in diamond anvil cell. OM2 shows higher K_0 than OM1 in spite of its lower jadeite content. However, this is attributable to the higher Ca-Eskola ($Ca_{0.5}\square_{0.5}AlSi_2O_6$, vacancy-rich end-member) content (13 mol%) in OM1 (McCormick et al., 1989). It should be pointed out that their results (diopside; K_0 = 122(2) GPa, OM2; 139(4) GPa at K' = 4.0) show higher bulk moduli than those by Brillouin scattering on the same materials (diopside; Levien et al., 1979; OM3; Bhagat et al., 1992), systematically. The reason for the discrepancy in bulk modulus is unclear. As described in Bhagat at al. (1992), K_0 of OM3 is well explained by the interpolation from the results of the Brillouin scattering on diopside and jadeite. Similarly, K_0 of OM4 and the interpolation from the results of the high-pressure and high-temperature XRD shows fairly good consistency (Pavese et al., 2001).

Pavese et al. (2000) measured the thermal expansivity of an omphacite, which is the same

specimen as that used by Pavese et al. (2001) for high-*P* XRD (OM4), from 298 to 1273 K at ambient pressure. The results are α = 2.76(4) and 2.51(3) × 10^{-5} K^{-1} upon heating and on cooling, respectively, and are consistent with the results of present experiments (Table 1-4).

Our data provide a direct assessment of thermoelastic behaviour of omphacite at simultaneous high-pressure and high-temperature. Although our opmphacite contains some minor end-member components (including vacancy-bearing $Ca_{0.5}\square_{0.5}AlSi_2O_6$ end-member) other than diopside and jadeite, the results are generally consistent with the linear interpolation from thermoelastic parameter of diopside and jadeite in the literature.

Acknowledgements

I am grateful to Prof. Eiichi Takahashi for his valuable advice, continuing encouragement, discussion and review of this manuscript. I thank T. Kikegawa, N. Nishiyama, T. Yagi, K. Kusaba and I. Aoki for their advice on experimental techniques, and K. Matsukage, T. Iguchi, K. Nakayama, M. Shirasaka, Y. Tange, K. Hirose and K. Kawamura for their helpful support for in situ X-ray diffraction experiments. I also thank T. Tsuchiya for useful discussions and T.L. Wright for reading the manuscript. Critical reviews by Y. Wang and A. Pavese were helpful to improve the manuscript. The in situ X-ray diffraction experiments were performed at the National Laboratory for High Energy Accelerator Research Organization (#00G030). Y.N. is grateful for the Research Fellowships of the Japan Society of the Promotion of Science for Young Scientists.

References

Aoki, I. and Takahashi, E. (2002) Density of MORB eclogite in the upper mantle. Physics of the Earth and Planetary Interior (submitted).

Bhagat, S.S., Bass, J.D., and Smyth, J.R. (1992) Single-crystal elastic properties of omphacite-C2/c by Brillouin spectroscopy. Journal of Geophysical Research, 97, 6843–6848.

Brown, J.M. (1999) The NaCl pressure standard. Journal of Applied Physics, 86, 5801–5808.

Carpenter, M.A. (1980) Mechanisms of exsolution in sodic pyroxenes. Contributions to Mineralogy and Petrology, 71, 289–300.

Clark , J.R. and Papike J.J. (1968) Crystal-chemical characterization of omphacites. American Mineralogist, 53, 840–868.

Decker, D.L. (1971) High-pressure equation of state for NaCl, KCl, and CsCl. Journal of Applied Physics, 42, 3239–3244.

Flesch, L.M., Li, B., and Liebermann, R.C. (1998) Sound velocities of polycrystalline $MgSiO_3$-orthopyroxene to 10 GPa at room temperature. American Mineralogist, 83, 444–450.

Funamori, N., Yagi, T., Utsumi, W., Kondo, T., Uchida, T., and Funamori, M. (1996) Thermoelastic properties of $MgSiO_3$ perovskite determined by in situ X ray observations up to 30 GPa and 2000 K. Journal of Geophysical Research, 101, 8257–8269.

Irifune, T., Sekine, T., Ringwood, A.E., and Hibberson, W.O. (1986) The eclogite-garnetite transformation at high pressure and some geophysical implications. Earth and Planetary Science Letters, 77, 245–256.

Kandelin, J. and Weidner, D.J. (1988a) Elastic properties of hedenbergite. Journal of Geophysical Research, 93, 1063–1072.

————————(1988b) The single-crystal elastic properties of jadeite. Physics of the Earth and Planetary Interiors, 50, 251–260.

Levien, L. and Prewitt, C.T. (1981) High-pressure structural study of diopside. American Mineralogist, 66, 315–323.

Levien, L., Weidner, D.J., and Prewitt, C.T. (1979) Elasticity of diopside. Physics and Chemistry of Minerals, 4, 105–113.

Mao, H.K., Xu, J., and Bell, P.M. (1986) Calibration of the ruby pressure gauge to 800 kbar under quasi-hydrostatic conditions. Journal of Geophysical Research, 91, 4673–4676.

McCormick, T.C., Hazen, R.M., and Angel, R.J. (1989) Compressibility of omphacite to 60 kbar: Role of vacancies. American Mineralogist, 74, 1287–1292.

Pavese, A., Bocchio, R., and Ivaldi, G. (2000) In situ high temperature single crystal X-ray diffraction study of a natural omphacite. Mineralogical Magazine, 64, 983–993.

Pavese, A., Diella, V., Levy, D., and Hanfland, M. (2001) Synchrotron X-ray powder diffraction study of natural P2/n-omphacites at high-pressure conditions. Physics and Chemistry of Minerals, 28, 9–16.

Piermarini, G.J., Block, S., Barnett, J.D., and Forman, R.A. (1975) Calibration of the pressure dependence of the R_1 ruby fluorescence line to 195 kbar. Journal of Applied Physics, 46, 2774–2780.

Takahashi, E., Shimazaki, T., Tsuzaki, Y., and Yoshida, H. (1993) Melting study of a peridotite KLB-1 to 6.5 GPa, and the origin of basaltic magmas. Philosophical Transactions of the Royal Society of London A, 342, 105–120.

Tsuruta, K. and Takahashi, E. (1998) Melting study of an alkali basalt JB-1 up to 12.5 GPa: behavior of potassium in the deep mantle. Physics of the Earth and Planetary Interiors, 107, 119–130.

Wang, Y., Weidner, D.J., Zhang, J., Gwanmesia, G.D., and Liebermann, R.C. (1998) Thermal equation of state of garnets along the pyrope-majorite join. Physics of the Earth and Planetary Interiors, 105, 59–71.

Weidner, D.J., Wang, H., and Ito, J. (1978) Elasticity of orthoenstatite. Physics of the Earth and Planetary Interiors, 17, P7–P13.

Zhang, L. and Hafner, S.S. (1992) High-pressure ^{57}Fe γ resonance and compressibility of $Ca(Fe,Mg)Si_2O_6$ clinopyroxenes. American Mineralogist, 77, 462–473.

Zhang, L., Ahsbahs, H., Hafner, S.S., and Kutoglu, A. (1997) Single-crystal compression and crystal structure of clinopyroxene up to 10 GPa. American Mineralogist, 82, 245–258.

Zhao, Y., Schiferl, D., and Shankland, T.J. (1995) A high P-T single-crystal X-ray diffraction study of thermoelasticity of $MgSiO_3$ orthoenstatite. Physics and Chemistry of Minerals, 22, 393–398.

Zhao, Y., Von Dreele, R.B., Shankland, T.J., Weidner, D.J., Zhang, J., Wang, Y., and Gasparik, T. (1997) Thermoelastic equation of state of jadeite $NaAlSi_2O_6$: An energy-dispersive Rietveld refinement study of low symmetry and multiple phases diffraction. Geophysical Research Letters, 24, 5–8.

Zhao, Y., Von Dreele, R.B., Zhang, J.Z., and Weidner, D.J. (1998) Thermoelastic equation of state of monoclinic pyroxene: $CaMgSi_2O_6$ diopside. Review of High Pressure Science and Technology, 7, 25–27.

Table 1-1. Chemical composition of clinopyroxenes in MORB

wt%	Aoki*	Irifune†
SiO_2	53.92	51.60
TiO_2	0.50	0.70
Al_2O_3	12.53	15.71
FeO	6.03	5.36
MnO	0.06	–
MgO	9.33	8.73
CaO	13.58	14.37
Na_2O	3.39	3.20
K_2O	0.04	–
P_2O_5	0.08	–
Total	99.46	99.67

* Clinopyroxene in MORB composition at 5 GPa and 1773 K (Aoki and Takahashi, 2002).

† Clinopyroxene in MORB composition at 5.6 GPa and 1473 K (Irifune et al., 1986).

Table 1-2. Chemical composition of omphacite

Chemical Analysis			Pyroxene End Members	
Cation	Weight Percent Oxide	Number of Cations (O = 6)	Component	Mole Percent
Si	55.08(47)	1.954(12)	$NaAlSi_2O_6$	28.4(19)
Al	11.12(46)	0.465(19)	$CaAl_2SiO_6$	4.6(12)
Fe	4.52(40)	0.134(12)	$Ca_{0.5}\square_{0.5}AlSiO_6$	8.9(37)
Mg	10.40(25)	0.550(13)	$Ca_2Si_2O_6$	23.9(13)
Ca	14.94(40)	0.568(15)	$Mg_2Si_2O_6$	27.5(7)
Na	4.13(28)	0.284(19)	$Fe_2Si_2O_6$	6.7(6)
Total	100.18	3.956		100.0

Note: Estimated standard deviations in parentheses are based on 16 analyses.

Table 1-3. Unit cell parameters of omphacite at various P-T conditions

P_B* (GPa)	P_D† (GPa)	T (K)	a (Å)	b (Å)	c (Å)	β (°)	V (Å^3)
Run #1							
0.00	0.00	294	9.596(7)	8.765(2)	5.277(8)	106.89(8)	424.7(7)
4.05	4.05	1000	9.553(2)	8.721(4)	5.214(4)	106.62(2)	416.2(4)
3.94	3.94	900	9.546(4)	8.718(7)	5.211(7)	106.63(4)	415.5(7)
3.82	3.81	800	9.546(3)	8.711(5)	5.214(5)	106.64(3)	415.4(5)
3.70	3.69	700	9.536(2)	8.709(5)	5.213(4)	106.60(2)	414.9(4)
3.55	3.52	600	9.533(4)	8.703(7)	5.209(7)	106.59(4)	414.2(7)
3.45	3.41	500	9.530(3)	8.699(6)	5.211(5)	106.58(3)	414.1(5)
3.36	3.29	400	9.527(3)	8.690(6)	5.210(6)	106.55(3)	413.5(6)
3.32	3.23	303	9.526(9)	8.687(18)	5.215(17)	106.67(9)	413.4(17)
6.61	6.58	1000	9.485(9)	8.681(5)	5.174(18)	106.52(14)	408.5(14)
6.49	6.45	900	9.475(6)	8.675(3)	5.172(11)	106.37(9)	407.9(9)
6.40	6.35	800	9.483(8)	8.667(5)	5.171(15)	106.45(12)	407.6(12)
6.27	6.21	700	9.469(6)	8.667(4)	5.168(12)	106.36(10)	407.0(10)
6.15	6.07	600	9.466(6)	8.658(3)	5.171(11)	106.36(9)	406.7(9)
6.05	5.94	500	9.465(3)	8.650(2)	5.172(6)	106.26(4)	406.5(5)
5.98	5.85	400	9.470(4)	8.649(2)	5.168(8)	106.31(6)	406.2(7)
5.94	5.77	303	9.463(5)	8.647(3)	5.166(9)	106.29(7)	405.7(7)
7.96	7.91	1000	9.456(7)	8.650(4)	5.155(13)	106.38(10)	404.6(11)
7.78	7.72	900	9.450(4)	8.641(2)	5.161(7)	106.28(6)	404.5(6)
7.66	7.58	800	9.445(5)	8.639(3)	5.157(9)	106.26(7)	404.0(8)
7.52	7.42	700	9.446(4)	8.633(2)	5.159(7)	106.23(5)	403.9(6)
7.38	7.27	600	9.449(4)	8.626(3)	5.158(8)	106.29(7)	403.5(7)
7.23	7.09	500	9.441(4)	8.625(2)	5.154(7)	106.18(5)	403.1(6)
7.17	7.00	400	9.437(3)	8.616(2)	5.157(6)	106.14(4)	402.8(5)
7.11	6.89	303	9.441(4)	8.611(2)	5.155(7)	106.18(5)	402.5(6)
9.31	9.23	1000	9.441(6)	8.603(3)	5.155(11)	106.38(9)	401.7(9)
9.08	8.99	900	9.432(5)	8.604(3)	5.150(9)	106.23(8)	401.3(7)
8.95	8.84	800	9.429(4)	8.600(2)	5.150(8)	106.14(6)	401.2(6)
8.77	8.64	700	9.420(5)	8.594(3)	5.154(9)	106.05(8)	400.9(8)
8.66	8.51	600	9.418(4)	8.584(2)	5.165(8)	106.18(7)	401.1(7)
8.55	8.37	500	9.421(3)	8.592(2)	5.148(6)	106.16(5)	400.2(5)
8.44	8.23	400	9.418(4)	8.583(2)	5.155(7)	106.20(6)	400.2(6)
8.40	8.15	302	9.421(4)	8.582(2)	5.149(8)	106.20(7)	399.8(6)
10.15	10.06	1000	9.425(3)	8.590(2)	5.142(5)	106.29(4)	399.6(4)
9.92	9.81	900	9.416(3)	8.590(2)	5.144(6)	106.19(4)	399.6(4)
9.67	9.54	800	9.426(4)	8.583(2)	5.152(8)	106.25(6)	400.2(6)
9.53	9.38	700	9.423(5)	8.578(3)	5.150(10)	106.27(7)	399.6(8)
9.41	9.23	600	9.419(5)	8.574(3)	5.149(10)	106.25(8)	399.2(8)
9.34	9.13	500	9.424(6)	8.569(3)	5.148(11)	106.27(9)	399.0(9)
9.22	8.98	400	9.417(6)	8.568(3)	5.143(11)	106.24(9)	398.4(9)
9.20	8.92	302	9.419(5)	8.568(3)	5.131(11)	106.23(8)	397.6(9)

0.00	0.00	299	9.603(3)	8.770(1)	5.259(4)	106.87(4)	423.8(4)
Run #2							
0.00	0.00	300	9.603(3)	8.767(2)	5.271(6)	106.81(5)	424.8(5)
3.06	3.07	1000	9.569(2)	8.763(1)	5.239(3)	106.62(2)	421.0(3)
2.86	2.87	900	9.565(2)	8.758(1)	5.233(4)	106.57(3)	420.2(3)
2.76	2.77	800	9.560(2)	8.750(1)	5.236(3)	106.59(2)	419.7(3)
2.67	2.67	700	9.562(1)	8.745(0)	5.233(2)	106.62(1)	419.3(1)
2.56	2.55	600	9.557(1)	8.742(1)	5.230(2)	106.60(1)	418.7(2)
2.50	2.47	500	9.552(2)	8.734(1)	5.230(3)	106.58(2)	418.2(2)
2.44	2.40	400	9.541(1)	8.731(1)	5.229(2)	106.56(2)	417.6(2)
2.40	2.34	303	9.541(1)	8.723(1)	5.230(2)	106.57(2)	417.2(2)
5.56	5.55	1000	9.506(4)	8.704(2)	5.192(8)	106.38(6)	412.2(7)
5.42	5.40	900	9.505(4)	8.698(2)	5.191(8)	106.38(6)	411.7(7)
5.32	5.30	800	9.501(5)	8.692(3)	5.190(10)	106.38(7)	411.2(8)
5.20	5.16	700	9.502(5)	8.690(3)	5.186(9)	106.39(7)	410.8(7)
5.07	5.01	600	9.499(4)	8.685(2)	5.185(8)	106.37(6)	410.4(6)
4.95	4.88	500	9.500(5)	8.680(3)	5.186(10)	106.43(8)	410.1(8)
4.89	4.79	400	9.498(7)	8.675(4)	5.188(13)	106.48(10)	409.9(11)
4.84	4.70	303	9.487(5)	8.673(3)	5.188(10)	106.40(7)	409.5(8)
0.02	0.02	300	9.603(3)	8.767(2)	5.271(6)	106.81(5)	424.8(5)

* Pressure scale by Brown (1999).

† Pressure scale by Decker (1971).

Table 1-4. Thermoelastic parameters of omphacite

Parameters						
Pressure scale	Brown	Brown	Brown	Decker	Decker	Decker
K_{T0} (GPa)	117(4)	126(1)	123(1)	114(4)	123(1)	119(1)
K'_T	6.9(12)	[4]	[5]	6.7(11)	[4]	[5]
$(\partial K_T/\partial T)_P$ (GPa K^{-1})	–0.026(5)	–0.015(4)	–0.019(3)	–0.024(5)	–0.013(4)	–0.018(3)
$\alpha(10^{-5}$ $K^{-1})$	2.7(3)	2.2(1)	2.4(1)	2.8(3)	2.3(1)	2.5(1)

Note: V_{0T} is fixed to be 423.8 $Å^3$ in the calculation. Square brackets indicate fixed parameters in the fit.

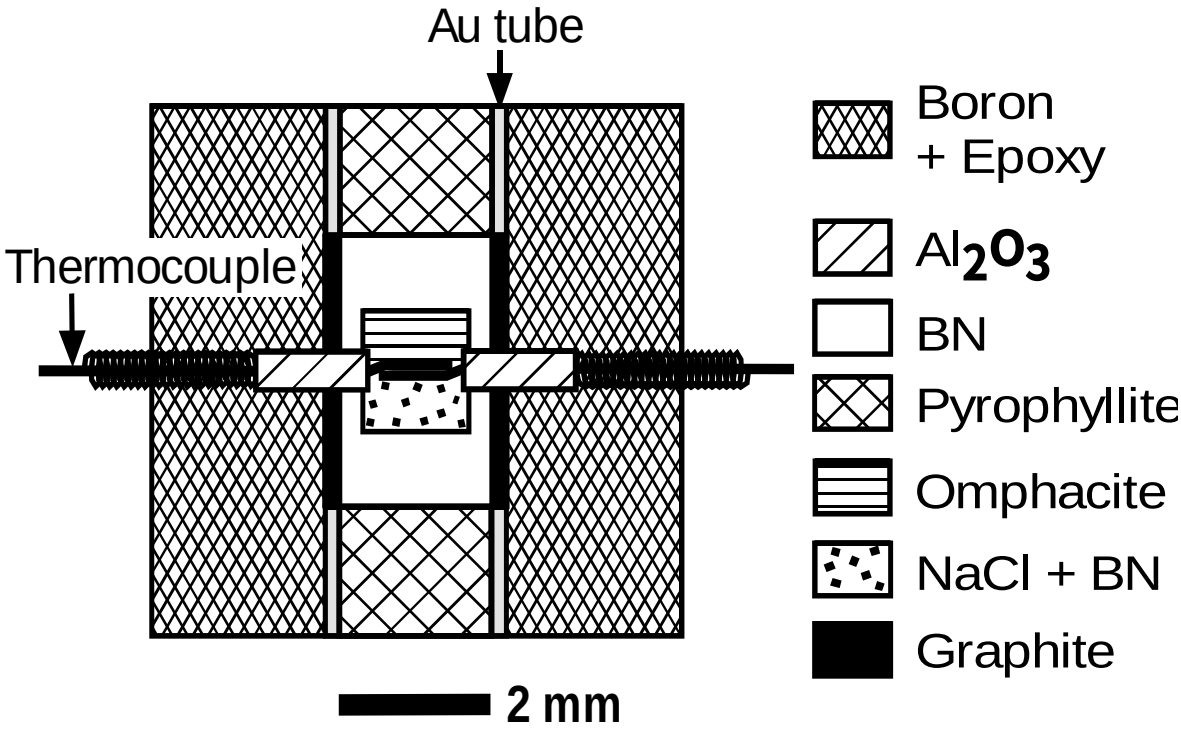

Fig. 1-1. Schematic cross section of the cell assembly.

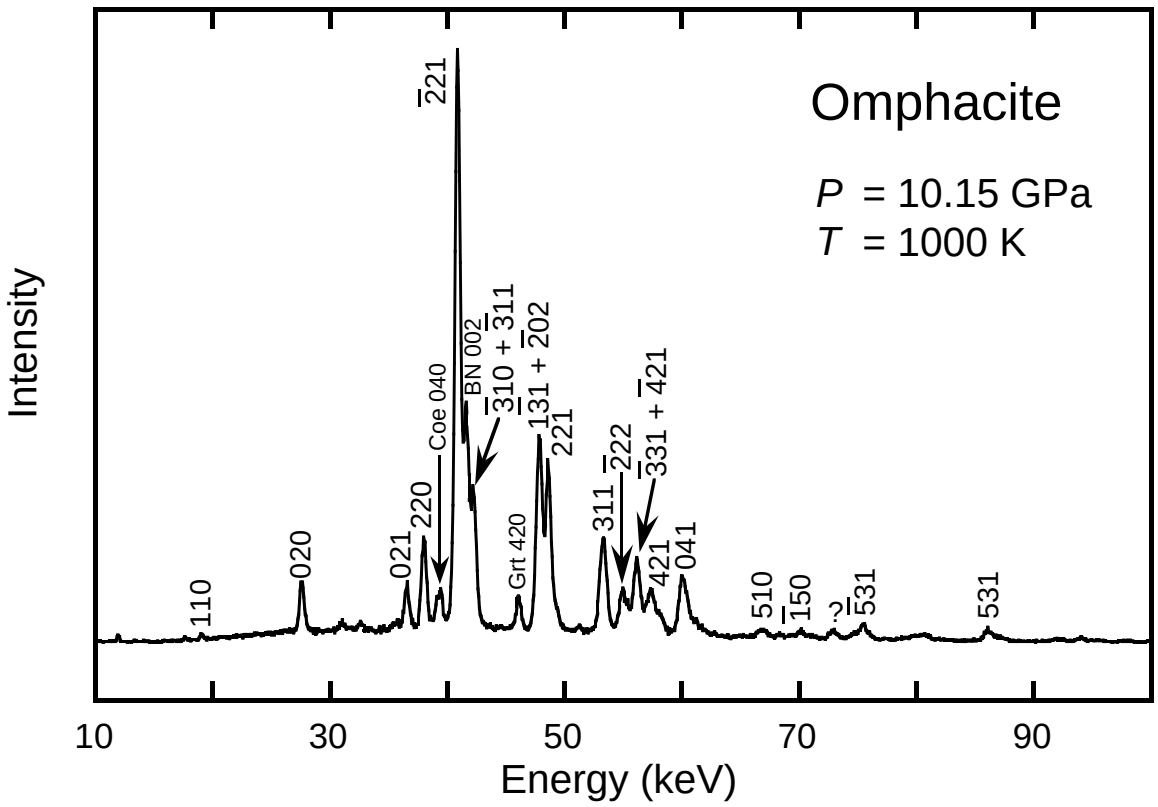

Fig. 1-2. Example of diffraction spectra ofomphacite at 10.15 GPa (Brown's scale) and 1000 K. Diffraction peaks for coesite (Coe) and garnet (Grt), which coexist with omphacite, and the sample capsule of boron nitride (BN) are alsodetected.

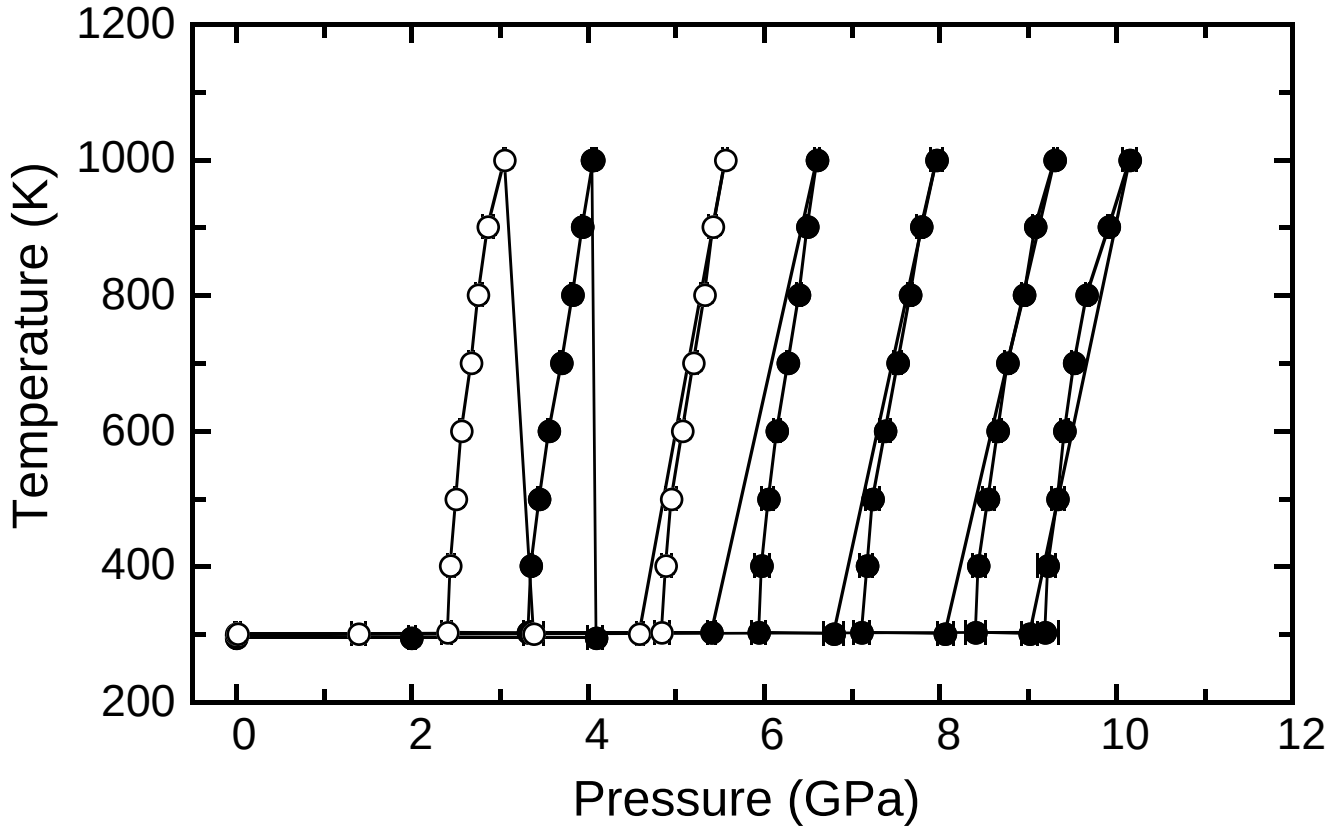

Fig. 1-3. Pressure-temperature paths of present experiments. Solid and open circles are Run#1 and Run#2, respectively. The pressures are calculated by the Brown (1999) EOS of NaCl.

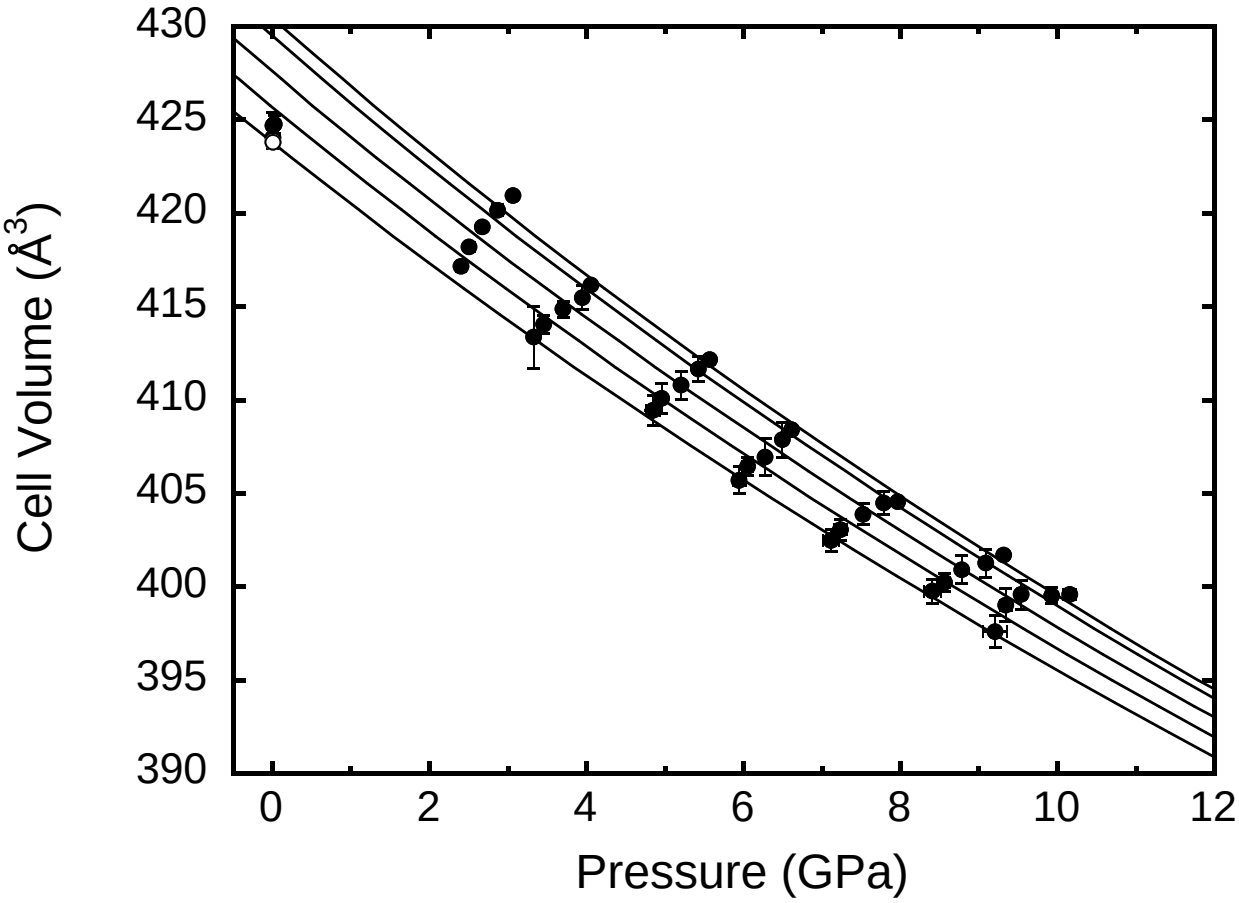

Fig. 1-4. *P-V-T* data of omphacite with calculated isothermal compression curves. Open circle is the result of angle dispersive X-ray diffraction at ambient condition. Pressures are based on Brown's scale (Brown, 1999). Data collected at 300 K, 500 K, 700 K, 900 K and 1000 K are plotted. The isotherms (from lower cell volumes, 300, 500, 700, 900 and 1000 K) are calculated from thermoelastic parameters derived at $K'_T = 4.0$ (Table 1-4).

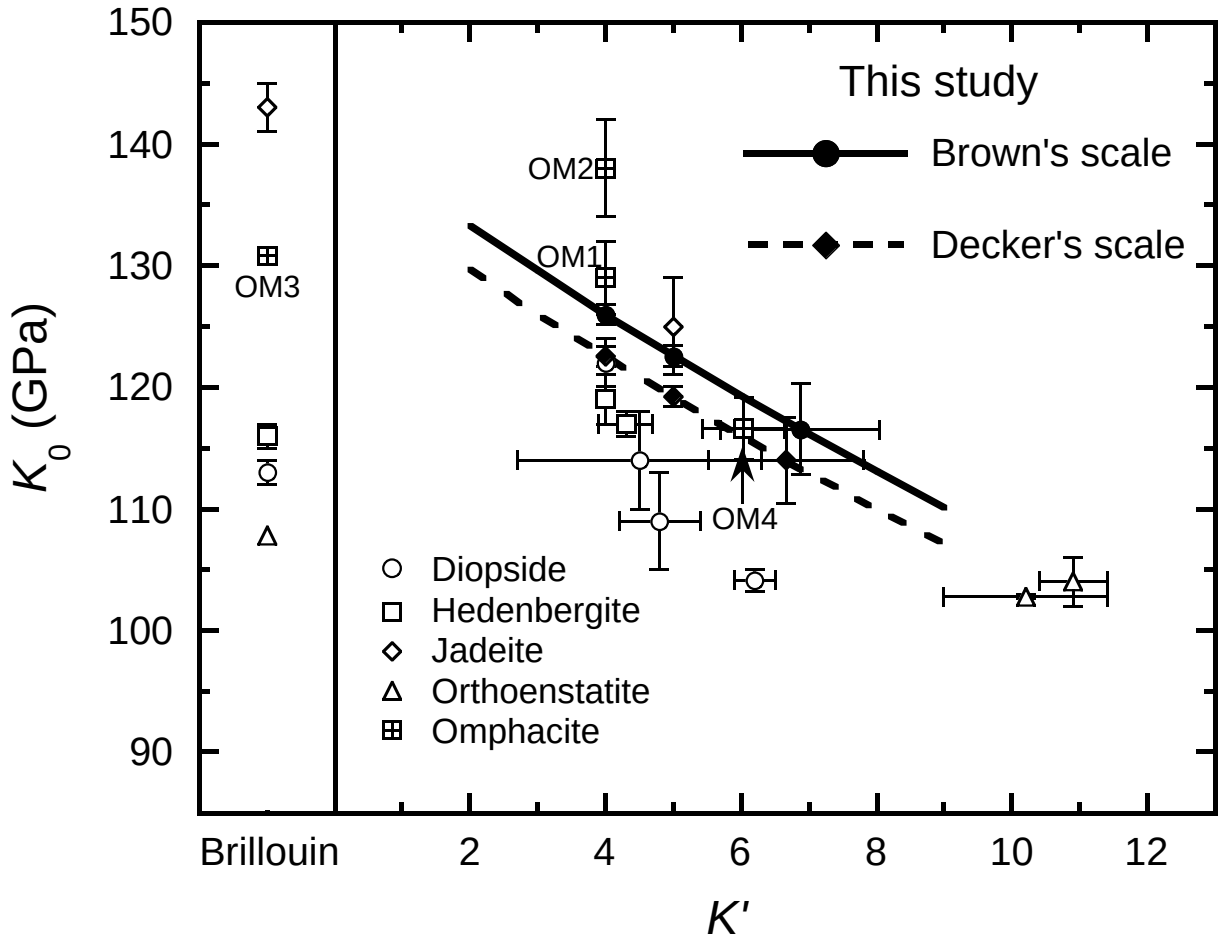

Fig. 1-5. Dependence of K_0 on K' values for omphacite and comparison to other pyroxenes. Bold (solid and broken) lines represent the dependencies of K_{T0} on fixed K'_T. Solid symbols are fitted K_{T0} values without constraint on K'_T, and at K'_T = 4.0 and 5.0 (Table 1-4). Solid lines and solid circles are based on Brown's scale (Brown, 1999). Broken lines and solid diamonds are based on Decker's scale (Decker, 1971). Open symbols are diopside (circles, Levien et al., 1979; Levien and Prewitt, 1981; McCormick et al., 1989; Zhang et al., 1997; Zhao et al., 1998), hedenbergite (squares, Kandelin and Weidner, 1988a; Zhang and Hafner, 1992; Zhang et al., 1997), jadeite (diamonds, Kandelin and Weidner, 1988b; Zhao et al., 1997), orthoenstatite (triangles, Weidner et al., 1978; Zhao et al., 1995; Flesch et al., 1998) and omphacite (squares with cross, McCormick et al., 1989 (OM1, OM2); Bhagat et al., 1992 (OM3); Pavese et al., 2001 (OM4)). OM2 and OM3 have identical compositions. Data plotted in the left box are the results of Brillouin scattering measurements (K_{S0}) at ambient conditions and their K' are not determined. Previous high-P XRD results are comparable with present results based on Decker's scale (see text).

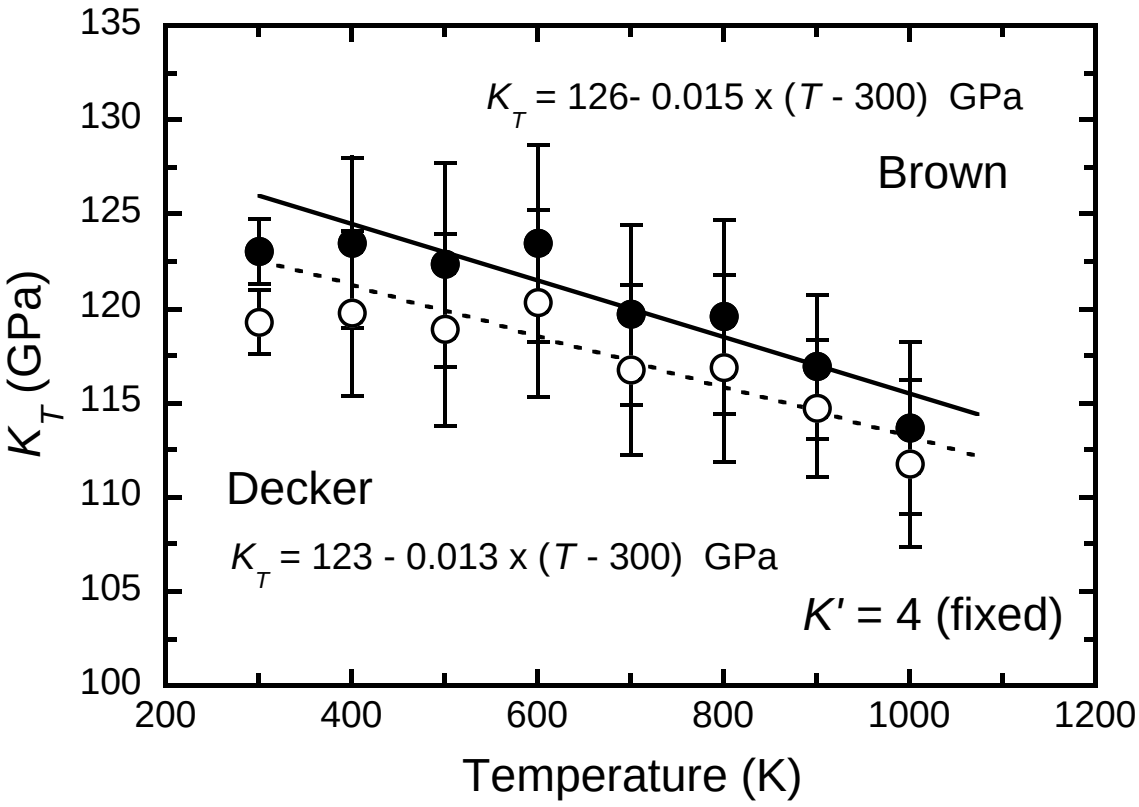

Fig. 1-6. Variations of the isothermal bulk modulus for omphacite against temperature. Circles are isothermal bulk moduli calculated by fitting the data at each temperature. Lines are the results of fits to the HTBM equation of state (Table 1-4). Solid circles and the solid line are based on Brown's scale (Brown, 1999); open circles and the broken line are based on Decker's scale (Decker, 1971). K'_T is fixed to be 4.0 in the calculations.

Chapter 2
Thermal equation of state of $(Mg_{0.91}Fe_{0.09})_2SiO_4$ ringwoodite

Abstract

In-situ synchrotron X-ray diffraction experiments were conducted using the SPEED-1500 multi-anvil press of SPring-8 on $(Mg_{0.91}Fe_{0.09})_2SiO_4$ ringwoodite, whose composition is similar to that expected in the Earth's mantle transition zone. Pressure-volume-temperature data were collected using a NaCl or MgO capsule up to 21 GPa and 1273 K. A fit to high-temperature Birch-Murnaghan equation of state (EOS) with fixed values of ambient cell volume V_0 = 527.83(7) Å^3 and isothermal bulk modulus K_{T0} =187 GPa yielded a pressure derivative of isothermal bulk modulus K'_T = 4.4(1), a temperature derivative of bulk modulus $(\partial K_T/\partial T)_P$ = –0.028(5) GPa K^{-1}, and a volumetric thermal expansivity $\alpha = a + bT$ with values of a = 1.9(2) × 10^{-5} K^{-1} and b = 1.2(4) × 10^{-8} K^{-2}. These properties are consistent with the analysis using the thermal pressure EOS. The derived K'_T and $(\partial K_T/\partial T)_P$ are consistent with previous studies on Mg_2SiO_4 ringwoodite. However, as well as measurements at 0 GPa, the present equation of state yields significantly higher thermal expansivity than derived by diamond anvil experiments on Mg_2SiO_4 ringwoodite to 30 GPa and 700 K. On the basis of the equation of state, the density jump at around 660 km depth expected for pyrolitic homogeneous mantle (caused by ringwoodite (Rw) → Mg-perovskite (MgPv) + magnesiowüstite (Mw) and garnet → MgPv transitions) was estimated. Consequently, the density jump for pyrolite (9.2%) is significantly larger than that across the 660-km discontinuity derived by recent seismological studies (4–6%). This possibly suggests that the recent seismic data reflect only the sharp transition concerned with the Rw → MgPv + Mw transition.

Keywords: Ringwoodite; Equation of state; High-pressure and high-temperature; X-ray

diffraction; Mantle transition zone; 660-km discontinuity

2-1 Introduction

The Pyrolite model has been widely accepted for the chemical composition of the Earth's mantle, and phase relations in this composition at the mantle *P-T* conditions has been extensively studied by high-pressure and high-temperature experiments (e.g. Akaogi and Akimoto, 1979; Irifune, 1987, 1994; Irifune and Isshiki, 1998, Wood, 2000; Hirose, 2002). These studies revealed that the pyrolitic mantle is mainly composed of ~60% ringwoodite (γ-$(Mg,Fe)_2SiO_4$) and ~40% majoritic garnet at conditions of the lower part of the mantle transition zone (~520–660 km depths). Although some studies preferred olivine-poorer compositions for the mantle transition zone (e.g. Bass and Anderson, 1984; Duffy and Anderson, 1989; Nishihara and Takahashi, 2001), ringwoodite is still one of the most abundant minerals in that region. The velocity and density increases across the 660-km discontinuity, which would be caused by decomposition of ringwoodite to Mg-rich silicate perovskite and magnesiowüstite are widely used to estimate temperature and mineralogy in this region (e.g. Akaogi et al, 1989; Matsui, 2001). Thus, knowledge of the thermoelastic properties of ringwoodite is very important to understand the nature of the mantle transition zone.

Because of its geophysical importance, thermoelastic properties of ringwoodite have been widely studied: thermal expansion at high-temperatures (Suzuki et al., 1979), room-temperature compressibility (Hazen, 1993; Zerr et al., 1993), acoustic velocities at ambient condition (Weidner et al., 1984; Sinogeikin et al., 1997, 1998), at high-temperatures (Jackson et al., 2000; Sinogeikin et al., 2001) and at high-pressures (Rigden and Jackson, 1991; Rigden et al., 1991; 1992; Sinogeikin et al., 2001). However, studies under simultaneous high-pressure and high-temperature conditions are still limited.

Meng et al. (1993) measured unit cell volumes of ringwoodite with Mg_2SiO_4 composition

in the temperature range from 759 K to 962 K at 9.8 GPa using synchrotron X-ray diffraction in a cubic anvil apparatus, but this pressure is still below the thermodynamically stable conditions of this mineral. Meng et al. (1994) reported the volume measurements on Mg_2SiO_4 ringwoodite to 30 GPa at 300–700 K using an externally heated diamond anvil cell, but the temperatures are far lower than estimated temperatures in the Earth's transition zone.

In the present study, we measured the change of unit cell volume of $(Mg_{0.91}Fe_{0.09})_2SiO_4$ ringwoodite, whose composition is close to that expected for ringwoodite in the Earth's mantle, at pressure and temperature conditions up to 21 GPa and 1273 K with synchrotron radiation, and the thermal equation of state (EOS) was determined. The pressure range essentially overlaps with the entire stability field of this mineral, and the temperature range is significantly expanded from previous *P-V-T* studies. By using the present results, the density jump caused by decomposition of ringwoodite to Mg-rich silicate perovskite and magnesiowüstite is calculated, and the expected density jump for pyorlite mantle at Earth's 660-km depth condition is compared with the recent seismic observations.

2-2 Experimental procedures

Samples

$(Mg_{0.91}Fe_{0.09})_2SiO_4$ ringwoodite was synthesized from natural olivine (Mg# = 91), collected from granular lherzorite xenolith (K-6, from Australia) using the SPI-1000, the 1000 ton multi-anvil press at the Magma Factory, Tokyo Institute of Technology (Takahashi et al., 1993). The powdered olivine was enclosed in a Re foil capsule, and experimental conditions were P = 21.5 GPa, T = 1473 K and t = 1 h. The experimental technique and the cell assembly used in the synthesis experiment are similar to those of Wang and Takahashi (2000) and Nishihara and Takahashi (2001). Chemical analyses were performed using a JEOL-8800 microprobe and synthesis of single-phase ringwoodite was confirmed. The chemical composition, including

minor elements, of the synthesized ringwoodite is $(Mg_{0.907}Fe_{0.088}Ni_{0.004}Mn_{0.001})_2SiO_4$. According to Frost et al. (2001), the $Fe^{3+}/\Sigma Fe$ content of ringwoodite synthesized within Re capsule is below 0.03, which is effectively zero. Then, we ignored the effect of solution of Fe_2FeO_4 component. Angle-dispersive X-ray powder diffraction with Cr Kα radiation was carried out at ambient conditions using Si as an external standard to calibrate diffraction angle. The unit-cell parameters of the ringwoodite was determined to be a = 8.0816(3) Å and V = 527.83(7) $Å^3$ from the positions of 6 diffraction peaks (220, 311, 400, 422, 511 and 440). Variation of the cell volume of the ringwoodite solid solution in the system Mg_2SiO_4-Fe_2SiO_4 is determined by Marumo et al. (1977) and Akaogi et al. (1989). The linear interpolation of their data predicts V = 528.0 $Å^3$ for $(Mg_{0.91}Fe_{0.09})_2SiO_4$. This volume is in good agreement with our result.

P-V-T experiments

P-V-T experiments were conducted using the SPEED-1500 apparatus installed on beam line BL04B1 at SPring-8, Hyogo, Japan. Detailed information about this system is described by Utsumi et al. (1998). Eight WC anvils (3.0 mm truncation size) were used for high-pressure generation.

Fig. 2-1 shows schematic illustration of cell assembly for high-pressure and high-temperature X-ray diffraction. Semisintered $LaCrO_3$ is used for the pressure medium as well as thermal insulator and (Mg,Co)O is placed along the X-ray path instead of $LaCrO_3$ for the X-ray window (see Fig. 2-1). A W5%Re-W26%Re thermocouple wire is inserted vertically, and two sample capsules are placed horizontally at the center of the cell assembly. This enables us to observe two (or more) different samples even when the anvil gap becomes extremely narrow (~0.3 mm) at the highest pressures. The samples are heated with an internal resistance heater made of a mixture of TiC and diamond powders (1:1 by weight). Powdered ringwoodite and a mixture of Au (grain size ~2 μm) and MgO (1:4 by weight, pressure marker) were packed into

the NaCl or MgO sample chamber separately. Pressure was determined by EOSs of Au (Anderson et al., 1989; Shim et al., 2002).

A solid-state detector connected to a multi-channel analyzer was used for data collection. The multi-channel analyzer was calibrated with the characteristic X-rays of Cu, Mo, Ag, Ta, Pt and Pb. The diffracted X-rays from the sample were collected at a fixed 2θ angle of ~5.6° by the energy dispersive method with a horizontal goniometer. The 2θ angle was determined using the unit-cell volume of Au. The incident X-ray beam was collimated to 0.2 mm and 0.05 mm in the vertical and horizontal dimensions, respectively. Three thin slits between the sample and the detector, 2.0 mm in the vertical dimension and 0.05 and 0.2 mm in the horizontal were used to eliminate diffracted X-rays from the pressure medium. Typical exposure times for collecting diffraction patterns of the sample and pressure marker were 400 and 200 s, respectively. Temperature variation indicated by the thermocouple was within 2 K.

Fig. 2-2 shows an example of the diffraction spectrum of ringwoodite. The unit-cell parameters were calculated from peak positions by least squares technique. In the calculation, at least 5 diffraction peaks were used from 220, 311, 400, 422, 511 and 440. The pressure was determined from the observed cell volume of Au calculated from four diffraction lines 111, 200, 220, and 311. Used pressure scales of Au are Anderson et al. (1989) and Shim et al. (2002).

Anderson's pressure scale has been widely used for in situ X-ray diffraction experiments in the last decade (e.g. Meng et al., 1994; Funamori et al., 1996; Irifune et al., 1998; Fei, 1999). However, Anderson et al. (1989) derived the EOS based on the measured elastic and thermodynamic properties of Au at temperatures only less than 550 K, where the electronic contribution to thermal expansion is expected to be very small. Very recently, Shim et al. (2002) reported a new *P-V-T* equation of state of Au based on the inversion of recent quasi-hydrostatic compression and shock wave data. However, Shim et al.'s (2002) EOS shows disagreement with the zero-pressure measurements in terms of $(\partial K_S/\partial T)_P$. The calculated pressures using these EOSs

reaches 0.5 GPa at the maximum in the *P-T* conditions of present experiments. Because it changes systematically, they affect significantly the derived EOS of ringwoodite. However, we cannot judge which EOS is expected to be more accurate. Thus, in our study, the pressure values based on Anderson et al.'s (1989) gold pressure scale are used primarily because it has been used most frequently in EOS measurement. Comparison with Shim et al.'s (2002) is also made.

Three *P-V-T* experiments were conducted. One (experiment no. S602) used an MgO capsule and two (S648 and S649) used NaCl capsules. The samples were compressed to the desired pressure at room temperature and heated to the maximum temperature (873, 1073 or 1273 K) to release non-hydrostatic stress. X-ray diffraction data for both the sample and the pressure marker were collected at fixed temperatures at 200 K intervals under constant load.

The *P-V-T* data collected with MgO capsule after heating to 873, 1073 and 1273 K showed significant deviation in spite of their relatively sharp diffraction peaks. For example, a fit of the third-order Birch Murnaghan EOS (Eq. (1), see below) to data collected at 300 K yields very large root mean square (RMS) misfit 0.77 GPa (with fixed V_0 = 527.83 Å^3 and K_{T0} = 187 GPa). On the other hand, the data collected with NaCl capsule after heating to 873 and 1073 K showed relatively good consistency with each other, and they also consistent with the data collected with MgO capsule after heating to 1273 K. The RMS misfit of the fit to these data at 300 K is reasonably reduced to be 0.23 GPa. These would mean that the macroscopic differential stress for the sample within the MgO capsule is not effectively released by heating at temperature below 1273 K, and that for the sample within the NaCl capsule is effectively released by heating to above 873 K. These are generally consistent with the stress analyses of MgO and NaCl at high-temperature and high-temperature by Weidner et al. (1994). Because we used powdered sample for experiments, the microscopic stress may also affect the quality of *P-V-T* data (Weidner et al., 1994). This could cause some scatters for present *P-V-T* data.

In the following calculations, we use the data collected after heating to 1273 K for MgO

capsule and after heating to above 873 K for NaCl capsule. Fig. 2-3 shows the *P-T* conditions of the used data and estimated phase boundary in $(Mg_{0.91}Fe_{0.09})_2SiO_4$ (Akaogi et al., 1989; Ito and Takahashi, 1989; Irifune et al., 1998; Kuroda et al., 2000). In order to avoid back transformation to lower pressure phases, heating was limited to 873 K when outside the stability field of $(Mg_{0.91}Fe_{0.09})_2SiO_4$ (Fig. 2-3).

2-3 Results and discussion

High-temperature Birch-Murnaghan equation of state

The unit-cell parameters of $(Mg_{0.91}Fe_{0.09})_2SiO_4$ ringwoodite at various *P-T* conditions are given in Table 2-1. Fig. 2-4 shows the volume data with calculated isothermal compression curves. The slight scatters in the data is possibly due to the remaining non-hydrostatic stress. The high-temperature Birch-Murnaghan (HTBM) equation of state is often used to fit the *P-V-T* data (e.g. Funamori et al., 1996; Wang et al., 1998; Nishihara et al., 2003). The equation of state is given by the following expression:

$$P = 3/2K_T\left[\left(V_{0T}/V\right)^{7/3} - \left(V_{0T}/V\right)^{5/3}\right]\left\{1 + 3/4\left(K_T' - 4\right)\left[\left(V_{0T}/V\right)^{2/3} - 1\right]\right\} \quad (1)$$

where K_T, V_{0T}, V and K'_T are the isothermal bulk modulus, zero-pressure volume, high-pressure volume, and pressure derivative of K_T, respectively. The temperature effects for K_T and V_{0T} are expressed as follows:

$$K_T = K_{T0} + \left(\partial K_T / \partial T\right)_P\left(T - 300\right) \quad (2)$$

$$V_{0T} = V_0 \exp\left[\int_{300}^{T} \alpha \mathrm{d}T\right] \quad (3)$$

where $(\partial K_T/\partial T)_P$, V_0 and α are the temperature derivative of the bulk modulus, volume at room condition and the volumetric thermal expansion at atmospheric pressure, respectively. The K'_T and $(\partial K_T/\partial T)_P$ values are assumed to be constant. V_0 was fixed to the value determined by angle-dispersive X-ray diffraction (V_0 = 527.83 Å^3) at ambient condition.

The experimental *P-V-T* data (Table 2-1) were fitted to HTBM equation of state. The fits without constraint on K_{T0} and K'_T yielded K_{T0} = 173(3) GPa and K'_T = 6.5(5) (Anderson et al.'s pressure scale). However, this K'_T value is relatively high as silicate mineral (typically K'_T = 4–5), and it is well known that there is a trade-off between the values of K_{T0} and K'_T in calculating these properties from *P-V* data (e.g. Bass et al., 1981). Because of the limited range and precision of the volume data, we could not resolve both K_{T0} and K'_T values simultaneously with confidence.

We also calculated the equation of state by fixing K_{T0}. Sinogeikin et al. (1998, 2001) determined the adiabatic bulk modulus of $(Mg_{0.91}Fe_{0.09})_2SiO_4$ ringwoodite to be K_{S0} = 188(3) GPa by Brillouin scattering. We used an isothermal bulk modulus K_{T0} = 187 GPa, which is converted from K_{S0} = 188(3) GPa, to constrain the other thermoelastic parameters accurately. In the conversion from K_S to K_T, the following thermodynamic identity was used: $K_{T0} = K_{S0}/(1 + \alpha\gamma_G T)$, where γ_G is Grüneisen parameter, data for α and γ_G are from Suzuki et al. (1979) and Watanabe (1987), respectively. The results of a fit with fixing K_{T0} = 187 GPa are listed in Table 2-2. We obtained K'_T = 4.4(1), this K'_T values are typical for silicate minerals. Compression curves depicted in Fig. 2-4 are calculated from thermoelastic parameters derived using K_{T0} = 187 GPa (pressure scale is Anderson et al., 1989).

Use of the different Au pressure scales causes significant variation in the derived thermoelastic parameters of $(Mg_{0.91}Fe_{0.09})_2SiO_4$ ringwoodite (Table 2-2). Shim et al.'s (2002) scale results in lower absolute value of $(\partial K_T/\partial T)_P$ of ringwoodite (–0.015(5) GPa K^{-1}; Table 2-2) than the Anderson et al.'s (1989) scales (–0.028(5) GPa K^{-1}; Table 2-2).

Thermal expansion of ringwoodite at 0 and 20 GPa was calculated from the parameters in

Table 2-2, and is depicted in Fig. 2-5. Thermal expansion at 0 GPa calculated from present equation of state of $(Mg_{0.91}Fe_{0.09})_2SiO_4$ ringwoodite, which is extrapolated from high-pressures, shows reasonably good agreement with direct measurements at 0 GPa on Mg_2SiO_4 and Fe_2SiO_4 ringwoodites (Suzuki et al., 1979; Yamanaka, 1986; Inoue et al., 2003). As shown in Funamori et al. (1996), the choice of pressure scale significantly affects thermal expansivity at high-pressures. At 20 GPa, Shim et al.'s of Au results in significantly larger thermal expansivity of ringwoodite than that by Anderson et al.'s scale (lower panel of Fig. 2-5). It is clearly recognized that choice of the pressure scale significantly affects the density estimate of model mantle composition at high-pressure and high-temperature using thermal equation of state.

Thermal pressure equation of state

We also analyze the *P*-*V*-*T* data using the thermal pressure equation of state (Anderson, 1984). At any temperature *T* and for a given volume *V*, the pressure is expressed as the sum of the static pressure at room-temperature $P(V,300)$ and the thermal pressure ΔP_{th} (see Jackson and Rigden, 1996). Then, ΔP_{th} is expressed by:

$$\begin{aligned}\Delta P_{th} &= P(V,T) - P(V,300) \\ &= (T-300)\alpha K_T - (T-300)\ln(V/V_0)(\partial K_T/\partial T)_V + (T-300)^2\left[\left(\partial^2 P/\partial T^2\right)_V\right]/2 . \end{aligned} \quad (4)$$

For expression of $P(V,300)$, we used Eq. (1). As shown in Fig. 2-6, ΔP_{th} increases linearly with temperature within the deviation of data. This means $(\partial^2 P/\partial T^2)_V$ is close to zero and not resolvable. Then, we fixed to be $(\partial^2 P/\partial T^2)_V = 0$ GPa K^{-2} in the calculation.

The results of a fit of the data with fixed $K_{T0} = 187$ GPa is listed in Table 2-3. The derived values of $K'_T = 4.3(1)$ and $\alpha_0 = 2.5(1) \times 10^{-5}$ K^{-1} are reasonably consistent with those derived by the fit to HTBM equation of state ($\alpha_0 = 2.3(2) \times 10^{-5}$ K^{-1} from $\alpha_0 = a + b \times 300$; Table 2-2,

Anderson et al.'s scale). Within the uncertainty of the fit $(\partial K_T/\partial T)_V$ value is roughly zero, indicating that the thermal pressure is independent of volume. This property is same as other silicate minerals: olivine (Guyot et al., 1996), $CaSiO_3$ perovskite (Wang et al., 1996) and garnet (Wang et al., 1998).

By using thermodynamic relation: $(\partial K_T/\partial T)_P = (\partial K_T/\partial T)_V - \alpha K_T K'_T$, we can obtain $(\partial K_T/\partial T)_P = -0.026(4)$ GPa K^{-1}. This result is in good agreement with previous analysis using HTBM equation of state (Table 2-2). The results for the data based on Shim et al.'s pressure scale are similarly consistent with those by the HTBM equation of state fit (Table 2-2, 2-3).

Comparison with previous studies

Fig. 2-7 shows comparison of room temperature V/V_0 data of ringwoodites with Mg-rich composition. The solid line is calculated compression curve with K_{T0} = 187 GPa and K'_T = 4.4 (Table 2-2). This equation of state of $(Mg_{0.91}Fe_{0.09})_2SiO_4$ ringwoodite is generally consistent with those of previous studies. Slight variation between different studies would be due to a compositional dependence of compressibility.

Elastic properties of ringwoodite have been investigated by many authors. Table 2-4 summarizes bulk modulus, its pressure derivative and its temperature derivative of $(Mg,Fe)_2SiO_4$ ringwoodite solid solution determined with various experimental techniques. Adiabatic values (K_{S0}, K'_S and $(\partial K_S/\partial T)_P$) can be obtained by Brillouin scattering and ultrasonic technique. These values are converted to isothermal values (K_{T0}, K'_T and $(\partial K_T/\partial T)_P$) by using the following equations: $K_{T0} = K_{S0}/(1 + \alpha\gamma_G T)$, $K'_T \approx (1 + \alpha\gamma_G T)^{-1}[K'_S - \gamma_G T(\partial K_T/\partial T)_P/ K_T]$, $(\partial K_T/\partial T)_P \approx (\partial K_S/\partial T)_P /(1 + \alpha\gamma_G T) - K_S/(1 + \alpha\gamma_G T)^2[\alpha\gamma_G + (\partial\alpha/\partial T)\gamma_G T]$ (Speziale and Duffy, 2002), data for α and γ_G are from Suzuki et al. (1979) and Watanabe (1987), respectively. The bulk modulus and its pressure derivative do not change so much by this conversion and the changes are within the experimental errors. However, the change of temperature derivative of bulk modulus is quite

significant (e.g. $(\partial K_S/\partial T)_P$ = –0.021(2) GPa K^{-1} to $(\partial K_T/\partial T)_P$ = –0.028(2) GPa K^{-1}, data from Sinogeikin et al., 2001). Thus, this conversion is necessary for comparison of this property.

The bulk modulus (K_{T0}) of $(Mg,Fe)_2SiO_4$ ringwoodite increases from 184 to ~205 GPa as the Fe content increases from 0 to 100% (Table 2-4, Sinogeikin et al., 1998). The value K_{T0} = 187 GPa for $(Mg_{0.91}Fe_{0.09})_2SiO_4$ ringwoodite, which was used in the above calculation to derive thermal equation of state, is consistent with this systematic trend. For K'_T and $(\partial K_T/\partial T)_P$, no systematic trend is detectable partly due to scatters in the reported values (Table 2-4).

The K'_T value is derived from some high-pressure studies. Among these K'_T values, that by Sinogeikin et al. (2001) (K'_T = 4.1(3)) is considered to be most accurate, because it is from direct measurements of elastic moduli (Brillouin scattering) at relatively wide pressure conditions (0–16 GPa). Although Rigden et al. (1991, 1992) and Rigden and Jackson (1991) also conducted direct measurements of elastic moduli (ultrasonic interferometry) to 3 GPa, their relatively high K'_T (4.7 and 5.6) may result from porosity or grain-boundary scattering (Sinogeikin et al., 2001). The K'_T value from our experiments is consistent with that by Sinogeikin et al. (2001).

Our $(\partial K_T/\partial T)_P$ value based on Anderson et al.'s scale is consistent with previous studies (Meng et al., 1993; 1994, Sinogeikin et al., 1998; 2001; Jackson et al., 2000). When Shim et al.'s scale is used, significantly lower absolute value of $(\partial K_T/\partial T)_P$ (–0.015(5) GPa K^{-1}) than those of previous studies is obtained. This would be related to that Shim et al.'s EOS of gold shows extremely small absolute value of $(\partial K_S/\partial T)_P$ compared to zero-pressure measurements (see Fig. 3c of Shim et al., 2002).

Fig. 2-5 shows comparison of thermal expansivity of ringwoodites at 0 and 20 GPa. As recognized from the scatter of data by measurements at 0 GPa (Suzuki et al., 1979; Yamanaka, 1986; Inoue et al., 2003) (upper panel of Fig. 2-5), compositional dependence of thermal expansivity is not clear. The thermal equation of state of Mg_2SiO_4 ringwoodite by Meng et al. (1994) has been widely used to investigate nature of the 660-km seismic discontinuity (e.g.

Weidner and Wang, 1998; Vacher et al., 1998). However, their EOS shows significant difference between our EOS of $(Mg_{0.91}Fe_{0.09})_2SiO_4$ ringwoodite in terms of thermal expansivity, while parameters in Table 2-4 are consistent each other. Meng et al. (1994) used EOS of Au by Anderson et al. (1989) for pressure standard for their high-temperature experiments, then our results based on Anderson et al.'s scale is comparable. At 0 GPa, Meng et al.'s EOS shows slightly lower thermal expansion than those of ours and zero-pressure measurements. This tendency is preserved at high-pressures, and thermal expansivity of ringwoodite based on Meng et al. is ~60% of ours at 20 GPa (lower panel of Fig. 2-5). The discrepancy may suggest that thermocouple reading outside the DAC actually does not give true temperature inside in their experiments. The use of different pressure scales for room-temperature (ruby fluorescence and EOS of Ne) and high-temperature (EOS of Au, Anderson et al., 1989) is also possibly responsible.

Fig. 2-6 shows comparison of thermal pressure ΔP_{th} of ringwoodite against temperature. The results of this study is in good agreement with the zero-pressure study by Suzuki et al. (1979) and the measurements at 9.8 GPa by Meng et al. (1993). Another zero-pressure study by Inoue et al. (2003) shows slightly higher ΔP_{th} than that by this study, and this property is similar to the previous comparison for thermal expansivity (Fig. 2-5). The results by Meng et al. (1994) show large scatters and relatively lower ΔP_{th} than those by other studies. Meng et al. (1994) reported a very large absolute value $(\partial K_T/\partial T)_V = -0.013$ GPa K^{-1}. However, it is clear from Fig. 2-6 that the large scatters and limited temperature range of Meng et al.'s (1994) data prevent to resolve this property accurately.

As discussed above, our EOS of $(Mg_{0.91}Fe_{0.09})_2SiO_4$ ringwoodite, based on the data collected at relatively wide *P-T* range, is generally consistent with previous zero-pressure or room-temperature measurements which seem to be reliable. Therefore, this EOS of ringwoodite enables highly robust estimation on thermoelasticity of this mineral in the Earth's mantle.

Implications for the 660-km discontinuity

In order to compare the seismically observed density jump across the 660-km discontinuity ($\Delta\rho_{660}$) with the density jump caused by the decomposition reaction ringwoodite $\rightarrow$ Mg-perovskite + magnesiowüstite, thermoelastic calculations were carried out based on the EOS of ringwoodite determined in this study. Thermoelastic parameters of Mg-perovskite are taken from Funamori et al. (1996) and those of magnesiowüstite are from Fei (1999) and Suzuki (1975), respectively. In these previous works on Mg-perovskite and magnesiowüstite, pressure was calculated by Anderson et al.'s (1989) EOS of Au, so that EOS of ringwoodite based on Anderson et al.'s scale in this study is also used for consistency. These parameters of Mg-perovskite and magnesiowüstite are values for the Mg end-member. The zero-pressure densities of these materials were corrected to be Mg# = 100 Mg/(Mg + Fe) (molar ratio) = 89, 91 and 87 for ringwoodite, Mg-perovskite and magnesiowüstite, respectively, using the data of Vacher et al. (1998). The calculated density jump at 660 km condition (23.4 GPa and 1873 K) is 8.9%.

According to recent phase equilibria studies, the density and seismic velocity jumps at around 660 km depth are mainly responsible to two phase transitions: (1) ringwoodite (Rw) $\rightarrow$ Mg-perovskite (MgPv) + magnesiowüstite (Mw) and (2) garnet (Grt) $\rightarrow$ Mg-perovskite (MgPv) (e.g. Weidner and Wang, 1998; Hirose, 2002; Akaogi et al., 2002). The former is very sharp transition (< ~5 km width, Ito and Takahashi, 1989), while the latter is relatively broad (~30–50 km width, Hirose, 2002; Akaogi et al., 2002). The size estimates of density and seismic velocity jump across the 660-km discontinuity by long-period (>15 s) seismic studies are considered to be the sum of these transitions.

If we assume that the composition of the mantle is pyrolitic (61 vol% ringwoodite at the base of transition zone, Hirose, 2002) and chemically homogeneous through the 660-km discontinuity, the Rw $\rightarrow$ MgPv + Mw transition yields 5.4% density jump. By using estimated

contribution of the Grt → MgPv transition for the density jump in pyrolite by Akaogi et al. (2002) (3.8%), the combined density jump around 660 km is 9.2%. This property is in good agreement with seismic PREM model ($\Delta\rho_{660}$ = 9.3%; Dziewonski and Anderson, 1981), and however, significantly larger than recent seismic models of the 660-km discontinuity derived using long-period data: $\Delta\rho_{660}$ = 6.2% (Esterbrook and Kind, 1996), 5.2% (Shearer and Flanagan, 1999) and 5.4% (Kato and Kawakatsu, 2001). The reason of this discrepancy is unclear. The recent short-period (2–5 s) data yields similar results ($\Delta\rho_{660}$ = 4.2%, Castle and Creager, 2000) to long-period studies. These results possibly suggest that the recent seismic long-period data reflect only the sharp transition concerned with the Rw → MgPv + Mw transition.

Acknowledgements

We thank N. Nishiyama for his advice on experimental techniques, and K. Hirose, T. Komabayashi and M. Shindo for their helpful support for the in situ X-ray diffraction experiments. We also thank T. Inoue for providing *V-T* data for Mg_2SiO_4 ringwoodite before publication. Constructive comments by Y. Wang, T. Katsura, T.S. Duffy and T. Irifune were helpful in improving the manuscript. The in situ X-ray diffraction experiments were performed by using the SPEED-1500 system at BL04B1 in SPring-8 (proposal no. 2000B0548-CD-np and 2001A0272-CD-np). Y.N. is grateful for the Research Fellowships of the Japan Society of the Promotion of Science for Young Scientists.

References

Akaogi, M., Akimoto, S., 1979. High-pressure phase equilibria in a garnet lherzolite, with special reference to Mg^{2+}-Fe^{2+} partitioning among constituent minerals. Phys. Earth Planet. Int. 19, 31–51.

Akaogi, M., Ito, E., Navrotsky, A., 1989. Olivine-modified spinel-spinel transitions in the system

Mg_2SiO_4-Fe_2SiO_4: calorimetric measurements, thermochemical calculation, and geophysical application. J. Geophys. Res. 94, 15671–15685.

Akaogi, M., Tanaka, A., Ito, E., 2002. Garnet-ilmenite-perovskite transitions in the system $Mg_4Si_4O_{12}$-$Mg_3Al_2Si_3O_{12}$ at high pressures and high temperatures: phase equilibria, calorimetry and implications for mantle structure. Phys. Earth Planet. Int. 132, 303–324.

Anderson, O.L., 1984. A universal thermal equation-of-state. J. Geodyn. 1, 185–214.

Anderson, O.L., Isaak, D.G., Yamamoto, S., 1989. Anharmonicity and the equation of state for gold. J. Appl. Phys. 65, 1534–1543.

Bass, J., Anderson, D.L., 1984. Composition of the upper mantle: geophysical tests of two petrological models. Geophys. Res. Lett. 11, 237–240.

Bass, J.D., Liebermann, R.C., Weidner, D.J., Finch, S.J., 1981. Elastic properties from acoustic and volume compression experiments. Phys. Earth Planet. Int. 25, 140–158.

Castle, J.C., Creager, K.C., 2000. Local sharpness and shear wave speed jump across 660-km discontinuity. J. Geophys. Res. 105, 6191–6200.

Decker, D.L., 1971. High-pressure equation of state for NaCl, KCl, and CsCl. J. Appl. Phys. 42, 3239–3244.

Duffy, T.S., Anderson, D.L., 1989. Seismic velocities in mantle minerals and the mineralogy of the upper mantle. J. Geophys. Res. 94, 1895–1912.

Dziewonski, A.M., Anderson, D.L., 1981. Preliminary reference Earth model. Phys. Earth Planet. Int. 25, 297–356.

Esterbrook, C.H., Kind, R., 1996. The nature of the 660-kilometer upper-mantle seismic discontinuity from precursors to the PP phase. Science 274, 1179–1182.

Fei, Y., 1999. Effects of temperature and composition on the bulk modulus of (Mg,Fe)O. Am. Mineral. 84, 272–276.

Frost, D.J., Langenhorst, F., van Aken, P.A., 2001. Fe-Mg partitioning between ringwoodite and

magnesiowüstite and the effect of pressure, temperature and oxygen fugacity. Phys. Chem. Mineral. 28, 445–470.

Funamori, N., Yagi, T., Utsumi, W., Kondo, T., Uchida, T., Funamori, M., 1996. Thermoelastic properties of $MgSiO_3$ perovskite determined by in situ X ray observations up to 30 GPa and 2000 K. J. Geophys. Res. 101, 8257–8269.

Guyot, F., Wang, Y., Gillet, P., Ricard, Y., 1996. Quasi-harmonic computations of thermodynamic parameters of olivines at high-pressure and high-temperature: a comparison with experiment data. Phys. Earth Planet. Int. 98, 17–29.

Hazen, R.M., 1993. Comparative compressibilities of silicate spinels: anomalous behavior of $(Mg,Fe)_2SiO_4$. Science 259, 206–209.

Hirose, K., 2002. Phase transitions in pyrolitic mantle around 670-km depth: Implications for upwelling of plumes from the lower mantle. J. Geophys. Res. 107, 10.1029/2001JB000597.

Inoue, T., et al., 2003. submitted to this volume.

Irifune, T., 1987. An experimental investigation of the pyroxene-garnet transformation in a pyrolite composition and its bearing on the constitution of the mantle. Phys. Earth Planet. Int. 45, 324–336.

Irifune, T., 1994. Absence of an aluminous phase in the upper part of the Earth's lower mantle. Nature 370, 131–133.

Irifune, T., Isshiki, M., 1998. Iron partitioning in a pyrolite mantle and the nature of the 410-km seismic discontinuity. Nature 392, 702–705.

Irifune, T., Nishiyama, N., Kuroda, K., Inoue, T., Isshiki, M., Utsumi, W., Funakoshi, K., Urakawa, S., Uchida, T., Katsura, T., Ohtaka, O., 1998. The postspinel phase boundary in Mg_2SiO_4 determined by in situ X-ray diffraction. Science 279, 1698–1700.

Ito, E., Takahashi, E., 1989. Postspinel transformations the system Mg_2SiO_4-Fe_2SiO_4 and some geophysical implications. J. Geophys. Res. 94, 10637–10646.

Jackson, I., Rigden, S.M., 1996. Analysis of P-V-T data: constraints on the thermoelastic properties of high-pressure minerals. Phys. Earth Planet. Int. 96, 85–112.

Jackson, J.M., Sinogeikin, S.V., Bass, J.D., 2000. Sound velocities and elastic properties of γ-Mg_2SiO_4 to 873 K by Brillouin spectroscopy. Am. Mineral. 85, 296–303.

Kato, M., Kawakatsu, H., 2001. Seismological in situ estimation of density jumps across the transition zone discontinuities beneath Japan. Geophys. Res. Lett. 28, 2541–2544.

Kuroda, K., Irifune, T., Inoue, T., Nishiyama, N., Miyashita, M., Funakoshi, K., Utsumi, W., 2000. Determination of the phase boundary between ilmenite and perovskite in $MgSiO_3$ by in situ X-ray diffraction and quench experiments. Phys. Chem. Minerals 27, 523–532.

Marumo, F., Isobe, M., Akimoto, S., 1977. Electron-density distributions in crystals of γ-Fe_2SiO_4 and γ-Co_2SiO_4. Acta Crstallogr. Sect. B 33, 713–716.

Matsui, M., 2001. Density and bulk sound velocity jumps across the 660 km seismic discontinuity. Phys. Earth Planet. Int. 125, 141–146.

Meng, Y., Weidner, D.J., Gwanmesia, G.D., Liebermann, R.C., Vaughan, M.T., Wang, Y., Leinenweber, K., Pacalo, R.E., Yeganeh-Haeri, A., Zhao, Y., 1993. In situ high-P-T X ray diffraction studies on three polymorphs (α, β, γ) of Mg_2SiO_4. J. Geophys. Res. 98, 22199–22207.

Meng, Y., Fei, Y., Weidner, D.J., Gwanmesia, G.D., Hu, J., 1994. Hydrostatic compression of γ-Mg_2SiO_4 to mantle pressures and 700 K: thermal equation of state and related thermoelastic properties. Phys. Chem. Minerals 21, 407–412.

Nishihara, Y., Takahashi, E., 2001. Phase relation and physical properties of an Al-depleted komatiite to 23 GPa. Earth Planet. Sci. Lett. 190, 65–77.

Nishihara, Y., Takahashi, E., Matsukage, K., Kikegawa, T., 2003. Thermal equation of state of omphacite. Am. Mineral. 88, 80–86.

Rigden, S.M., Jackson, I., 1991. Elasticity of germanate and silicate spinels at high pressure. J.

Geophys. Res. 96, 9999–10006.

Rigden, S.M., Gwanmesia, G.D., Fitz Gerald, J.D., Jackson, I., Liebermann, R.C., 1991. Spinel elasticity and seismic structure of the transition zone of the mantle. Nature 354, 143–145.

Rigden, S.M., Gwanmesia, G.D., Jackson, I., Liebermann, R.C., 1992. Progress in high-pressure ultrasonic interferometry, the pressure dependence of elasticity of Mg_2SiO_4 polymorphs and constraints on the composition of the transiton zone of the Earth's mantle. In: Syono, Y., Manghnani, M.H. (Eds.), High-Pressure Reserch: Application to Earth and Planetary Sciences. Am. Geophys. Union, Washington, DC, pp. 167–182.

Shearer, P.M., Flanagan, M.P., 1999. Seismic velocity and density jumps across the 410- and 660-kilometer discontinuities. Science 285, 1545–1548.

Shim, S.-H., Duffy, T.S., Takemura, K., 2002. Equation of state of gold and its application to the phase boundaries near 660 km depth in Earth's mantle. Earth Planet. Sci. Lett. 203, 729–739.

Sinogeikin, S.V., Bass, J.D., Kavner, A., Jeanloz, R., 1997. Elasticity of natural majorite and ringwoodite from the Catherwood meteorite. Geophys. Res. Lett. 24, 3265–3268.

Sinogeikin, S.V., Katsura, T., Bass, J.D., 1998. Sound velocities and elastic properties of Fe-bearing wadsleyite and ringwoodite. J. Geophys. Res. 103, 20819–20825.

Sinogeikin, S.V., Bass, J.D., Katsura, T., 2001. Single-crystal elasticity of γ-$(Mg_{0.91}Fe_{0.09})_2SiO_4$ to high pressures and to high temperatures. Geophys. Res. Lett. 28, 4335–4338.

Speziale, S., Duffy, T.S., 2002. Single-crystal elastic constants of fluorite (CaF_2) to 9.3 GPa. Phys. Chem. Minerals 29, 465–472.

Suzuki, I., 1975. Thermal expansion of periclase and olivine, and their anharmonic properties. J. Phys. Earth 23, 145–159.

Suzuki, I., Ohtani, E., Kumazawa, M., 1979. Thermal expansion of γ-Mg_2SiO_4. J. Phys. Earth 27, 53–61.

Takahashi, E., Shimazaki, T., Tsuzaki, Y., Yoshida, H., 1993. Melting study of a peridotite KLB-1 to 6.5 GPa, and the origin of basaltic magmas. Phil. Trans. R. Soc. Lond. A 342, 105–120.

Utsumi, W., Funakoshi, K., Urakawa, S., Yamakata, M., Tsuji, K., Konishi, H., Shimomura, O., 1998. SPring-8 beamlines for high pressure science with multi-anvil apparatus. Rev. High Pres. Sci. Tech. 7, 1484–1486.

Vacher, P., Mocquet, A., Sotin, C., 1998. Computation of seismic profiles from mineral physics: the importance of the non-olivine components for explaining the 660 km depth discontinuity. Phys. Earth Planet.Int. 106, 275–298.

Wang, W., Takahashi, E., 2000. Subsolidus and melting experiments of K-doped peridotite KLB-1 to 27 GPa: its geophysical and geochemical implications. J. Geophys. Res. 105, 2855–2868.

Wang, Y., Weidner, D.J., Zhang, J., Gwanmesia, G.D., Liebermann, R.C., 1998. Thermal equation of state of garnets along the pyrope-majorite join. Phys. Earth Planet. Int. 105, 59–71.

Wang, Y., Weidner, D.J., Guyot, F., 1996. Thermal equation of state of $CaSiO_3$ perovskite. J. Geophys. Res. 101, 661–672.

Watanabe, H., 1987. Physico-chemical properties of olivine and spinel solid solutions in the system Mg_2SiO_4-Fe_2SiO_4. In: Manghnani, M.H., Syono, Y. (Eds.), High-Pressure Reserch in Mineral Physics. Am. Geophys. Union, Washington, DC, pp. 275–278.

Weidner, D.J., Wang, Y., 1998. Chemcal- and Clapeyron-induced buoyancy at the 660 km discontinuity. J. Geophys. Res. 103, 7431–7441.

Weidner, D.J., Sawamoto, H., Sasaki, S., Kumazawa, M., 1984. Single-crystal elastic properties of the spinel phase of Mg_2SiO_4. J. Geophys. Res. 89, 7852-7860.

Weidner, D.J., Wang, Y., Vaughan, M.T., 1994. Yield strength at high pressure and temperature.

Geophys. Res. Lett. 21, 753–756.

Wood, B.J., 2000. Phase transformations and partitioning relations in peridotite under lower mantle conditions. Earth Planet.Sci. Lett. 174, 341–354.

Yamanaka, T., 1986. Crystal structures of Ni_2SiO_4 and Fe_2SiO_4 as a function of temperature and heating duration. Phys. Chem. Minerals 13, 227–232.

Zerr, A., Reichmann, H., Euler, H., Boehler, R., 1993. Hydrostatic compression of γ-$(Mg_{0.6}, Fe_{0.4})_2SiO_4$ to 50.0 GPa. Phys. Chem. Minerals 19, 507–509.

Table 2-1.

Unit cell parameters of $(Mg_{0.91}Fe_{0.09})_2SiO_4$ ringwoodite at various *P*-*T* conditions

P^a_A (GPa)	P^b_S (GPa)	*T* (K)	Ringwoodite		Au
			a (Å)	*V* (Å^3)	V/V_0
S602 (MgO capsule)					
18.17(19)	18.69(19)	1273	7.9092(6)	494.77(11)	0.9413(8)
17.14(15)	17.52(15)	1073	7.9084(7)	494.61(14)	0.9402(6)
17.65(18)	18.15(18)	1273	7.9131(5)	495.50(10)	0.9436(8)
16.74(17)	16.98(17)	873	7.9050(6)	493.97(11)	0.9365(7)
15.66(17)	15.41(16)	300	7.8891(5)	491.00(8)	0.9266(6)
20.68(18)	21.24(18)	1273	7.8796(8)	489.22(15)	0.9309(7)
20.06(25)	20.47(25)	1073	7.8781(5)	488.96(10)	0.9283(10)
19.48(26)	19.71(26)	873	7.8746(7)	488.30(12)	0.9257(10)
19.08(33)	19.12(32)	673	7.8700(6)	487.44(12)	0.9225(12)
18.75(26)	18.59(25)	473	7.8642(6)	486.37(10)	0.9192(9)
18.71(27)	18.36(26)	300	7.8594(6)	485.47(11)	0.9156(9)
0.00(16)	0.00(16)	300	8.0876(5)	529.00(11)	1.0000(9)
S648 (NaCl capsule)					
0.00(13)	0.00(13)	300	8.0825(13)	528.01(26)	1.0000(8)
9.78(14)	9.94(14)	873	7.9841(6)	508.95(12)	0.9681(7)
9.13(18)	9.23(18)	673	7.9791(7)	507.99(13)	0.9646(9)
8.49(19)	8.50(19)	473	7.9749(5)	507.20(9)	0.9613(9)
8.18(18)	8.11(18)	300	7.9706(6)	506.38(11)	0.9574(8)
13.56(19)	13.78(19)	873	7.9392(6)	500.41(11)	0.9502(8)
12.97(15)	13.08(15)	673	7.9342(7)	499.48(13)	0.9470(7)
12.51(17)	12.48(17)	473	7.9297(6)	498.62(11)	0.9434(7)
12.19(19)	12.04(18)	300	7.9270(7)	498.12(14)	0.9401(8)
15.64(20)	15.99(20)	1073	7.9270(4)	498.12(7)	0.9467(9)
15.09(20)	15.32(20)	873	7.9215(6)	497.07(12)	0.9434(9)
14.53(16)	14.62(16)	673	7.9171(6)	496.26(11)	0.9404(7)
14.06(18)	14.00(17)	473	7.9134(6)	495.54(11)	0.9370(7)
13.88(18)	13.69(18)	300	7.9093(6)	494.77(11)	0.9334(7)
17.52(13)	17.90(13)	1073	7.9064(6)	494.23(12)	0.9386(5)
17.08(17)	17.32(17)	873	7.9009(8)	493.21(15)	0.9351(7)
16.53(15)	16.60(15)	673	7.8969(9)	492.46(18)	0.9323(6)
16.12(21)	16.02(20)	473	7.9822(10)	491.59(18)	0.9290(8)
15.82(14)	15.57(13)	300	7.8887(10)	490.93(18)	0.9260(5)
19.35(18)	19.75(18)	1073	7.8863(7)	490.47(13)	0.9311(7)
18.83(13)	19.06(13)	873	7.8818(10)	489.63(19)	0.9282(5)
18.35(15)	18.41(14)	673	7.8775(9)	488.84(16)	0.9252(5)
17.93(15)	17.78(14)	473	7.8737(11)	488.13(20)	0.9222(5)
17.82(17)	17.50(17)	300	7.8705(13)	487.54(24)	0.9187(6)
21.16(14)	21.57(14)	1073	7.8712(6)	487.67(10)	0.9241(5)
20.51(17)	20.73(17)	873	7.8676(4)	486.99(7)	0.9218(6)

19.94(16)	19.97(16)	673	7.8635(4)	486.23(7)	0.9194(6)
19.61(19)	19.43(18)	473	7.8593(5)	485.45(9)	0.9162(7)
19.49(21)	19.12(21)	300	7.8566(6)	484.95(10)	0.9129(7)
0.00(9)	0.00(9)	300	8.0841(6)	528.32(12)	1.0000(5)
S649 (NaCl capsule)					
4.22(14)	4.22(15)	873	8.0632(6)	524.22(12)	0.9992(9)
3.60(13)	3.61(14)	673	8.0565(8)	522.93(15)	0.9944(8)
3.08(12)	3.09(12)	473	8.0509(9)	521.83(18)	0.9892(7)
2.84(14)	2.83(14)	300	8.0466(6)	521.00(12)	0.9838(7)
0.00(10)	0.00(10)	300	8.0847(9)	528.43(18)	1.0000(6)

[a] Pressure scale by Anderson et al. (1989).

[b] Pressure scale by Shim et al. (2002).

Table 2-2.
Thermoelastic parameters of $(Mg_{0.91}Fe_{0.09})_2SiO_4$ ringwoodite using the HTBM equation of state

Parameter		
K_{T0} (GPa)	[187]	[187]
K'_T	4.4(1)	4.0(1)
$(\partial K_T/\partial T)_P$ (GPa K^{-1})	–0.028(5)	–0.015(5)
$\alpha = a + bT$		
a (10^{-5} K^{-1})	1.9(2)	2.1(2)
b (10^{-8} K^{-2})	1.2(4)	0.7(4)
P-Marker[a]	Au-A	Au-S

[a] Pressure was calculated from the equation of state of gold by Anderson et al. (1989) (Au-A) and Shim et al. (2002) (Au-S). V_0 is fixed to be 527.83 $Å^3$ in the calculation. Square brackets indicate fixed value in the calculation.

Table 2-3.
Thermoelastic parameters of $(Mg_{0.91}Fe_{0.09})_2SiO_4$ ringwoodite from the thermal pressure equation of state

Parameter		
K_{T0} (GPa)	[187]	[187]
K'_T	4.3(1)	3.9(1)
α_0 (10^{-5} K^{-1})	2.5(1)	2.4(1)
$(\partial K_T/\partial T)_V$ (GPa K^{-1})	–0.006(4)	0.006(4)
$(\partial K_T/\partial T)_P$ (GPa K^{-1})	–0.026(4)	–0.011(4)
$(\partial^2 P/\partial T^2)_P$ (GPa K^{-2})	[0]	[0]
P-Marker[a]	Au-A	Au-S

[a] Pressure was calculated from the equation of state of gold by Anderson et al. (1989) (Au-A) and Shim et al. (2002) (Au-S). V_0 is fixed to be 527.83 $Å^3$ in the calculation. Square brackets indicate fixed value in the calculation.

Table 2-4. Bulk modulus, its pressure derivative and its temperature derivative of ringwoodite

Composition	K_{T0} (GPa)	K'_T	$(\partial K_T/\partial T)_P$ (GPa K^{-1})	Method[b]	Pressure calibration[c]	References
Mg_2SiO_4	184(2)	[4.8]	–	HP-XRD	Ruby	Hazen (1993)
Mg_2SiO_4	[182.6]	[5.0]	–0.028(3)	HP-XRD	NaCl	Meng et al. (1993)
Mg_2SiO_4	182(3)	4.0(3)	–0.027(5)	HP-XRD	Ruby, Au-A	Meng et al. (1994)
Mg_2SiO_4	183(3)[a]	–	–	BS	–	Weidner et al. (1984)
Mg_2SiO_4	[183][a]	4.7[a]	–	US	RG	Rigden et al. (1991, 1992)
Mg_2SiO_4	184(3)[a]	–	–0.031(3)[a]	BS	–	Jackson et al. (2000)
$(Mg_{0.91}Fe_{0.09})_2SiO_4$	187(3)[a]	–	–	BS	–	Sinogeikin et al. (1998)
$(Mg_{0.91}Fe_{0.09})_2SiO_4$	187(3)[a]	4.1(3)[a]	–0.028(2)[a]	BS	Ruby	Sinogeikin et al. (2001)
$(Mg_{0.91}Fe_{0.09})_2SiO_4$	[187]	4.4(1)	–0.028(5)	HP-XRD	Au-A	This study, HTBM
$(Mg_{0.91}Fe_{0.09})_2SiO_4$	[187]	4.3(1)	–0.026(4)	HP-XRD	Au-A	This study, PTH
$(Mg_{0.75}Fe_{0.25})_2SiO_4$	192(3)[a]	–	–	BS	–	Sinogeikin et al. (1997)
$(Mg_{0.6}Fe_{0.4})_2SiO_4$	183(2)	5.4(2)	–	HP-XRD	Ruby	Zerr et al. (1993)
$(Mg_{0.4}Fe_{0.6})_2SiO_4$	203(2)	[4.8]	–	HP-XRD	Ruby	Hazen (1993)
$(Mg_{0.2}Fe_{0.8})_2SiO_4$	205(2)	[4.8]	–	HP-XRD	Ruby	Hazen (1993)
Fe_2SiO_4	200[a]	5.6[a]	–	US	RG	Rigden and Jackson (1991)
Fe_2SiO_4	207(3)	[4.8]	–	HP-XRD	Ruby	Hazen (1993)

[a] Converted from adiabatic values. [b] HP-XRD: X-ray diffraction at high-pressure, BS: Brillouin scttering, US: ultrasonic technique. [c] Pressure calibration is based on ruby fluorescence (Ruby), EOS of NaCl by Decker (1971) (NaCl), EOS of gold by Anderson et al. (1989) (Au-A) and registance gauge (RG). The properties derived in this study using high-temperature Birch-Murnghan (HTBM) EOS and thermal pressure (PTH) EOS are presented. Square brackets indicate fixed value in the calculation.

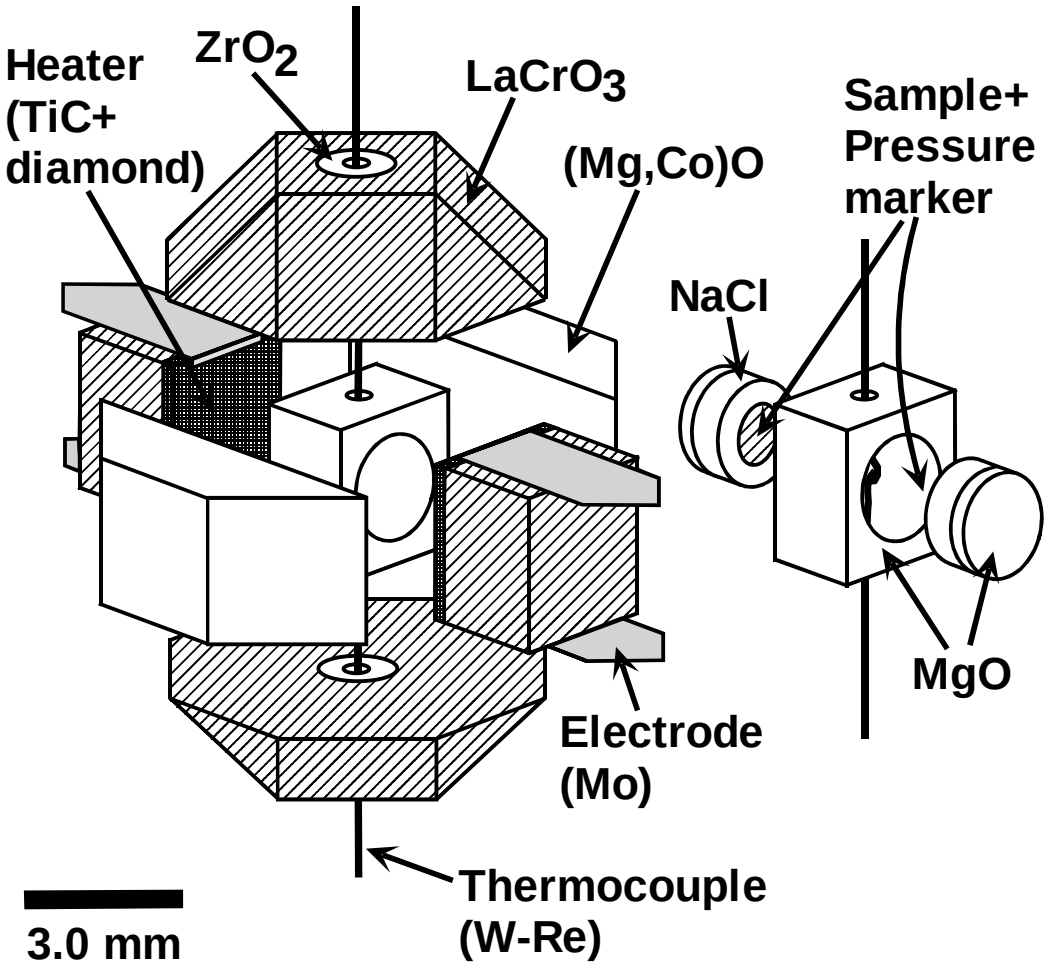

Fig. 2-1. Schematic illustration of the cell assembly. In the run S602, MgO capsule was used instead of NaCl capsule.

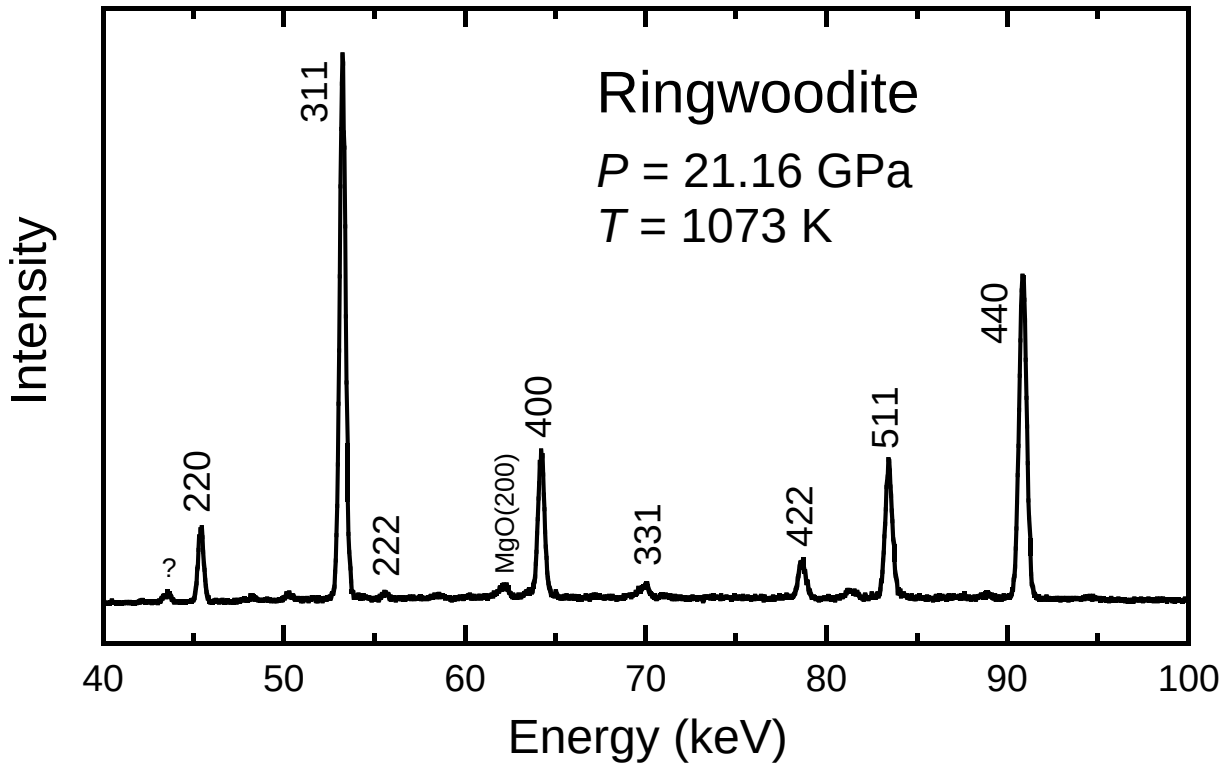

Fig. 2-2. Example of diffraction spectra of ringwoodite at 21.2 GPa (Anderson et al.'s scale) and 1073 K. A samll peak labeled "?" was unidentified.

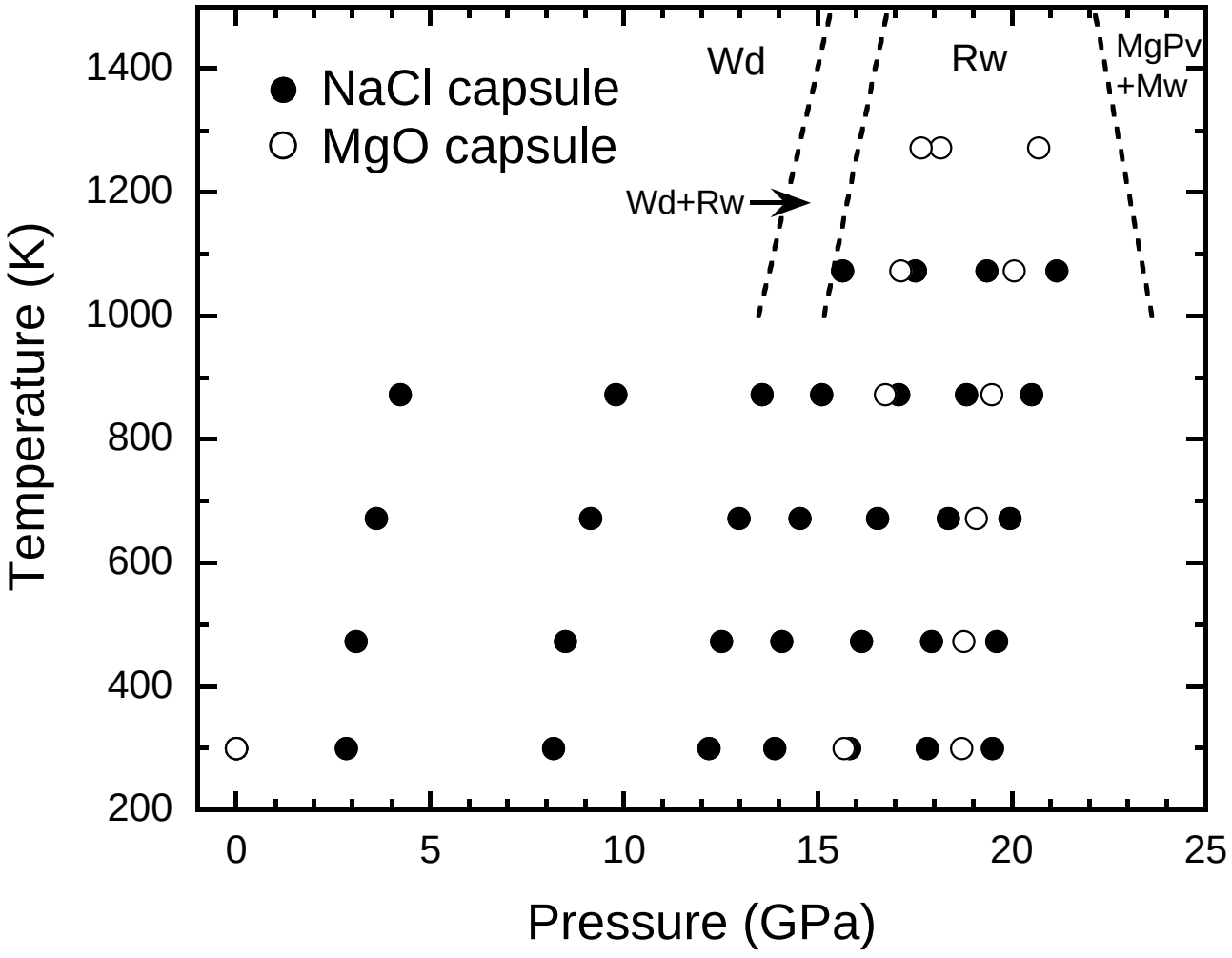

Fig. 2-3. Pressure-temperature conditions of present experiments. Solid and open symbols are data collected by using NaCl (experiment no. S648 and S649) and MgO (S602) capsules, respectively. The pressures were calculated using the Anderson et al. (1989) EOS for Au. Broken lines are estimated phase boundary in $(Mg_{0.91}Fe_{0.09})_2SiO_4$ composition consistent with Anderson et al.'s Au pressure scale (Akaogi et al., 1989; Ito and Takahashi, 1989; Irifune et al., 1998; Kuroda et al., 2000). Abbreviations are Wd: wadsleyite, Rw: ringwoodite, MgPv: Mg-rich perovskite, Mw: magnesiowustite.

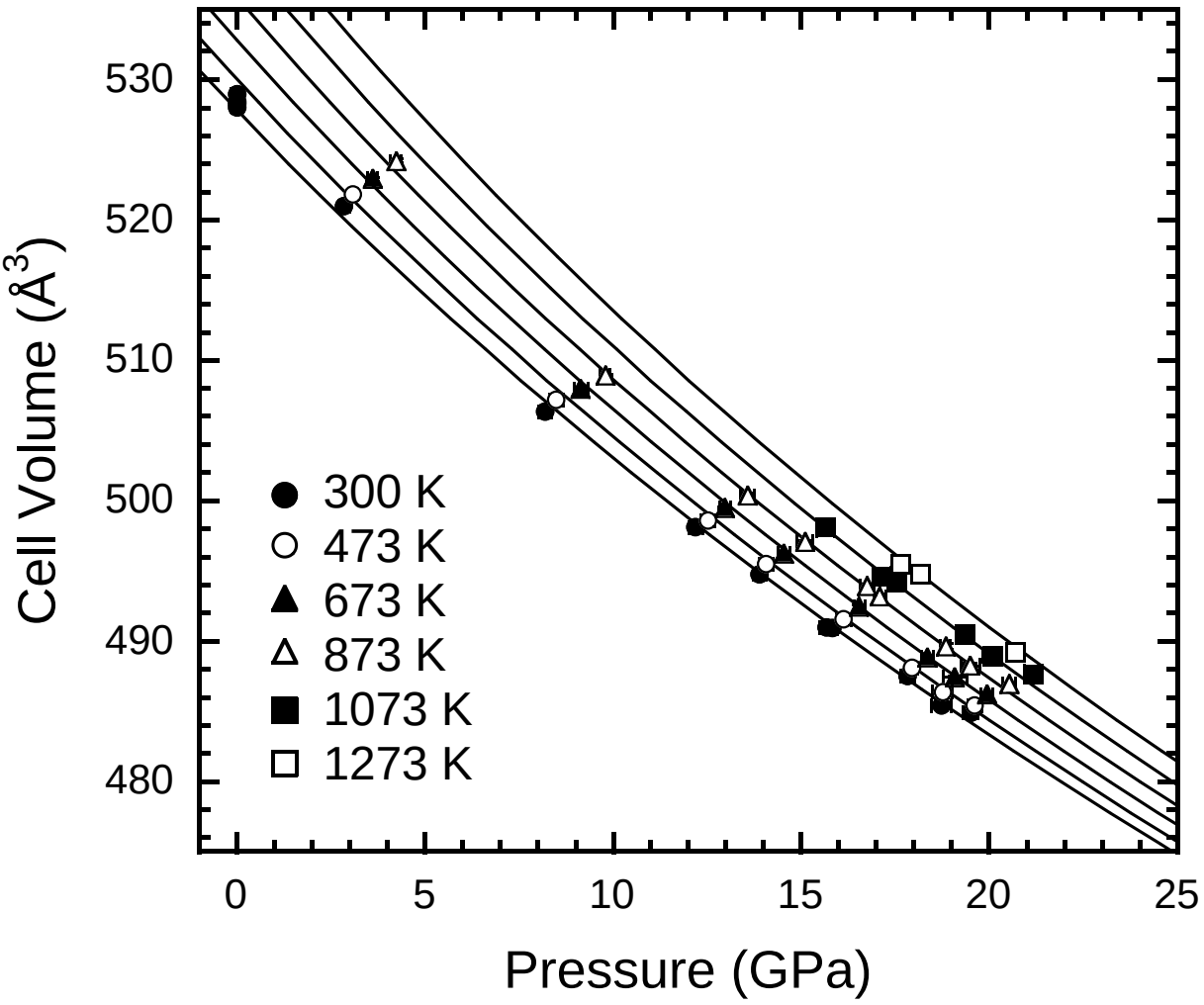

Fig. 2-4. *P-V-T* data of $(Mg_{0.91}Fe_{0.09})_2SiO_4$ ringwoodite with calculated isothermal compression curves. Pressures are based on Anderson's scale (Anderson et al., 1989). The isotherms (from lower cell volumes, 300, 473, 673, 873, 1073 and 1273 K) are calculatedfrom thermoelastic parameters derived with fixed value of K_{T0} = 187 GPa (Table 2-2).

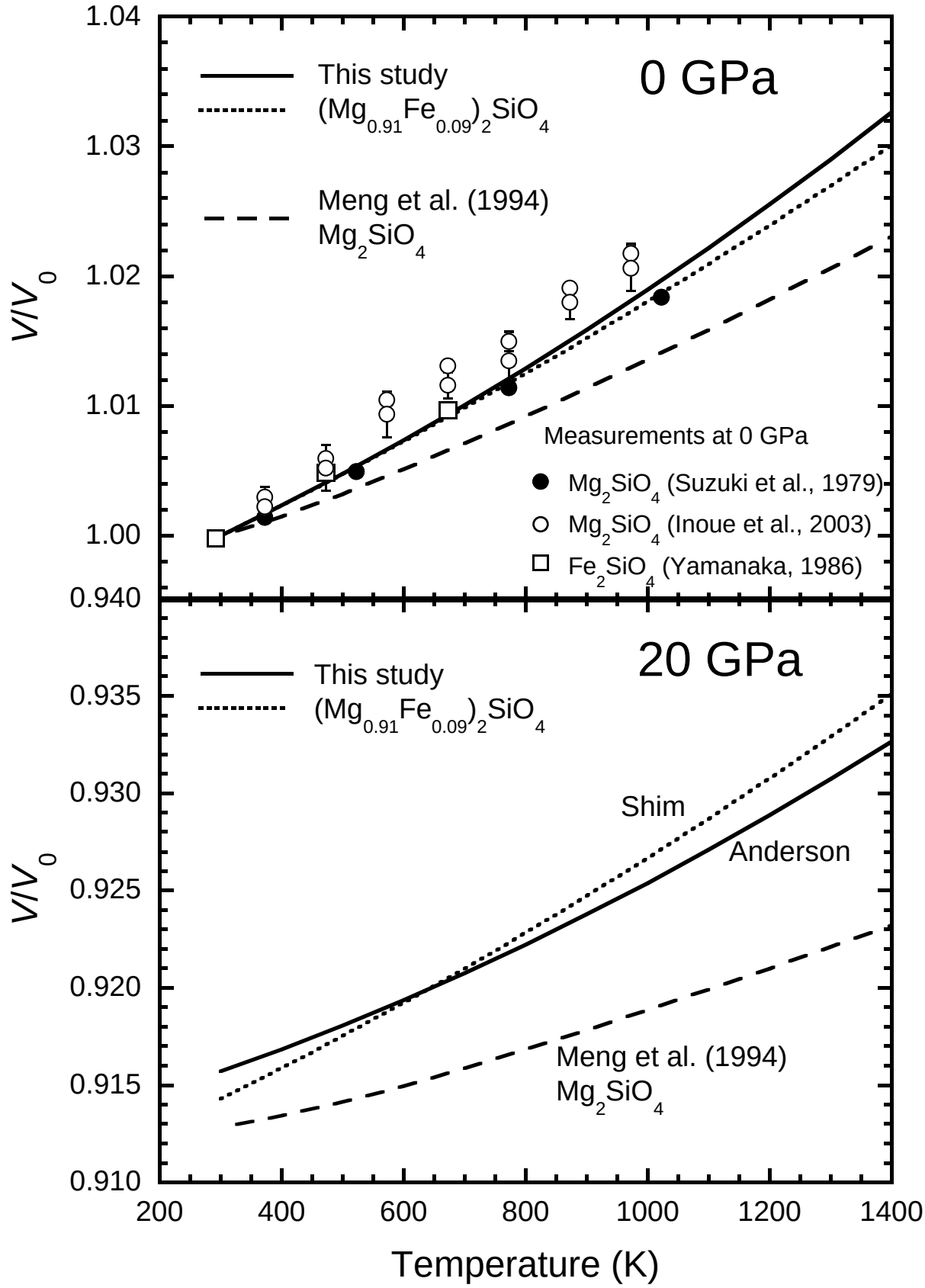
0 GPa
This study
(Mg0.91Fe0.09)2SiO4
Meng et al. (1994)
Mg2SiO4
Measurements at 0 GPa
Mg2SiO4 (Suzuki et al., 1979)
Mg2SiO4 (Inoue et al., 2003)
Fe2SiO4 (Yamanaka, 1986)
20 GPa
This study
(Mg0.91Fe0.09)2SiO4
Shim
Anderson
Meng et al. (1994)
Mg2SiO4
V/V0
Temperature (K)
1.04
1.03
1.02
1.01
1.00
0.940
0.935
0.930
0.925
0.920
0.915
0.910
200
400
600
800
1000
1200
1400

Fig. 2-5. Normalized volumes (V/V_0) of ringwoodite at 0 GPa (upper panel) and 20 GPa (lower panel) as a function of temperature. Solid and dotted lines are based on Anderson et al.'s (1989) and Shim et al.'s (2002) Au pressure scale, respectively. Broken lines are based on Meng et al.'s (1994) EOS of Mg_2SiO_4 ringwoodite, which is based on Anderson's pressure scale. Symbols are results of measurements at 0 GPa (1 bar) on Mg_2SiO_4 (solid circles; Suzuki et al., 1979, open circles; Inoue et al., 2003) and Fe_2SiO_4 (open square; Yamanaka, 1986) ringwoodites, respectively.

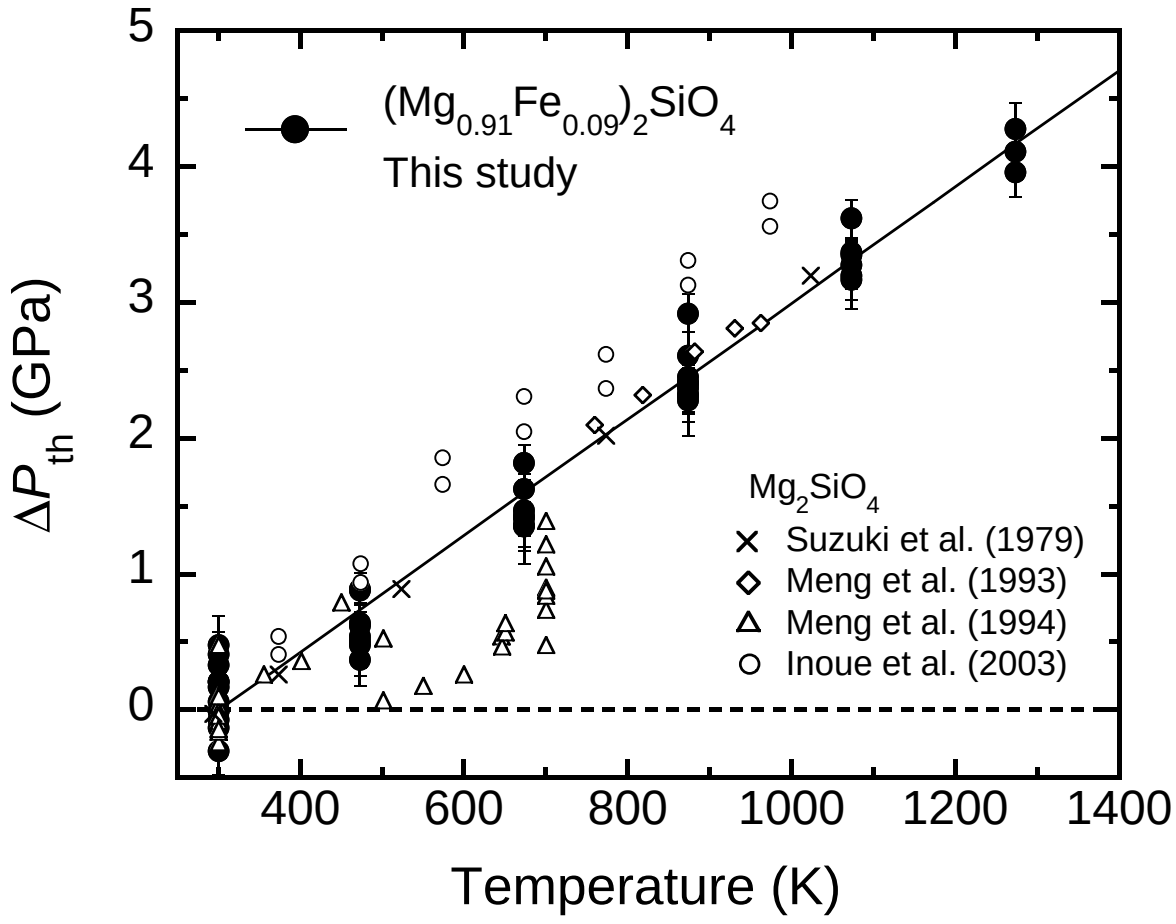

Fig. 2-6. Thermal pressure of ringwoodite against temperature. Solid circles are $(Mg_{0.91}Fe_{0.09})_2SiO_4$ ringwoodite (this study). Data for Mg_2SiO_4 ringwoodite are from Suzuki et al. (1979) (crosses), Meng et al. (1993) (open diamonds), Meng et al. (1994) (open triangles) and Inoue et al. (2003) (open circles). Solid line is calculated from the parameters listed in Table 2-3 for V = 498.9 A^3, which is the mean value of data by this study. The data of this study is based on Anderson et al.'s (1989) pressure scale.

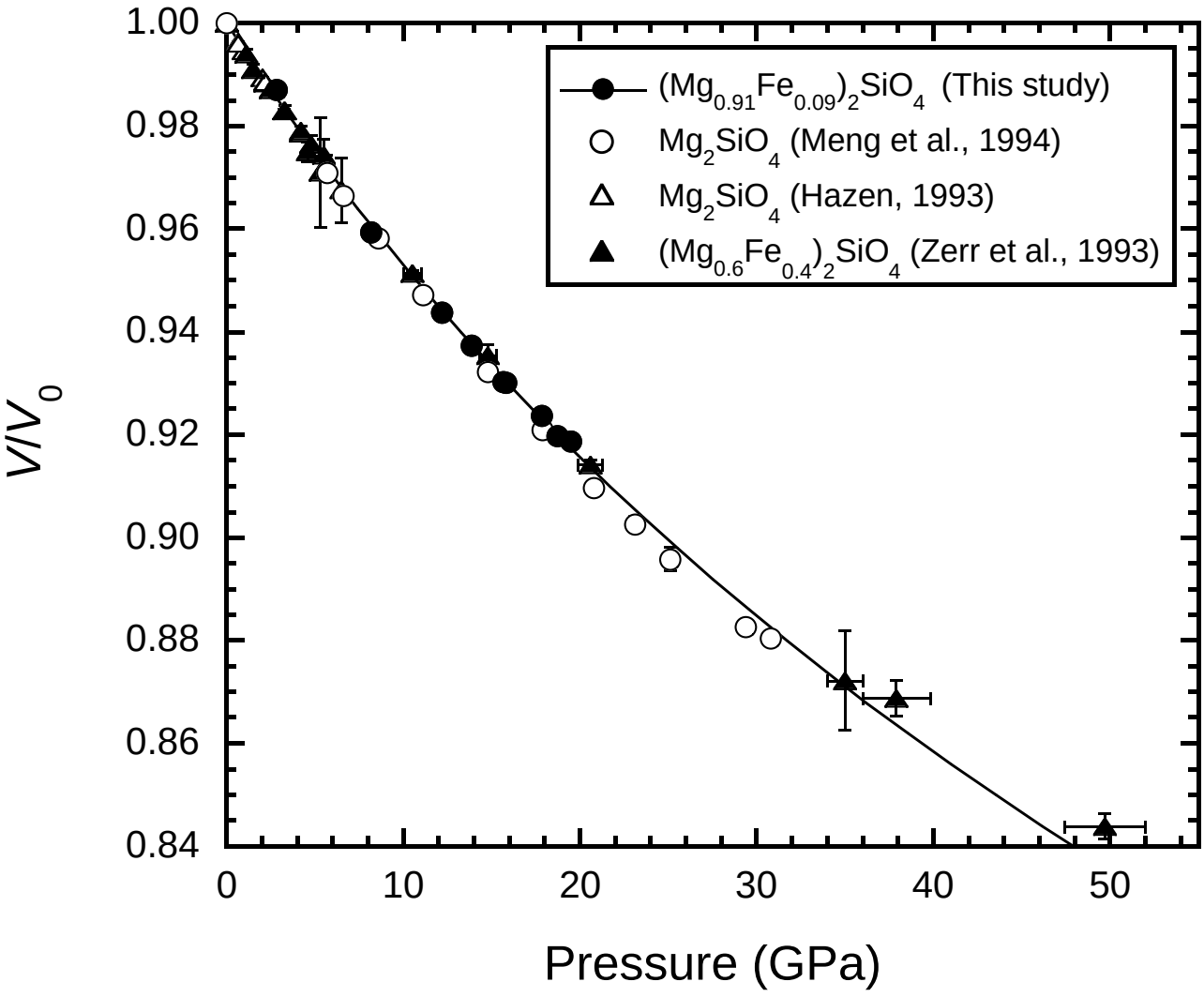

Fig. 2-7. Comparison of room temperature V/V_0 data of ringwoodites with Mg-rich composition. Solid circles, open circles, open triangles and solid triangles are data from this study ($(Mg_{0.91}Fe_{0.09})_2SiO_4$, Anderson et al.'s scale), Meng et al. (1994) (Mg_2SiO_4), Hazen (1993) (Mg_2SiO_4) and Zerr et al. (1993) ($(Mg_{0.6}Fe_{0.4})_2SiO_4$). Solid line is calculated compression curve with K_{T0} = 187 GPa and K'_T = 4.4 (Table 2-2).

Chapter 3
Thermal equation of state of majorite with MORB composition

Abstract

In-situ synchrotron X-ray diffraction experiments were conducted using SPEED-1500 multi-anvil press of SPring-8 on majoritic garnet synthesized from natural mid oceanic ridge basalt (MORB) at 19 GPa and 2200 K. Pressure-volume-temperature data were collected using newly developed high-pressure cell assembly at up to 21 GPa and 1273 K. A fit to high-temperature Birch-Murnaghan equation of state with fixed values of ambient cell volume V_0 = 1574.14(4) Å and pressure derivative of isothermal bulk modulus K'_T = 4 yielded an isothermal bulk modulus K_{T0} = 173(1) GPa, a temperature derivative of bulk modulus $(\partial K_T/\partial T)_P$ = −0.022(5) GPa K^{-1}, and a volumetric thermal expansivity $\alpha = a + bT$ with values of a = 2.0(3) × 10^{-5} K^{-1} and b = 1.0(5) × 10^{-8} K^{-2}. The derived thermoelastic parameters are consistent with those of pyrope. The density of oceanic crust and ambient mantle at conditions of the mantle transition zone (410–660 km depths) were calculated by using present results, previously reported thermoelastic parameters of related minerals and phase relation in MORB and pyrolite. As a result, the oceanic crust is denser than ambient mantle in entire range of the mantle transition zone along normal geotherm, and the density difference is insensitive to temperature at the lower part of transition zone.

3-1 Introduction

The mineralogy of the subducted oceanic crust in the deep mantle has been studied extensively by high-pressure and high-temperature phase equilibrium experiments on basaltic compositions (e.g. Irifune et al., 1986; Irifune and Ringwood, 1993; Hirose et al., 1999; Ono et

al., 2001). These studies revealed that majoritic garnet, whose composition is rich in pyroxene components, is the most abundant mineral in basaltic composition in the mantle transition zone (410–660 km depth), and that oceanic crust is denser than surrounding peridotitic mantle in the region.

Recently, the significance of recycled oceanic crust component in hotspot magma genesis has been pointed out (e.g. Hauri, 1996; Takahashi et al., 1998; Takahashi and Nakajima, 2002). However, it is sill not clear how the oceanic crust is entrained into mantle plume and, how the oceanic crust, denser than the ambient mantle, can ascend to Earth's surface. In order to clarify these processes, accurate thermal equation of state of majoritic garnet is very important because basalt consists of >90% majorite in the transition zone.

Thermoelastic properties of normal (non-majorite) garnets with various chemical composition have been widely investigated by several experimental methods (e.g. Isaak et al., 1992; Zhang et al., 1999; Wang and Ji, 2001; and references therein). In addition, recently, thermoelasticity of majoritic garnets in the system $Mg_3Al_2Si_3O_{12}$ (pyrope; Py)-$Mg_4Si_4O_{12}$ (majorite; Mj) were reported by some authors (e.g. Yagi et al., 1987; Morishima et al., 1999; Sinogeikin and Bass, 2002a, b; and references therein). Wang et al. (1998) and Morishima et al. (1999) conducted in situ X-ray observation experiments on $Py_{62}Mj_{38}$ and $Py_{20}Mj_{80}$ garnets, respectively, and determined their *P*-*V*-*T* equations of state. However, there are few data on majorite with natural basaltic composition. Faust and Knittle (1996) studied compressibility of majoritic garnet synthesized from natural tholeiitic basalt to 46 GPa using diamond-anvil cell, but their experimental conditions are limited to room temperature.

In this study, we measured the change of unit cell volume of majorite synthesized from natural oceanic ridge basalt (MORB) at pressure and temperature conditions up to 21 GPa and 1273 K with synchrotron radiation, and its thermal equation of state (EOS) was determined. Using the newly acquired EOS of MORB majorite together with previously reported themoelastic

parameters of MORB constituent minerals, we evaluate the density difference between oceanic crust and ambient mantle in the deep mantle.

3-2 Experimental procedures

Samples

Majorite was synthesized from natural abyssal basalt (ARP74, Table 3-1) using the SPI-1000, 1000 ton multi-anvil press at the Magma Factory, Tokyo Institute of Technology. The starting material (ARP74) was also used for high-pressure and high-temperature experiments by Aoki and Takahashi (2002), and its phase relation and phase chemistry are well determined at 5–14 GPa and 1473–1973 K. Its chemical composition is close to the primitive MORB composition. The powdered ARP74 was used for the synthesis experiment after drying at quartz-fayalite-magnetite buffer, 1 atm and 1273 K for 2 hours. According to previous high-pressure experiments on MORB (e.g. Irifune et al., 1986; Irifune and Ringwood, 1993), MORB consists of nearly single phase of majorite (with minor amount of stishovite, ~5–10%) at 15–20 GPa. Thus, the majorite suitable for the *P-V-T* experiments can be synthesized at these conditions from MORB. The powdered ARP74 was enclosed in a Re foil capsule, and experimental conditions were P = 19 GPa, T = ~2200 K and t = 10 min. Thermocouple was not used and temperature was estimated from power-temperature relation derived from previous experiments with similar cell assembly (Wang and Takahashi, 2000; Nishihara and Takahashi, 2001). Details of experimental technique were described in the previous papers.

Analysis with the JEOL-8800 microprobe and angular dispersive X-ray powder diffraction (XRD) with Cr Kα radiation (RINT2000) showed synthesis of majoritic garnet with minor amount of stishovite. Chemical composition of synthesized majorite is listed in Table 3-1. The SiO_2 content of the majorite is lower than that of ARP74 and most of other components are somewhat higher than that of the starting material (Table 3-1). These are due to the coexistence of

stishovite with majorite. Reason for lower K_2O content of majorite than that of ARP74 is not clear. Very small amount of K-bearing phase (e.g. K-hollandite, Wang and Takahashi, 1999), which is not detectable with microprobe, may be present. To obtain the composition in terms of garnet end-members, calculation was carried out by least squares fit neglecting minor elements and Fe^{3+}. Used end-member components are $M_3Al_2X_3O_{12}$ (PAS: pyralspite), $Ca_3Al_2X_3O_{12}$ (Grs: grossular), $M_4X_4O_{12}$ (Mj: majorite) and $Na_2MX_5O_{12}$ (NaMj: Na-rich majorite), where M = Mg + Fe + Mn and X = Si + Ti, and the result is listed in Table 3-2. Present MORB majorite consists of 70.9 mol% normal garnet (PAS + Grs), 17.3 mol% NaMj and 11.5 mol% Mj. If we calculate pyrope (Py), almandine (Alm) and spessartine (Spe) contents from the product of PAS content and molar ratio of Mg, Fe and Mn, our MORB majorite consists of 24.7 mol% Py, 12.6 mol% Alm and 0.2 mol% Spe. The Mg# value (Mg# = 100Mg/(Mg+Fe) molar ratio) of the majorite is 66.3.

The unit-cell parameters of the MORB majorite was calculated to be a = 11.6327(10) Å and V = 1574.14(4) Å from the positions of 10 X-ray diffraction peaks (400, 420, 332, 422, 431, 521, 611, 444, 640 and 642) obtained with angular dispersive XRD.

P-V-T experiments

P-V-T experiments were conducted using the SPEED-1500 apparatus installed on a synchrotron beam line (BL04B1) at the SPring-8, Hyogo, Japan. Detail about this system was described by Utsumi et al. (1998). The MORB majorite was packed into NaCl or MgO capsule with pressure marker (mixture of Au and MgO, 1:4 by weight) and $(Mg_{0.91}Fe_{0.09})_2SiO_4$ ringwoodite separately, and these samples were compressed in the same high-pressure cell (see Fig. 3-1). The *P-V-T* experiments on the majorite and the ringwoodite were conducted simultaneously. The results on the ringwoodite are reported by Nishihara et al. (2003b) (Chapter 2), and detailed experimental procedures are described in the paper.

For *P-V-T* experiments, we used newly developed cell assembly with $LaCrO_3$ pressure medium, a pair of TiC + diamond disk heater and W5%Re-W26%Re thermocouple (see Fig. 2-1 of Chapter 2). The X-ray CCD image of high-pressure cell assembly at ~8 GPa is shown in Fig. 3-1. The samples and pressure marker were placed horizontally. It enables us to observe two (or more) different samples even when the anvil gap is extremely narrowed (~0.3 mm) at the highest pressures. The diffracted X-rays from the sample were collected at a fixed 2θ angle of ~5.6° by the energy dispersive method. Typical exposure times for collecting diffraction patterns of sample and pressure marker were 400 and 200 s, respectively.

Fig. 3-2 shows an example of the X-ray diffraction spectra of the MORB majorite. The unit-cell parameters were calculated from positions of five diffraction peaks (400, 332, 611, 444 and 640) by least squares technique. The pressure was determined from the observed cell volume of Au calculated from four diffraction lines 111, 200, 220, and 311 by using thermal equation of state of Au (Anderson et al., 1989; Shim et al., 2002). An experiment with MgO sample capsule (experiment no. S602) and two experiments with NaCl capsule (S648 and S649) were carried out. We used only the XRD data collected after heating to 1273 K in MgO capsule. In the experiments with NaCl capsule, the data after heating to above 873 K were used. These experimental run products are considered to be under nearly hydrostatic conditions according to Weidner et al. (1994).

3-3 Results and discussion

Thermal equation of state

The unit-cell parameters of majorite with MORB composition at various *P-T* conditions are given in Table 3-3. Fig. 3-3 shows the volume data with calculated isothermal compression curves.

The high-temperature Birch-Murnaghan (HTBM) equation of state is often used to fit the

P-*V*-*T* data (e.g. Funamori et al., 1996; Wang et al., 1998; Chapter 1 and 2). The third-order Birch-Murnaghan equation of state is given by the following expression:

$$P = 3/2K_T\left[\left(V_{0T}/V\right)^{7/3} - \left(V_{0T}/V\right)^{5/3}\right]\left\{1 + 3/4\left(K_T' - 4\right)\left[\left(V_{0T}/V\right)^{2/3} - 1\right]\right\} \quad (1)$$

where K_T, V_{0T}, V and K'_T are the isothermal bulk modulus, zero-pressure volume, high-pressure volume, and pressure derivative of K_T, respectively. The temperature effects for K_T and V_{0T} are expressed as follows:

$$K_T = K_{T0} + \left(\partial K_T/\partial T\right)_P\left(T - 300\right) \quad (2)$$

$$V_{0T} = V_0 \exp\left[\int_{300}^{T} \alpha dT\right] \quad (3)$$

where $(\partial K_T/\partial T)_P$, V_0 and α are the temperature derivative of the bulk modulus, volume at room condition and the volumetric thermal expansion at atmospheric pressure, respectively. The K'_T and $(\partial K_T/\partial T)_P$ values are assumed to be constant. The V_0 was fixed to the value determined by angle dispersive X-ray diffraction (V_0 = 1574.14 Å^3) in the calculation.

The experimental *P*-*V*-*T* data (Table 3-3) were fitted to HTBM equation of state, and results are listed in Table 3-4. The fits without constraint on K_{T0} and K'_T yielded relatively high values for pressure derivative of K_{T0} (K'_T = 6.0(5), Table 3-4). However, it is well known that there is a trade-off between the value of K_{T0} and K'_T in calculating these properties from *P*-*V* data, and in many cases, the accuracy of derived parameters are not good enough (e.g. Bass et al., 1981). Because of limited precision of volume data, we cannot resolve both K_{T0} and K'_T values with confidence. We also calculated the thermoelastic parameters by fixing K'_T = 4 and 5 (Table 3-4), which is most common value for mantle minerals. K'_T = 4 corresponds to a second-order

Birch-Murnaghan EOS. Evaluation on reported K'_T values for majorite garnet with various techniques (e.g. Brillouin scattering, ultrasonic technique, etc, see Table 3-5) will be made in the discussion.

As discussed by Funamori et al. (1996) and Nishihara et al. (2003b) (Chapter 2), choice of pressure scale significantly affects thermoelastic parameters derived by *P-V-T* experiments. The pressure scale of Au by Anderson et al. (1989) is based on the measured elastic and thermodynamic properties of Au to 550 K at 0 GPa, while recent Au pressure scale by Shim et al. (2002) is based on the inversion of quasi-hydrostatic compression and shock wave data. We also calculated thermoelastic parameters of MORB majorite by using pressure values based on Shim et al.'s pressure scale (listed in Table 2-1 of Nishihara et al., 2003b, Chapter 2). The results are also listed in Table 3-4. The absolute value of $(\partial K_T/\partial T)_P$ is significantly lowered ($(\partial K_T/\partial T)_P$ = –0.022 GPa K^{-1} for Anderson et al.'s scale and –0.015 GPa K^{-1} for Shim et al.'s scale, at $K'_T = 4$) by the change of pressure scale, while other parameters are almost consistent.

Comparison with previous studies

Fig. 3-4 shows comparison of room temperature V/V_0 data of majorite bearing garnets and pyrope. Their bulk moduli (K_{T0}) and their pressure derivatives (K'_T) are listed in Table 3-5. Solid line in Fig. 3-4 is calculated compression curve with K_{T0} = 173 GPa and K'_T = 4 (Table 3-4). Faust and Knittle (1996) measured compressibility of majoritic garnet synthesized at 21 GPa from natural tholeiitic basalt to 46 GPa using diamond-anvil cell. Their results depicted in Fig. 3-4 (basaltic majorite) scatter significantly and show extremely large V/V_0 values at >20 GPa. As a result, their K_{T0} value is also extremely large (K_{T0} = 226(9) GPa). On the contrary, the compression curve for the MORB majorite made from similar basalt composition (this study) agrees with other garnets (see Fig. 3-4). The discrepancy in Faust and Knittle's (1996) experiments is most probably due to effect of nonhydrostaticity (e.g. uniaxial stress) in the high-

pressure cell. They used the methanol-ethanol-water mixture for the pressure medium without annealing, but that freezes above ~15 GPa (Sinogeikin and Bass, 2000). Moreover, Faust and Knittle's (1996) V_0 value is relatively low in spite of its high Ca content (Table 3-1). This may also be responsible for their results.

The compressibility of our MORB majorite is quite consistent with that of Py (pyrope; Zhang et al., 1998, 1999), while Py-Mj ($Mg_4Si_4O_{12}$) solid solutions ($Py_{62}Mj_{38}$ and $Py_{20}Mj_{80}$ by Wang et al., 1998 and Morishima et al., 1999, respectively) are slightly more compressible than MORB majorite. Na-rich majorite (NaMj; $Na_{1.88}Mg_{1.18}Si_{4.94}O_{12}$ by Hazen et al., 1994) seems to be slightly stiffer than MORB majorite and pyrope. However, bulk modulus of the same NaMj specimen determined by Brillouin scattering at ambient condition (Pacalo et al., 1992) is significantly lower than that of Hazen et al. (1994) which was determined by X-ray diffraction to 4.7 GPa (Table 3-5). Thus, experiments on NaMj to higher-pressure are required to constrain its compressibility.

Table 3-5 summarizes bulk modulus, its pressure derivative and its temperature derivative of garnets determined with various experimental techniques. Adiabatic values (K_{S0}, K'_S and $(\partial K_S/\partial T)_P$) can be obtained by Brillouin scattering, impulsively stimulated scattering and ultrasonic technique. These values are converted to isothermal values (K_{T0}, K'_T and $(\partial K_T/\partial T)_P$) by using thermodynamically derived equations, which were used in previous studies (Speziale and Duffy, 2002; Nishihara et al., 2003b; Chapter 2). For the calculation, data on thermal expansivity (α) and Grüneisen parameter (γ_G) are collected from Skinner (1956) and Suzuki and Anderson (1983), respectively for the pyrope-rich and majorite bearing garnets, from Skinner (1956) and Watanabe (1982), respectively for almandine, and from Skinner (1956) and Isaak et al. (1992), respectively for grossular-rich garnets. Because temperature derivative of bulk modulus changes significantly by this adiabatic-isothermal conversion, this process is necessary for comparison of this property.

High-pressure X-ray diffraction is not a direct measurement of elastic moduli, and the trade-off between K_{T0} and K'_T makes it difficult to resolve the both values with confidence. Then, we will compare the values of K'_T obtained by direct measurements of elastic moduli at high-pressures. Compositional dependency of K'_T is not detectable due to large scatters in the reported data, but K'_T value seems to depend on experimental method. Recent studies with laser induced phonon spectroscopy (Brillouin scattering and impulsively stimulated scattering) on garnets at high-pressures generally result in K'_T = ~4, whereas studies with ultrasonic interferometry at high-pressures yield much higher values for K'_T (K'_T = ~5–6.5) (Table 3-5). Because of the following reasons, we believe that the K'_T value derived by laser induced phonon spectroscopy is more accurate. As described in Chai et al. (1997) and Sinogeikin and Bass (2000), K'_T = ~4 is well consistent with reported *P*-*V* data on Py. Solid pressure medium used in ultrasonic studies without annealing above 3 GPa may have caused the nonhydrostatic conditions. Moreover, ultrasonic measurement on polycrystalline sample may be suffered from porosity and grain-boundary scattering. Therefore, we prefer the thermoelastic parameters of MORB majorite derived with K'_T = 4.

Because pyrope (Py) is geophysically most important in the garnet end-members, its thermoelasticity has been studied most intensively and is well established. Various reports on the K_{T0} of Py (and Py dominant garnets) converge to K_{T0} = 170 ± 2 GPa (Table 3-5). $Mg_4Si_4O_{12}$ majorite (Mj) shows slightly lower K_{T0} value (160–165 GPa) compared to Py. The K_{T0} values of garnets in Py-Mj join are generally between that of Py and Mj. The K_{T0} values of almandine (Alm) and grossular (Grs) are generally 180 ± 5 and 170 ± 5 GPa, respectively. Therefore, it can be considered that the K_{T0} value of Py-rich garnet decreases with increasing Mj content and increases with increasing Alm content, and Grs content do not affect significantly. Present MORB majorite shows similar K_{T0} value (173(1) GPa at K_{T0} = 4) with that of Py. This should be due to trade-off between Mj and Alm contents. Two data are available for K_{T0} of Na-rich majorite

(NaMj), but they differ significantly (172(3) GPa, Brillouin scattering by Pacalo et al., 1992, 192(3) GPa, high–*P* XRD by Hazen et al., 1994), and we cannot discuss the effect of this component on K_{T0}.

Compositional dependency of $(\partial K_T/\partial T)_P$ value is also not clear due to the scatter of data (Table 3-5). Our $(\partial K_T/\partial T)_P$ value based on Anderson et al.'s (1989) pressure scale of Au is consistent with all the previous studies in Table 3-5 within the estimated error. However, the use of Shim et al.'s (2002) scale yields the lowest absolute value of $(\partial K_T/\partial T)_P$ (–0.015(4) GPa K^{-1}) in Table 3-5.

Fig. 3-5 shows comparison of thermal expansivity of garnets at 0 GPa. Measurements at 0 GPa on end-member garnets (Py, Alm and Grs, Skinner et al., 1956) show similar values regardless of the garnet chemistry. However, measurements of $Py_{73}Alm_{16}$ at 0 GPa by Suzuki and Anderson (1983) show slightly higher thermal expansivity than the other three end-member garnets. Thermal expansivity of $Py_{62}Mj_{38}$ by Wang et al. (1998) is similar to the 0 GPa value of Suzuki and Anderson (1983) for $Py_{73}Alm_{16}$. On the contrary, the thermal expansivity of the MORB majorite determined in this study is similar to 0 GPa values for the end-member garnets.

Density of oceanic crust in the mantle transition zone

Densities of oceanic crust and ambient mantle in the deep mantle is calculated, using the newly acquired EOS of MORB majorite, together with previously reported thermoelastic parameters of MORB and pyrolite constituent minerals. Here, composition of the oceanic crust and the mantle are assumed to be MORB and pyrolite, respectively. The EOS of MORB majorite established in this study and that of ringwoodite by Nishihara et al. (2003b) are used. These EOSs are determined by the *P-V-T* data collected in the same high-pressure experiments (see Fig. 3-1). Majorite and ringwoodite are most dominant mineral phases at the lower part of mantle transition zone in MORB and pyrolite compositions, respectively (e.g. Irifune and Ringwood, 1993; Hirose,

2002). Therefore, calculated density difference between MORB and pyrolite in this study is considered to be insensitive to the any experimental systematic errors.

Phase relations and mineral volume fractions in MORB and pyrolite are collected from high-pressure phase equilibrium studies: Irifune et al. (1986), Irifune and Ringwood (1993), Aoki and Takahashi (2002) for MORB, and Irifune (1987), Akaogi et al. (1989), Irifune and Isshiki (1998) for pyrolite. Thermoelastic parameters for related minerals are collected from this study (majoritic garnet in MORB), Nishihara et al. (2003a) (clinopyroxene in MORB, Chapter 1), Nakayama et al. (2002) (stishovite), Wang et al. (1996) (Ca-rich perovskite), Wang et al. (1998) (majoritic garnet in pyrolite), Zhao et al. (1998) (clinopyroxene in pyrolite), Fei et al. (1992) (wadsleyite), Meng et al. (1993) (wadsleyite) and Nishihara et al. (2003b) (ringwoodite, Chapter 2).

Fig. 3-6 shows calculated density changes of MORB and pyrolite (a) against depth along the normal geotherm (Brown and Shankland, 1981) and (b) against temperature at 600 km depth (P = 21.04 GPa). In this calculation, temperature dependency of mineral proportions is not considered. The density of pyrolite is generally consistent with seismic observations (PREM; Dziewonski and Anderson, 1981, ak135; Kennett et al., 1995). As shown previously (e.g. Irifune and Ringwood, 1993), MORB is denser than surrounding pyrolitic mantle in entire range of the mantle transition zone along normal geotherm. The density difference ($\Delta\rho = \rho_M - \rho_P$, where ρ_M and ρ_P are density of MORB and pyrolite, respectively) is smallest at ~550 km depth ($\Delta\rho$ = 0.12 g cm^{-3}), because wadsleyite-ringwodite transition had completed in pyrolite and Ca-rich perovskite does not appear in MORB at this condition. At 600 km depth, density of MORB decreases parallel to that of pyrolite with increasing temperature. The $\Delta\rho$ is nearly constant ($\Delta\rho$ = 0.13–0.14 g cm^{-3}) at 1100–2300 K and this depth (pressure). This is mainly due to the similar thermal expansivities of MORB majorite and ringwoodite at this pressure.

Recently, it has been pointed out that the oceanic crust component plays important role in

hotspot magma genesis (e.g. Hauri, 1996; Takahashi et al., 1998; Takahashi and Nakajima, 2002). However, it is sill not clear how the oceanic crust, denser than the ambient mantle, ascend to Earth's surface. Present results suggest that there is no density crossover between the oceanic crust and the ambient mantle in the lower part of transition zone even at high-temperatures. In spite of its high density, the block of oceanic crust may be brought up to the shallower mantle by the viscous force in the mantle plume (Yasuda and Fujii, 1998).

Acknowledgements

I am grateful to Prof. Eiichi Takahashi for his valuable advice, continuing encouragement, discussion and review of this manuscript. I thank I. Aoki, K. Funakoshi, T. Yagi, T. Uchida and N. Nishiyama for their advice on experimental techniques, and K. Matsukage, T. Iguchi, K. Nakayama, K. Hirose, T. Komabayashi and M. Shindo for their helpful support for the in situ X-ray diffraction experiments. The in situ X-ray diffraction experiments were performed by using the SPEED-1500 system at BL04B1 in SPring-8 (proposal no. 2000B0548-CD-np and 2001A0272-CD-np). The earlier stage of *P-V-T* experiments were carried out by using the MAX-90 system in Photon Factory at National Laboratory for High Energy Accelerator Research Organization. Y.N. is grateful for the Research Fellowships of the Japan Society of the Promotion of Science for Young Scientists.

References

Akaogi, M., Ito, E., Navrotsky, A., 1989. Olivine-modified spinel-spinel transitions in the system Mg_2SiO_4-Fe_2SiO_4: calorimetric measurements, thermochemical calculation, and geophysical application. J. Geophys. Res. 94, 15671–15685.

Anderson, O.L., Isaak, D.G., Yamamoto, S., 1989. Anharmonicity and the equation of state for gold. J. Appl. Phys. 65, 1534–1543.

Aoki, I., Takahashi, E., 2002. Density of MORB eclogite in the upper mantle. Phys. Earth Planet. Int (submitted).

Bass, J.D., Liebermann, R.C., Weidner, D.J., Finch, S.J., 1981. Elastic properties from acoustic and volume compression experiments. Phys. Earth Planet. Int. 25, 140–158.

Brown, J.M., Shankland, T.J., 1981. Thermodynamic parameters in the Earth as determined from seismic profiles. Geophys. J. R. astr. Soc. 66, 579–596.

Chai, M., Brown, J.M., Slutsky, L.J., 1997. The elastic constants of a pyrope-grossular-almandine garnet to 20 GPa. Geophys. Res. Lett. 24, 523–526.

Chen, G., Cooke, J.A., Gwanmesia, G.D., Liebermann, R.C., 1999. Elastic wave velocoties of $Mg_3Al_2Si_3O_{12}$-pyrope garnet to 10 GPa. Am. Mineral. 84, 384–388.

Conrad, P.G., Zha, C.-s., Mao, H.-k., Hemley, R.J., 1999. The high-pressure, single-crystal elasticity of pyrope, grossular, and andradite. Am. Mineral. 84, 374–383.

Dziewonski, A.M., Anderson, D.L., 1981. Preliminary reference Earth model. Phys. Earth Planet. Int. 25, 297–356.

Faust, J. and Knittle, E., 1996. The stability and equation of state of majoritic garnet synthesized from natural basalt at mantle conditions. Geophys. Res. Lett. 23, 3377–3380.

Fei, Y., Mao, H.-K., Shu, J., Parthasarathy, G., Bassett, W.A., Ko, J., 1992. Simultaneous high-P, high-T X ray diffraction study of β-$(Mg,Fe)_2SiO_4$ to 26 GPa and 900 K. J. Geophys. Res. 97, 4489–4495.

Funamori, N., Yagi, T., Utsumi, W., Kondo, T., Uchida, T., Funamori, M., 1996. Thermoelastic properties of $MgSiO_3$ perovskite determined by in situ X ray observations up to 30 GPa and 2000 K. J. Geophys. Res. 101, 8257–8269.

Gwanmesia, G.D., Chen, G., Liebermann, R.C., 1998. Sound velocities in $MgSiO_3$-garnet to 8 GPa. Geophys. Res. Lett. 25, 4553–4556.

Hauri, E.H., 1996. Major-element variability in the Hawaiian mantle plume. Nature 382, 415–

419.

Hazen, R.M., Downs, R.T., Conrad, P.G., Finger, L.W., Gasparik, T., 1994. Comparative compressibilities of majorite-type garnets. Phys.Chem.Minerals 21, 344–349.

Hirose, K., 2002. Phase transitions in pyrolitic mantle around 670-km depth: implications for upwelling of plumes from the lower mantle. J. Geophys. Res. 107, 10.1029/2001JB000597.

Hirose, K., Fei, Y., Ma, Y., Mao, H.-K., 1999. The fate of subducted basaltic crust in the Earth's lower mantle. Nature 397, 53–56.

Irifune, T., 1987. An experimental investigation of the pyroxene-garnet transformation in a pyrolite composition and its bearing on the constitution of the mantle. Phys. Earth Planet. Int. 45, 324–336.

Irifune, T., Ringwood, A.E., 1993. Phase transformations in subducted oceanic crust and buoyancy relationships at depths of 600–800 km in the mantle. Earth Planet. Sci. Lett. 117, 101–110.

Irifune, T., Isshiki, M., 1998. Iron partitioning in a pyrolite mantle and the nature of the 410-km seismic discontinuity. Nature 392, 702–705.

Irifune, T., Sekine, T., Ringwood, A.E., Hibberson, W.O., 1986. The eclogite-garnetite transformation at high pressure and some geophysical implications. Earth Planet. Sci. Lett. 77, 245–256.

Isaak, D.G., Anderson, O.L., Oda, H., 1992. High-temperature thermal expansion and elasticity of calcium-rich garnet. Phys. Chem. Minerals 19, 106–120.

Kennett, B.L.N., Engdahl, E.R., Buland, R., 1995. Constraints on seismic velocities in the Earth from traveltimes. Geophys. J. Int. 122, 108–124.

Liu, J., Chen, G., Gwanmesia, G., Liebermann, R.C., 2000. Elastic wave velocities of pyrope-majorite garnets ($Py_{62}Mj_{38}$ and $Py_{50}Mj_{50}$) to 9 GPa. Phys. Earth Planet. Int. 120, 153–163.

Meng, Y., Weidner, D.J., Gwanmesia, G.D., Liebermann, R.C., Vaughan, M.T., Wang, Y.,

Leinenweber, K., Pacalo, R.E., Yeganeh-Haeri, A., Zhao, Y., 1993. In situ high-P-T X ray diffraction studies on three polymorphs (α, β, γ) of Mg_2SiO_4. J. Geophys. Res. 98, 22199–22207.

Morishima, H., Ohtani, E., Kato, T., Kubo, T., Suzuki, A., Kikegawa, T., Shimomura, O., 1999. The high-pressure and temperature equation of state of a majorite solid solution in the system of $Mg_4Si_4O_{12}$-$Mg_3Al_2Si_3O_{12}$. Phys.Chem. Minerals 27, 3–10.

Nakayama, K., Nishihara, Y., Takahashi, E., Iguchi, T., Funakoshi, K., 2002. P-V-T equation of state of stishovite to 23 GPa and 1073 K. Phys. Earth Planet. Int. (in prep.).

Nishihara, Y., Takahashi, E., 2001. Phase relation and physical properties of an Al-depleted komatiite to 23 GPa. Earth Planet. Sci. Lett. 190, 65–77.

Nishihara, Y., Takahashi, E., Matsukage, K., Kikegawa, T., 2003a. Thermal equation of state of omphacite. Am. Mineral. 88, 80–86.

Nishihara, Y., Takahashi, E., Matsukage, K., Iguchi, T., Nakayama, K., Funakoshi, K., 2003b. Thermal equation of state of $(Mg_{0.91}Fe_{0.09})_2SiO_4$ ringwoodite. Phys. Earth Planet. Int., (submitted).

Oguri, K., Funamori, N., Uchida, T., Miyajima, N., Yagi, T., Fujino, K., 2000. Post-garnet transition in a natural pyrope: a multi-anvil study based on in situ X-ray diffraction and transmission electron microscopy. Phys. Earth Planet. Int. 122, 175–186.

Ono, S., Ito, E., Katsura, T., 2001. Mineralogy of subducted basaltic crust (MORB) from 25 to 37 GPa, and chemical heterogeneity of the lower mantle. Earth Planet. Sci. Lett. 190, 57–63.

Pacalo, R.E.G., Weidner, D.J., Gasparik, T., 1992. Elastic properties of sodium-rich majorite garnet. Geophys. Res. Lett. 19, 1895–1898.

Pavese, A., Diella, V., Pischedda, V., Merli, M., Bocchio, R., Mezouar, M., 2001. Pressure-volume-temperature equation of state of andradite and grossular, by high-pressure and -temperature powder diffraction. Phys. Chem. Minerals 28, 242–248.

Rigden, S.M., Gwanmesia, G.D., Liebermann, R.C., 1994. Elastic wave velocities of a pyrope-majorite garnet to 3 GPa. Phys. Earth Planet. Int. 86, 35–44.

Shim, S.-H., Duffy, T.S., Takemura, K., 2002. Equation of state of gold and its application to the phase boundaries near 660 km depth in Earth's mantle. Earth Planet. Sci. Lett. 203, 729–739.

Sinogeikin, S.V., Bass, J.D., 2000. Single-crystal elasticity of pyrope and MgO to 20 GPa by Brillouin scattering in the diamond cell. Phys. Earth Planet. Int. 120, 43–62.

Sinogeikin, S.V., Bass, J.D., 2002a. Elasticity of majorite and a majorite-pyrope solid solution to high pressure: implications for the transition zone. Geophys. Res. Lett. 29, 10.1029/2001GL013937.

Sinogeikin, S.V., Bass, J.D., 2002b. Elasticity of pyrope and majorite-pyrope solid solutions to high temperatures. Earth Planet. Sci. Lett. 203, 549–555.

Skinner, B.J., 1956. Physical properties of end-members of the garnet group. Am. Mineral. 41, 428–436.

Speziale, S., Duffy, T.S., 2002. Single-crystal elastic constants of fluorite (CaF_2) to 9.3 GPa. Phys. Chem. Minerals 29, 465–472.

Suzuki, I., Anderson, O.L., 1983. Elasticity and thermal expansion of a natural garnet up to 1,000 K. J. Phys. Earth 31, 125–138.

Takahashi, E., Nakajima, K., 2002. Melting process in the Hawaiian plume: an experimental study. In: Takahashi, E., Lipman, P.W., Garcia, M.J., Naka, J., Aramaki, S. (Eds.), Hawaiian Volcanoes: Deep Underwater Perspectives. Am. Geophys. Union, Washington, DC, pp. 403–418.

Takahashi, E., Nakajima, K., Wright, T.L., 1998. Origin of the Columbia River basalts: melting model of a heterogeneous plume head. Earth Planet. Sci. Lett. 162, 63–80.

Utsumi, W., Funakoshi, K., Urakawa, S., Yamakata, M., Tsuji, K., Konishi, H., Shimomura, O.,

1998. SPring-8 beamlines for high pressure science with multi-anvil apparatus. Rev. High Pres. Sci. Tech. 7, 1484–1486.

Wang, W., Takahashi, E., 1999. Subsolidus and melting experiments of a K-rich basaltic composition to 27 GPa: implication for the behavior of the potassium in the mantle. Am. Mineral. 84, 357–361.

Wang, W., Takahashi, E., 2000. Subsolidus and melting experiments of K-doped peridotite KLB-1 to 27 GPa: its geophysical and geochemical implications. J. Geophys. Res. 105, 2855–2868.

Wang, Y., Weinder, D.J., Guyot, F., 1996. Thermal equation of state of $CaSiO_3$ perovskite. J. Geophys. Res. 101, 661–672.

Wang, Y., Weidner, D.J., Zhang, J., Gwanmesia, G.D., Liebermann, R.C., 1998. Thermal equation of state of garnets along the pyrope-majorite join. Phys. Earth Planet. Int. 105, 59–71.

Wang, Z., Ji, S., 2001. Elasticity of six polycrystalline silicate garnets at pressure up to 3.0 GPa. Am. Mineral. 86, 1209–1218.

Watanabe, H., 1982. Thermochemical properties of synthetic high-pressure compounds relevant to the Earth's mantle. In: Akimoto, S., Manghnani, M.H. (Eds.), High-Pressure Research in Geophysics, CAPJ, Tokyo, pp. 441–464.

Webb, S.L., 1989. The elasticity of the upper mantle orthosilicates olivine and garnet to 3 GPa. Phys. Chem. Minerals 16, 684–692.

Weidner, D.J., Wang, Y., Vaughan, M.T., 1994. Yield strength at high pressure and temperature. Geophys. Res. Lett. 21, 753–756.

Yagi, T., Akaogi, M., Shimomura, O., Tamai, H., Akimoto, S., 1987. High pressure and high temperature equations of state of majorites. In: Manghnani, M.H., Syono, Y. (Eds.), High-Pressure Reserch in Mineral Physics. Am. Geophys. Union, Washington, DC, pp. 141–147.

Yagi, T., Uchiyama, Y., Akaogi, M., Ito, E., 1992. Isothermal compression curve of $MgSiO_3$ tetragonal garnet. Phys. Earth Planet. Int. 74, 1–7.

Yasuda, A., Fujii, T., 1998. Ascending subducted oceanic crust entrained within mantle plumes. Geophys. Res. Lett. 25, 1561–1564.

Zhang, L., Ahsbahs, H., Kutoglu, A., 1998. Hydrostatic compression and crystal structure of pyrope to 33 GPa. Phys. Chem. Minerals 25, 301–307.

Zhang, L., Ahsbahs, H., Kutoglu, A., Geiger, C.A., 1999. Single-crystal hydrostatic compression of synthetic pyrope, almandine, spessartine, grossular and andradite garnets at high pressures. Phys. Chem. Minerals 27, 52–58.

Zhao, Y., Von Dreele, R.B, Zhang, J.Z., Weidner, D.J., 1998. Thermoelastic equation of state of monoclinic pyroxene: $CaMgSi_2O_6$ diopside. Rev. High Pres. Sci. Tech. 7, 25–27.

Table 3-1.

Chemical composition of MORB and majorites

wt%	ARP74[a]	Majorite[b]	Majorite[c]
SiO_2	50.12	46.67	53.84
TiO_2	1.14	1.21	–
Al_2O_3	15.04	16.52	7.92
FeO[d]	9.06	9.61	23.42
MnO	0.15	0.18	–
MgO	9.62	10.58	2.93
CaO	11.80	12.70	10.74
Na_2O	2.00	2.28	–
K_2O	0.22	0.06	0.60
P_2O_5	0.12	0.18	–
Total	99.27	100.00	99.45

[a] Natural abyssal basalt used. [b] Synyjesized from ARP74 and used for present P-V-T experiments. Normalized to 100. [c] Faust and Knittle (1996); Synthesized from natural thoreiitic basalt. [d] Total Fe as FeO.

Table 3-2.
Mole percentages of end-member components

Cation[a] (O = 12)		Component	mol%[b]
X (Si+Ti)	3.467	$M_3Al_2X_3O_{12}$	37.5
Al	1.418	$Ca_3Al_2X_3O_{12}$	33.5
M (Mg+Fe+Mn)	1.747	$M_4X_4O_{12}$	11.5
Ca	0.992	$Na_2MX_5O_{12}$	17.3
Na	0.323		
SUM	7.947	SUM	99.8

[a] Minor elements are neglected. [b] Calculated by least squares fit. Mg# = 100Mg/(Mg+Fe) = 66.3.

Table 3-3.
Unit cell parameters of majorite with MORB composition at various P-T conditions

P [a] (GPa)	T (K)	a (Å)	V (Å^3)
S602 (MgO capsule)			
17.14(15)	1073	11.3601(29)	1466.0(11)
17.65(18)	1273	11.3646(15)	1467.8(6)
16.74(17)	873	11.3555(25)	1464.3(9)
15.66(17)	300	11.3382(20)	1457.6(8)
20.68(18)	1273	11.3133(14)	1448.0(6)
20.06(25)	1073	11.3080(17)	1445.9(6)
19.48(26)	873	11.3063(13)	1445.3(6)
19.08(33)	673	11.3013(9)	1443.4(3)
18.75(26)	473	11.2955(9)	1441.2(3)
18.71(27)	300	11.2889(9)	1438.7(3)
0.00(16)	300	11.6426(10)	1578.2(4)
S648 (NaCl capsule)			
0.00(13)	300	11.6388(5)	1576.6(2)
9.78(14)	873	11.4810(11)	1513.3(4)
9.13(18)	673	11.4741(9)	1510.6(4)
8.49(19)	473	11.4678(10)	1508.1(4)
8.18(18)	300	11.4619(8)	1505.8(3)
13.56(19)	873	11.4071(11)	1484.3(4)
12.97(15)	673	11.4024(8)	1482.5(3)
12.51(17)	473	11.3968(6)	1480.3(2)
12.19(19)	300	11.3913(8)	1478.2(3)
15.64(20)	1073	11.3882(11)	1476.9(4)
15.09(20)	873	11.3801(10)	1473.8(4)
14.53(16)	673	11.3752(10)	1471.9(4)
14.06(18)	473	11.3684(9)	1469.3(3)
13.88(18)	300	11.3622(6)	1466.8(2)
17.52(13)	1073	11.3525(6)	1463.1(2)
17.08(17)	873	11.3664(8)	1460.8(3)
16.53(15)	673	11.3406(8)	1458.5(3)
16.12(21)	473	11.3346(4)	1456.2(1)
15.82(14)	300	11.3293(4)	1454.1(2)
19.35(18)	1073	11.3229(10)	1451.7(4)
18.83(13)	873	11.3176(12)	1449.7(5)
18.35(15)	673	11.3121(14)	1447.5(5)
17.93(15)	473	11.3069(8)	1445.5(3)
17.82(17)	300	11.3019(10)	1443.6(4)
21.16(14)	1073	11.3019(7)	1443.6(3)
20.51(17)	873	11.2969(7)	1441.7(3)
19.94(16)	673	11.2924(8)	1440.0(3)
19.61(19)	473	11.2876(9)	1438.1(4)

19.49(21)	300	11.2839(10)	1436.7(4)
0.00(9)	300	11.6424(8)	1578.1(3)
S649 (NaCl capsule)			
4.22(14)	873	11.5975(7)	1559.9(3)
3.60(13)	673	11.5863(5)	1555.4(2)
3.08(12)	473	11.5767(7)	1551.5(3)
2.84(14)	300	11.5691(5)	1548.5(2)
0.00(10)	300	11.6273(7)	1572.0(3)

[a] Pressure is based on EOS of Au by Anderson et al. (1989) .

Table 3-4. Thermoelastic parameters of majorite with MORB composition

Parameter				
K_{T0} (GPa)	173(1)	166(1)	159(3)	170(1)
K'_T	[4]	[5]	6.0(5)	[4]
$(\partial K_T/\partial T)_P$ (GPa K^{-1})	–0.022(5)	–0.032(4)	–0.041(6)	–0.015(4)
$\alpha = a + bT$				
a (10^{-5} K^{-1})	2.0(3)	2.2(2)	2.3(2)	2.2(2)
b (10^{-8} K^{-2})	1.0(5)	1.4(5)	1.9(6)	0.7(4)
P-Marker[a]	Au-A	Au-A	Au-A	Au-S

[a] Pressure was calculated from the equation of state of gold by Anderson et al. (1989) (Au-A), Shim et al. (2002) (Au-S). V_0 is fixed to be 1574.14 $Å^3$ in the calculation.Square brackets indicate fixed value in the calculation.

Table 3-5. Bulk modulus, its pressure derivative and its temperature derivative of garnets

Composition[a]	K_{T0} (GPa)	K'_T	$(\partial K_T/\partial T)_P$ (GPa K^{-1})	P_{max}[d] (GPa)	T_{max}[e] (K)	References
X-ray diffraction at high-pressure						
MORB majorite	173(1)	[4]	–0.022(5)	21	1273	This study
Basaltic majorite	226(9)	[4]	–	42	300	Faust and Knittle (1996)
Py_{100}	171(2)	4.4(2)	–	33	300	Zhang et al. (1998, 1999)
Py_{100}	170(2)	[5]	–0.020(3)	6	1300	Wang et al. (1998); Yagi et al. (1987)
$Py_{62}Mj_{38}$	159(2)	4.9(6)	–0.019(4)	10	1073	Wang et al. (1998)
$Py_{48}Mj_{52}$	160(1)	[4]	–	6	1273	Yagi et al. (1987)
$Py_{20}Mj_{80}$	156(2)	4.4(3)	–0.019(3)	23	773	Morishima et al. (1999)
Mj_{100}	161(2)	[4]	–	10	300	Yagi et al. (1992)
$Py_{72}Alm_{17}Grs_{11}$	[166]	[4]	–0.016(1)	26	2000	Oguri et al. (2000)
Alm_{100}	185(3)	4.2(3)	–	21	300	Zhang et al. (1999)
$Alm_{82}Fs_{18}$	165(1)	[4]	–	6	1273	Yagi et al. (1987)
Grs_{100}	175(1)	[4.4]	–	12	300	Zhang et al. (1999)
Grs_{100}	168(2)	[4]	–0.016(3)	4	1000	Pavese et al. (2001)
CaMj	165(2)	[4]	–	5	300	Hazen et al. (1994)
NaMj	192(3)	[4]	–	5	300	Hazen et al. (1994)
Brillouin scattering[b]						
Py_{100}	170(2)	4.1(3)	–0.022(2)	20	1073	Sinogeikin and Bass (2000, 2002b)
$Py_{50}Mj_{50}$	166(3)	4.2(3)	–0.022(2)	13	1073	Sinogeikin and Bass (2002a, b)
$Py_{80}Mj_{20}$	162(3)	–	–0.022(2)	0	943	Sinogeikin and Bass (2002b)
Mj_{100}	165(3)	4.2(3)	–	15	300	Sinogeikin and Bass (2002a)
$Py_{95}Alm_3Grs_2$	171	3.2	–	9	300	Conrad et al. (1999)
$Grs_{98}Py_1$[c]	166	5.5	–	10	300	Conrad et al. (1999)
NaMj	172(3)	–	–	0	300	Pacalo et al. (1992)
Impulsively stimulated scattering[b]						
$Py_{52}Alm_{32}Grs_{16}$[c]	169(1)	4.1	–	20	298	Chai et al. (1997)
Ultrasonic technique[b]						
Py_{100}	170(2)	5.3(4)	–	10	300	Chen et al. (1999)
$Py_{62}Mj_{38}$	167(6)	5.3(2)	–	3	300	Rigden et al. (1994)
$Py_{62}Mj_{38}$	170(5)	6.2(5)	–	9	300	Liu et al. (2000)
$Py_{50}Mj_{50}$	169(5)	6.4(5)	–	8	300	Liu et al. (2000)
Mj_{100}	166(3)	6.7(4)	–	8	300	Gwanmesia et al. (1998)
$Py_{94}Alm_6$	169(1)	4.9(6)	–	3	300	Wang and Ji (2001)
$Py_{73}Alm_{16}$[c]	170(1)	–	–0.0269(1)	0	1000	Suzuki and Anderson (1983)
$Py_{62}Alm_{36}Grs_2$	172.1(4)	4.9(1)	–	3	295	Webb (1989)
Alm_{100}	174(1)	6.2(5)	–	3	300	Wang and Ji (2001)
Grs_{100}	165(3)	5.9(5)	–	3	300	Wang and Ji (2001)
$Grs_{97}Py_1$[c]	167(1)	–	–0.0209(1)	0	1350	Isaak et al. (1992)

[a] Py: pyrope ($Mg_3Al_2Si_3O_{12}$), Mj: majorite ($Mg_4Si_4O_{12}$), Alm: almandine ($Fe_3Al_2Si_3O_{12}$), Grs: grossular ($Ca_3Al_2Si_3O_{12}$), Fs: ferrosilite ($Fe_4Si_4O_{12}$), CaMj: $Ca_{0.49}Mg_{3.51}Si_4O_{12}$ garnet, NaMj: $Na_{1.88}Mg_{1.18}Si_{4.94}O_{12}$ garnet. [b] Converted from adiabatic values. [c] Minor components are neglected. [d] Maximum pressure in the experiments. [e] Maximum temperature in the experiments. Square brackets indicate fixed value in the calculation.

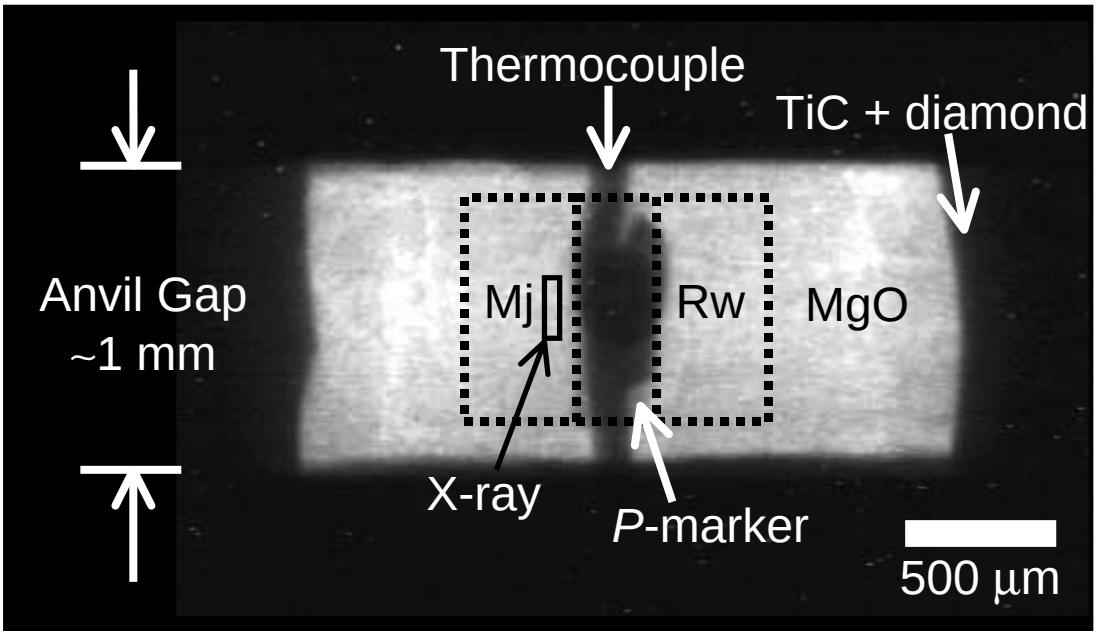

Fig. 3-1. An X-ray image of the high-pressure cell assembly for *P-V-T* experiments at ~8 GPa (experiment no. S602). The small rectangle represents the area of 0.05×0.2 mm, from which X-ray diffraction was collected. The thin layer of pressure marker was placed at the center of assembly and samples were placed at both outsides (Mj; MORB majorite, Rw; ringwoodite) horizontally.

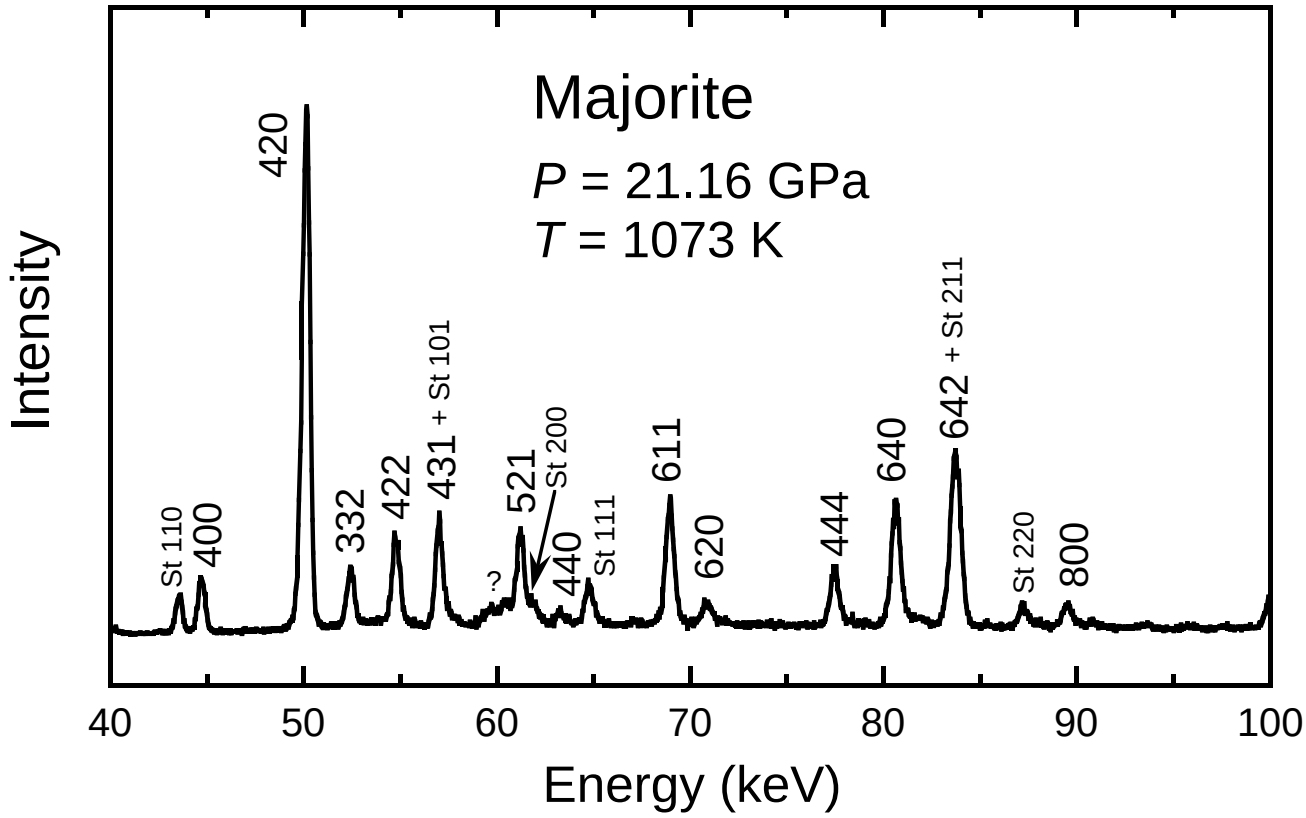

Fig. 3-2. An example of X-ray diffraction pattern of majorite with MORB composition at 21.16 GPa and 1073 K. Some weak diffraction peaks for stishovite (St), which coexists with majorite, are also detected.

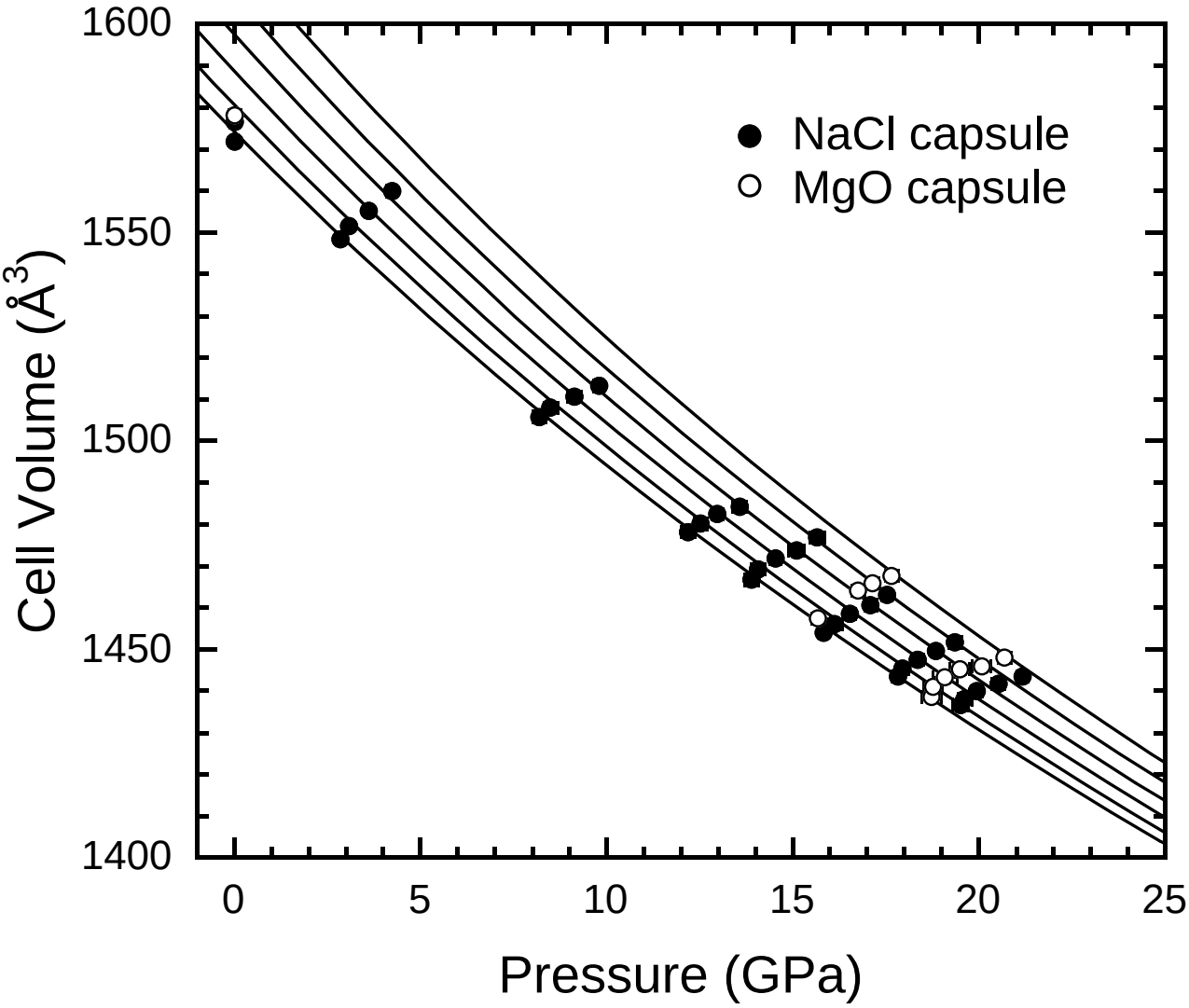

Fig. 3-3. *P-V-T* data of MORB majorite with calculated isothermal compression curves. Solid and open circles are data collected by using NaCl (S648 and S649) and MgO (S602) capsules, respectively. The isotherms (from lower cell volumes, 300, 473, 673, 873, 1073 and 1273 K) are calculated from thermoelastic parameters derived with fixed value of $K'_T = 4$ (Table 3-4).

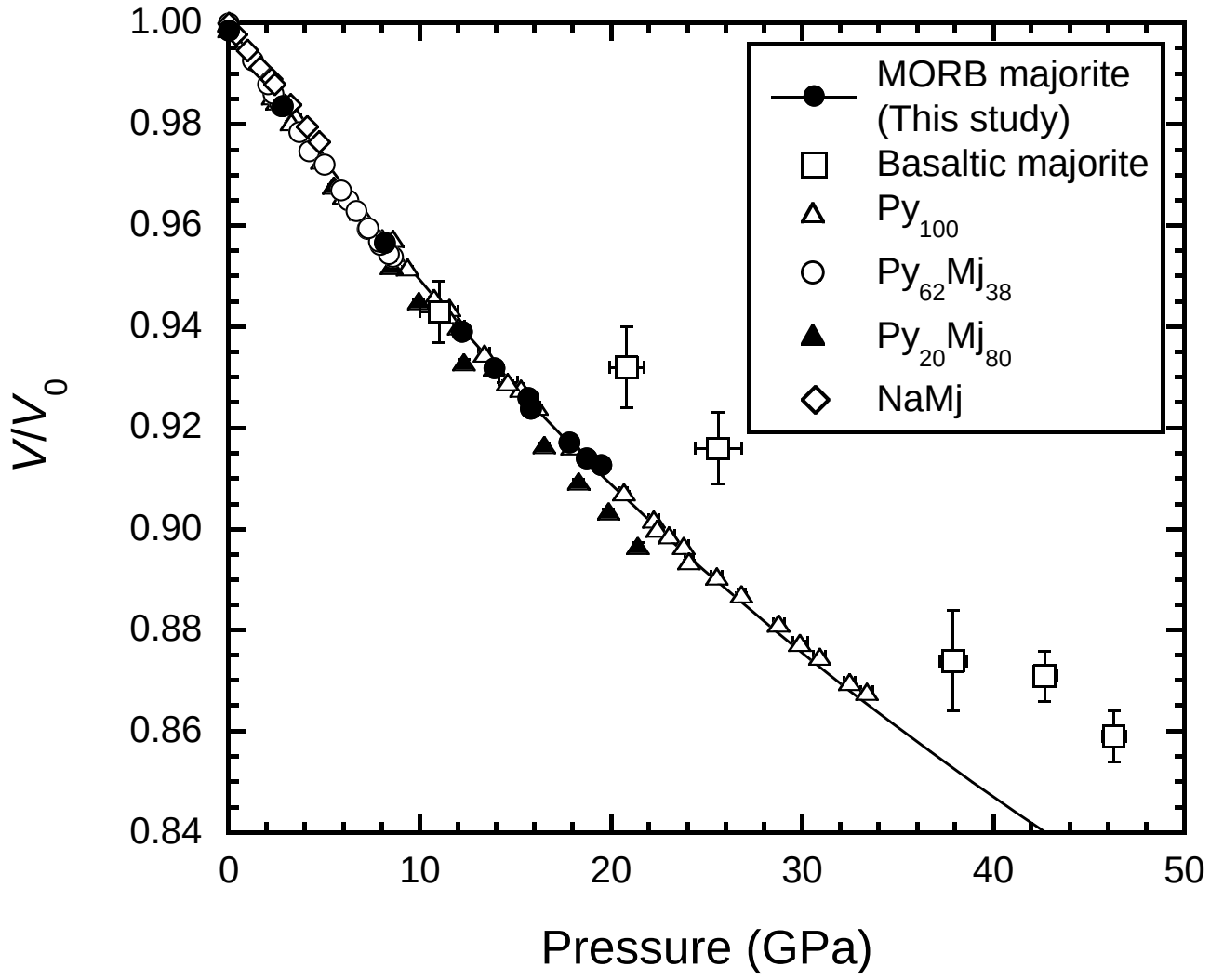

Fig. 3-4. Comparison of room temperature V/V_0 data of majorite bearing garnets and pyrope. Solid circles, open squares, open triangles, open circles, solid triangles and open diamonds are data from this study (MORB majorite), Faust and Knittle (1996) (basaltic majorite), Zhang et al. (1998, 1999) (Py_{100}), Wang et al. (1998) ($Py_{62}Mj_{38}$), Morishima et al. (1999) ($Py_{20}Mj_{80}$) and Hazen et al. (1994) (NaMj), respectively. Solid line is calculated compression curve with K_{T0} = 173 GPa and K'_T = 4 (Table 3-4).

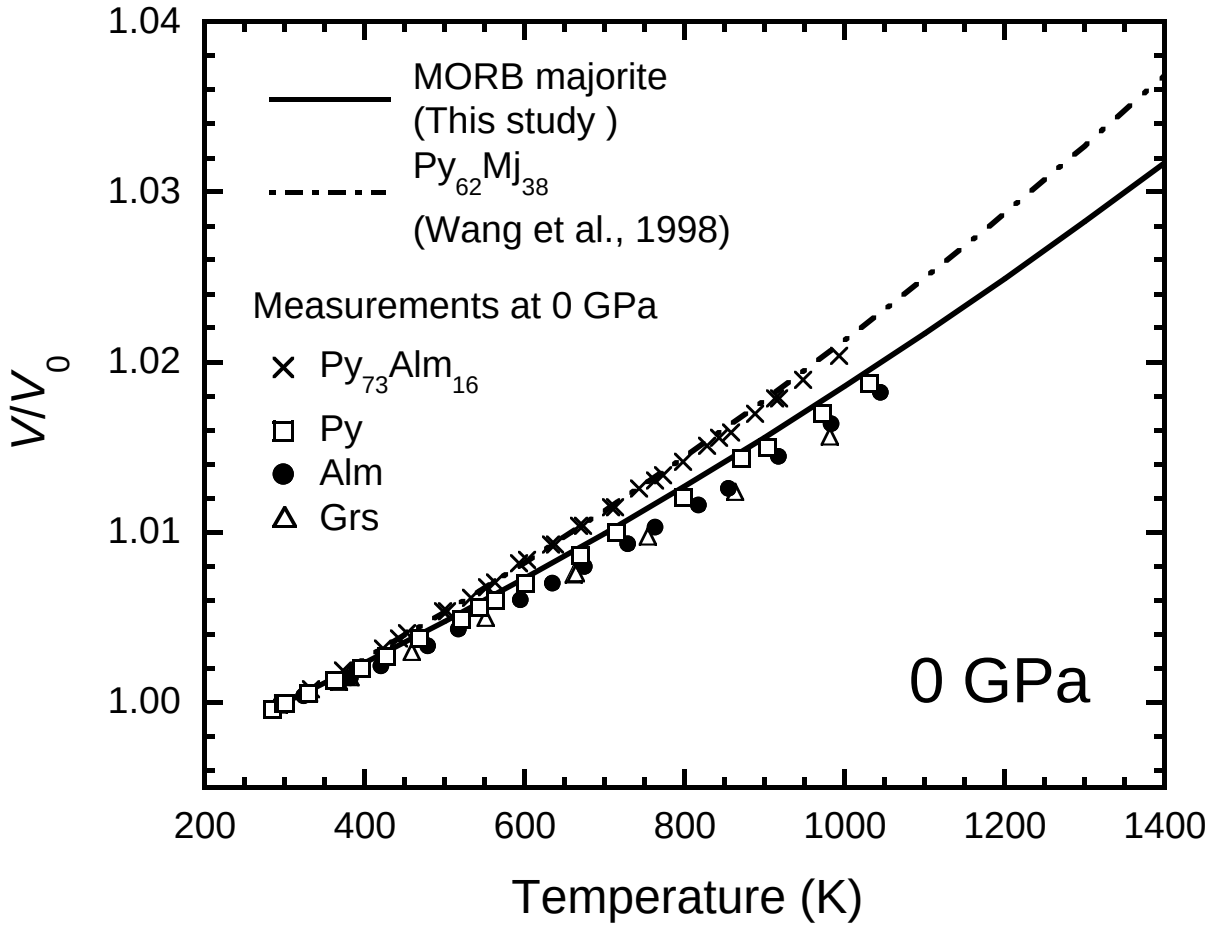

Fig. 3-5. Normalized volumes (V/V_0) of garnets at 0 GPa as a function of temperature. Solid and dashed dotted lines are calculated from thermal EOSs of present study (MORB majorite) and Wang et al. (1998) ($Py_{62}Mj_{38}$), respectively. Crosses are results of measurements at 0 GPa by Suzuki and Anderson (1983) ($Py_{73}Alm_{16}$), and open squares, solid circles and open triangles are results of measurements at 0 GPa by Skinner (1956) (Py, Alm and Grs).

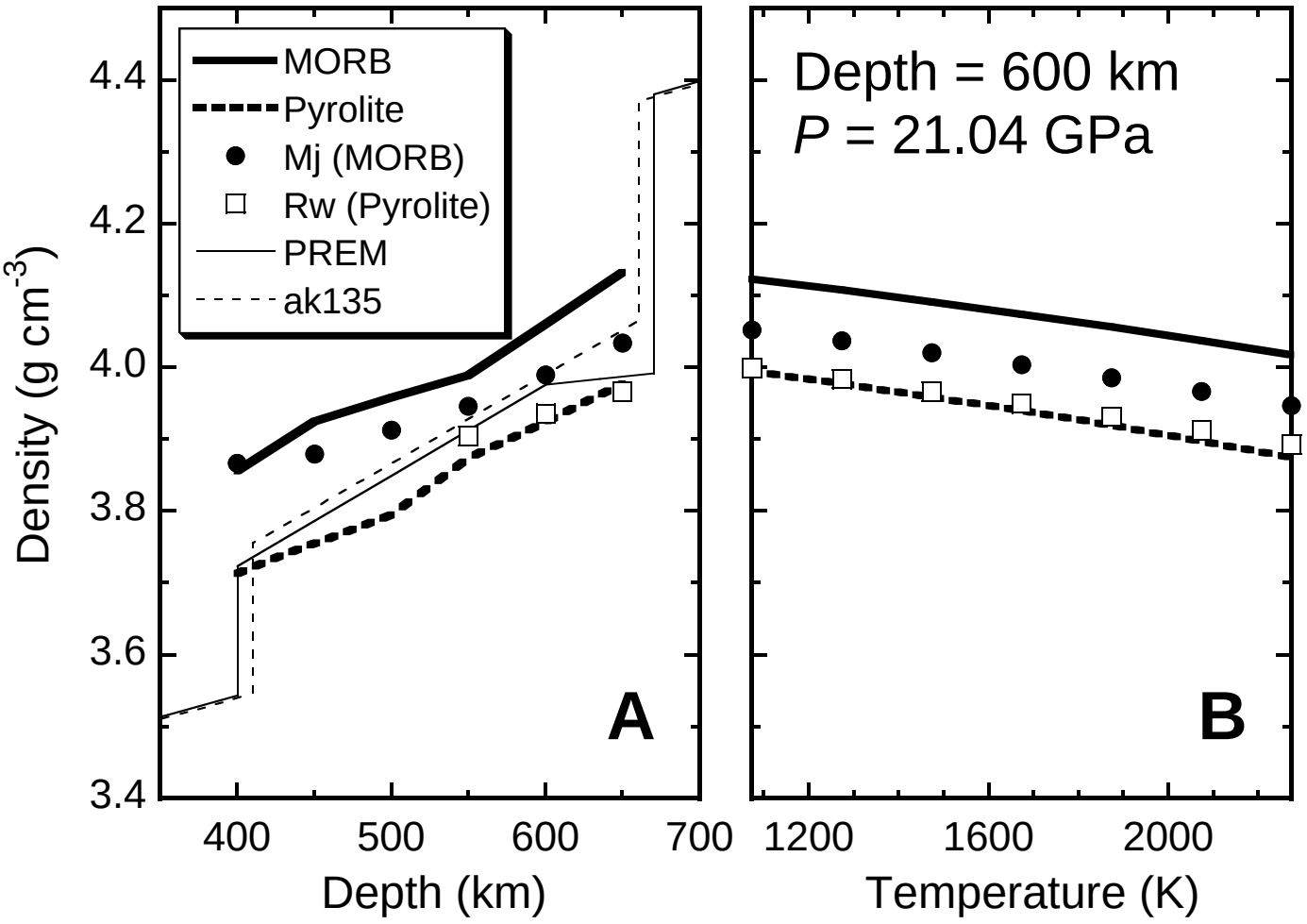

Fig. 3-6. Density changes of MORB and pyrolite (a) against depth along the normal geotherm (Brown and Shankland, 1981) and (b) against temperature at 600 km depth (P = 21.04 GPa). Bold solid and dashed lines are MORB and pyrolite, respectively. Solid circles and open squares are majorite in MORB and ringwoodite in pyrolite, respectively, which are calculated using equations of state of majorite (this study) and ringwoodite (Nishihara et al., 2002, Chapter 2). Seismic observations are shown as thin solid (PREM; Dziewonski and Anderson, 1981) and dashed (ak135; Kennett et al., 1995), lines.

Chapter 4
Density and elasticity of oceanic crust in the Earth's mantle

Abstract

Subducted oceanic crust would be the most important source of chemical and physical heterogeneity in the Earth's deep mantle. We investigated density (ρ) and seismic velocities (V_Φ, V_P and V_S) of the oceanic crust and ambient mantle up to 2900 km depth condition by calculations using previously reported phase equilibrium data of MORB (for the oceanic crust) and pyrolite (for the ambient mantle) and thermoelasrtic parameters of related minerals. At first, we constructed the phase diagrams of MORB and pyrolite as functions of pressure and temperature based on results of many experimental studies. Using these phase diagrams and a set of thermoelastic parameters, densities and seismic velocities (V_Φ, V_P and V_S) were calculated along normal, +300ºC and –300ºC geotherms based on third-order Birch-Murnaghan equation of state (third-order Eulerian finite strain) with temperature correction. For stishovite, which undergoes phase transition caused by elastic instability at 50–80 GPa, its shear modulus along the geotherm was derived by Landau free energy expansion and its extrapolation to high-temperature. The calculations show that the oceanic crust is slightly denser than the ambient mantle except for depths between 660 and 730 km. The V_Φ of the oceanic crust is similar to that of the ambient mantle except for at the depths ~600–730 km. The variations of V_P and V_S of the oceanic crust are generally similar to that of V_Φ except for those in the mid lower mantle. At the depths of ~1400–2100 km, V_P and V_S of the oceanic crust show drastic decrease due to the transition of stishovite (rutle-type to $CaCl_2$-type). At <~450 km depths, the ρ, V_Φ, V_P and V_S of the oceanic crust are more sensitive to temperature than those of ambient mantle due to temperature dependence of Cpx/Grt ratio in the oceanic crust. Behavior of the oceanic crust entrained within mantle plume is considered by calculation base on Stokes' law using the derived densities. The

low V_S of seismic scatterers in the mid lower mantle east of the Mariana and Izu-Bonin subduction zones is consistent with the drastic decrease in V_S of the oceanic crust. It is suspected that the subducted oceanic crust in the deep mantle would be detected more easily at ~1400–2100 km depth by seismic observation. Other seismic heterogeneity in the mid lower mantle reported by recent studies may be also related to the subducted oceanic crust.

4-1 Introduction

In the Earth's mantle, chemical heterogeneity has been created by differentiation at the mid oceanic ridges and at the subduction zone. From early stage of plate tectonics (~4.5Ga), basaltic crust bas been generated at the mid oceanic ridges and subducted as the upper most part of the oceanic plate into the Earth's mantle. Then, significant amount of basaltic material must be present in the today's Earth's deep mantle (Hofmann and White, 1982; Silver et al., 1988), and the basaltic material, which is rich in pyroxene and garnet components, should be the source of the most important chemical heterogeneity in the olivine-rich peridotitic mantle. Moreover, the significance of recycled old oceanic crust in hotspot magma genesis has been pointed out (e.g. Hauri, 1996; Takahashi et al., 1998; Takahashi and Nakajima, 2002). Thus, it is important to understand the dynamic behavior of basaltic material in the Earth's mantle, and its density and seismic velocities are most useful information for understanding this issue.

Kaneshima and Helffrich (1998, 1999) first found small scale seismic scattering bodies (~8 km thick) in the mid lower mantle by using short period seismic array data. It is possible that the seismic scatters in the mid lower mantle are caused by former basaltic oceanic crust in the deep mantle. Thus, knowledge about elasticity of basaltic material at high-pressure and high-temperature is important in order to assess the seismic heterogeneity.

Several experimental studies to determine the subsolidus phase relation at high-pressure and high-temperature has been carried out with mid oceanic ridge basalt (MORB) composition

(e.g. Irifune et al., 1986; Irifune and Ringwood, 1993; Ono et al., 2001) and with pyrolitic mantle composition (e.g. Akaogi and Akimoto, 1979; Irifune, 1987, 1994, Irifune and Isshiki, 1998; Hirose, 2002). These studies have revealed mineral proportion and phase chemistry in MORB and pyrolite compositions up to the upper most part of the lower mantle. Moreover, some authors investigated mineralogy in MORB and pyrolite at entire pressure range of the lower mantle (e.g. Kesson et al., 1994, 1998).

In order to evaluate density and seismic velocities (P- and S-wave velocities and bulk sound velocity) of oceanic crust in the Earth's deep mantle, we have determined thermal rquation of state of MORB and pyrolite constituent minerals (omphacite, ringwoodite and majoritic garnet, see Chapter 1–3). In Chapter 4, thermoelastic calculation is carried out by using available data on phase equilibrium in MORB and pyrolite and thermoelasticity of related minerals. Here, we chose MORB and pyrolite as the representative compositions for the oceanic crust and ambient mantle, respectively. At first, we compiled reported phase equilibrium data at high-pressure and high-temperature on MORB and pyrolite, and constructed their *P*-*T* phase diagram. Secondary, we calculated density and elastic moduli of individual minerals at high-*P* and high-*T* using same scheme as that used in our previous study (Nishihara and Takahashi, 2001) and thermoelastic parameters for related minerals. For stishovite, which undergoes second-order transformation caused by elastic instability, its shear modulus was determined by different manner.

The density and seismic velocities for bulk MORB and pyrolite were calculated from the density and elastic moduli of individual minerals and mineral proportions based on the previous phase equilibrium experiments. These calculations were carried out at the *P*-*T* conditions of along normal, +300 and –300ºC geotherms to 800 km depth condition and to 2900 km depth condition along the normal geotherm. By using the present results, behavior of the oceanic crust entrained within mantle plume are considered, and seismic scatterers in the mid lower mantle are examined whether they are plausible as the oceanic crust.

4-2 Phase equilibria in MORB and pyrolite

Phase relations in MORB

We constructed pressure (*P*)- temperature (*T*) phase diagrams for MORB and pyrolite compositions and determined weight fractions of constituting minerals in these compositions by compilation of reported data of high-*P* and high-*T* phase equilibrium experiments. The geotherm estimated by Brown and Shankland (1981) was adopted for the normal geotherm in this study. This geotherm is close to those for the transition zone estimated by Akaogi et al. (1989) and Ito and Katsura (1989). The 300ºC higher and 300ºC lower profiles than the normal geotherm (HT and LT geotherms, respectively) were also used, HT geotherm may represent conditions of hot plume (e.g. White and McKenzie, 1989). The following thermoelastic calculations were conducted along the geotherms. These geotherms are depicted in the *P*-*T* phase diagrams (Fig. 4-1).

The constructed phase diagrams for MORB composition are shown as Figs. 4-1a and 4-2. Phase boundary of coesite (Coe)-stishovite (St) is based on in situ observation of SiO_2 at high-*P* and high-*T* (Zhang et al., 1996). Weight fractions of minerals up to 14 GPa are based on recent study on MORB by Aoki and Takahashi (2002). Aoki and Takahashi (2002) revised phase relation of MORB at temperatures between 1200 and 1700ºC, which has been studied previously by Irifune et al. (1986) only at 1200ºC. Aoki and Takahashi observed SiO_2 phase (Coe or St) below 12 GPa, while Irifune et al. reported only St above 12 GPa as the SiO_2 phase. The Cpx/Grt ratio at 1200ºC in Aoki and Takahashi is much smaller than the data reported by Irifune et al. (1986) (<~16 GPa). We believe the results by Aoki and Takahashi (2002) are more reliable than those by Irifune et al. (1986) because of their longer run durations. This smaller Cpx/Grt ratio leads higher density of MORB at the Cpx stable conditions. Aoki and Takahashi (2002) also reported that the Cpx/Grt ratio increases with increasing temperature. This is also incorporated in

present phase diagrams of MORB. Because, experiments of Aoki and Takahashi (2002) is limited up to 14 GPa, Cpx-out phase boundary above 14 GPa is taken from Irifune et al. (1986) and Yasuda et al. (1994). The weight fractions of Coe and St are assumed to be constant up to the pressure of appearance of hexagonal aluminous phase (HAP, same as NAL phase reported by Miyajima et al., 2001; Hirose and Fei, 2002) and at all temperature conditions.

Phase boundary of Ca-rich silicate perovskite (CaPv)-in is based on Irifune and Ringwood (1987) and Hirose and Fei (2002), those of HAP-in, Mg-rich silicate perovskite (MgPv)-in, Ca ferrite-type aluminous phase (CF)-in, and Grt-out are based on Hirose and Fei (2002). Because the number of high-*P* experiments on these phase transition is still limited, accuracy of determination of these phase boundary may be somewhat lower than that of phase boundaries at lower pressures. Mineral weight fractions in MORB after completion of the phase transitions are 22% St, 23% CaPv, 5% HAP, 34% MgPv and 16% CF (Ono et al., 2001; Hirose and Fei, 2002), and are assumed to be constant to pressure and temperature.

Hirose and Fei (2002) reported the appearance of HAP at 25–27 GPa and below 2100ºC in MORB. Irifune and Ringwood (1993) found CF in MORB composition above 25 GPa and at 1500ºC. Currently, the CF reported by Irifune and Ringwood (1993) is considered to be misidentification of HAP (Akaogi et al., 1999; Miyajima et al., 2001). On the other hand, Kesson et al. (1994) and Ono et al. (2001) conducted high-*P* experiments on MORB to 37 GPa and to 100 GPa, respectively, and they did not observed HAP in their experimental products. HAP is considered to be the host phase of K_2O, and the higher K_2O content should stabilize this phase. The reason of absence of HAP in Kesson et al.'s (1994) run products may be the use of synthetic starting material with no K_2O. The starting material used by Ono et al. (2001) contains 0.2 wt% K_2O. However, no K_2O is contained in reported chemical composition of individual minerals. This strongly suggests the existence of minor amount of HAP phase as described in the paper. Thus, we assumed the HAP exists in natural K-bearing MORB throughout the Earth's lower

mantle.

Kesson et al. (1994) reported no phase change to 100 GPa in MORB composition. However, recently it is revealed that St undergoes second-order transition from rutile-type to $CaCl_2$-type at ~50–80 GPa (e.g. Cohen, 1992; Andrault et al., 1998; Ono et al., 2002a). This phase transition is completely reversible and cannot be detected from observation of quenched run products such as Kesson et al. (1994). We adopted this phase boundary determined by Ono et al. (2002a) in the following calculation. It is not established whether SiO_2 transforms to further dense phase (α-PbO_2-type, pyrite-type) at the lower mantle condition (e.g. Karki et al., 1997a; Dubrovinsky et al., 2001). We did not consider these phases.

Phase relations in pyrolite

The constructed phase diagrams for pyrolite composition are shown as Figs. 4-1b and 4-3. These phase diagrams are based on phase equilibrium experiments on pyrolite and pyrolite-like natural peridotites. The phase relations between olivine (Ol), wadsleyite (Wd) and ringwoodite (Rw) are based on the phase diagram in the system Mg_2SiO_4-Fe_2SiO_4 determined by Akaogi et al. (1989). Irifune and Isshiki (1998) clarified that, in pyrolite composition, pressure interval of Ol + Wd region becomes significantly narrower than that for olivine with fixed $(Mg,Fe)_2SiO_4$ composition because of the Mg-Fe partitioning between coexisting minerals (Grt, Cpx). We adjusted the Wd-in and Ol-out phase boundary to be consistent with the result of Irifune and Isshiki with fixed Clapeyron slope (dP/dT) of Akaogi et al. (1989). The same effect is expected for Wd-Rw transition, but it has not been determined yet. It was not taken in our phase diagram (Figs. 4-1b, 4-3). Weight fractions of Ol, Wd and Rw are fixed to be 61% (e.g. Irifune and Isshiki, 1998; Hirose, 2002), and assumed to be independent to temperature.

Orthopyroxene (Opx)-out is based on Takahashi (1986) and Irifune and Isshiki (1998), and its dP/dT is negative. This negative Clapeyron slope can be understood from the temperature

dependence of pyroxene (Px)-Grt transition in the system $Mg_4Si_4O_{12}$-$Mg_3Al_2Si_3O_{12}$ (Akaogi et al., 1987). Cpx-out is based on Zhang and Herzberg (1994) and Irifune and Isshiki (1998), CaPv-in is based on Irifune and Ringwood (1987) and Zhang and Herzberg (1994). These phase boundaries are nearly independent of temperature. Weight fractions of Grt, Opx and Cpx along normal geotherm are based on Irifune and Isshiki (1998). Mineral weight fractions along HT and LT geotherms were derived by modification of those along normal geotherm to be consistent with phase boundaries.

All the phase boundaries and weight fractions above 21 GPa in pyrolite (Figs. 4-1b, 4-3) are derived from recent detail experiments on KLB-1 peridotite by Hirose (2002). The appearance of akimotoite (Ak; Mg-rich silicate ilmenite) in pyrolitic composition at 22 GPa and 1600ºC is reported by Hirose (2002), while Ak was not found by other experimental studies on similar compositions at similar *P*-*T* conditions (Irifune, 1994; Wood, 2000). However, the appearance of Ak in pyrolite at ~22 GPa and relatively low temperatures (below 1600ºC) has been predicted based on the phase diagram in the system $Mg_4Si_4O_{12}$-$Mg_3Al_2Si_3O_{12}$ (e.g. Weidner and Wang, 1998; Akaogi et al., 2002). Since there is no reliable experimental data on pyrolite at lower than 1600ºC and >20 GPa, we extended Ak-in line linearly to lower temperatures in *P*-*T* space based on Hirose's (2002) data (Fig. 4-1b). Because Ak can contain only small amount of FeO and CaO (Ito and Yamada, 1982; Hirose, 2002), Grt would not transform to Ak completely. Then, weight fraction of Ak in pyrolite was suppressed to 8% even in the case of LT geotherm (Fig. 4-3).

At 22–25 GPa, there are many phase boundaries in pyrolite, and some of these have positive d*P*/d*T* while others have negative d*P*/d*T*. Then, quite complex phase relations are caused in these conditions. At high-temperatures (>~1900ºC) MgPv is primarily formed by the transition of Grt. The contribution of transition of Grt for MgPv formation decreases with decreasing temperature, and that of decomposition of Rw increases with decreasing temperature. At

low-temperatures (<~1600ºC), small amount of Ak also transforms to MgPv. More detail of these phase transitions is described in Hirose (2002). After completion of above phase transitions, pyrolite composed of 78% MgPv, 15% Mw (magnesiowüstite) and 7% CaPv in weight.

Chemical compositions of minerals

We used chemical compositions of individual mineral to investigate compositional dependence of zero-pressure density and thermoelastic parameters. Chemical compositions are also based on the results of high-*P* and high-*T* experiments on MORB and pyrolite mentioned above. It should be noted that the compositions of mineral are determined independently of mineral proportions (weight fractions), and bulk composition is not preserved at various *P*-*T* conditions in a strict sense. However, in order to preserve the bulk composition in such calculation, the partition coefficients of all major elements between all coexisting minerals and their pressure and temperature dependence is needed. Lack of these data necessitates us to adopt present method.

Chemical compositions for Coe and St are assumed to be pure SiO_2, and that for CaPv is assumed to be $CaSiO_3$. Compositions for HAP and CF are assumed to be same as those of Ono et al. (2002c, b), respectively. Used chemical compositions of other minerals are shown in Table 4-1 and Fig. 4-4. For Ol, Wd, Rw, Opx, Ak, MgPv and Mw, only the X_{Fe} value (Fe/(Mg + Fe) in molar ratio) is considered (Table 4-1). For Cpx, X_{Fe} and X_{Jd} (Jd/(Di + Hd + Jd) in molar ratio, where Jd; jadeite, Di, diopside, Hd; hedenbergite) (Table 4-1). These compositions are assumed to be constant regardless of pressure and temperature.

It is well known that chemical composition of Grt crystallized from fixed bulk composition changes significantly with changing pressure. Fig. 4-4 shows variations of chemical compositions (X_{Fe}, X_{Ca}, X_{Mj}) of Grt (a) in MORB and (b) in pyrolite, where X_{Ca} = Ca/(Mg + Fe + Ca) in molar ratio and X_{Mj} is majorite content. X_{Mj} was calculated by following two schemes, one is $X_{MjA} = 1 -$

(Al + Cr)/2, another is X_{MjS} = 8Si/SUM – 3, where O = 12 and SUM is sum of cation. Both X_{MjA} (opencircles) and X_{MjS} (open triangles) are plotted in Fig. 4-4, and these values are virtually the same. Data for Grt in MORB are collected from experiments at 1200–1750ºC (Irifune et al., 1986; Irifune and Ringwood, 1993; Ono and Yasuda, 1996; Ono et al., 2001; Aoki and Takahashi, 2002), those for Grt in pyrolite are from experiments at 1100–1600ºC (Irifune, 1987, 1994; Irifune and Ringwood, 1987; Irifune and Isshiki, 1998; Hirose, 2002).

Grt in MORB and pyrolite have quite different compositions. The X_{Fe} values of Grt in MORB are 0.3–0.4, while those of Grt in pyrolite are 0.05–0.2, and they decrease with increasing pressure. The X_{Ca} values of Grt in MORB are systematiclly higher than those of Grt in pyrolite, and the X_{Mj} values of Grt in MORB are systematically lower than those of Grt in pyrolite. However, we can find that the behavior of these values (X_{Ca}, X_{Mj}) against pressure is similar for Grt in both MORB and pyrolite, although large scatter exists in reported data. The X_{Ca} and X_{Mj} values increase in the pressure range of 5 GPa to ~15 GPa, and decreases above ~20 GPa. At the pressure range of ~15–20 GPa, the X_{Ca} and X_{Mj} values are almost constant. These changes in X_{Ca} and X_{Mj} values are attributable to gradual Grt-pyroxene (Cpx, Opx) phase transition and Grt-CaPv transition (see Cpx-out and CaPv-in in Fig. 4-4). We adopted the compositional changes of Grt shown as bold lines in Fig. 4-4 along the normal geotherm. The compositions of Grt along HT and LT geotherms are derived by slight modification of Fig. 4-4 to be consistent with Cpx-out and CaPv-in phase boundary along each geotherm (Fig. 4-1).

4-3 Thermoelastic calculations

Expressions for density and seismic velocities of minerals

In order to obtain density and seismic velocities of MORB and pyrolite in the Earth's mantle conditions. We used the same formulation as Vacher et al. (1996). The same method was also used in Vacher et al. (1998) and Nishihara and Takahashi (2001). As described above,

stishovite transforms from rutile-type to $CaCl_2$-type at the mid-lower mantle *P*-*T* conditions (e.g. Andrault et al., 1998; Ono et al., 2002a). Because this phase transformation is caused by elastic instability, elasticity of stishovite shows anomalous behavior at the pressure conditions around this transformation (e.g. Cohen, 1992; Karki et al., 1997b; Carpenter et al., 2000). Thus, shear modulus of stishovite was calculated by different manner, and this is described in another section.

Because following calculations were made by using adiabatic bulk modulus (K_S) (not isothermal bulk modulus, K_T), the excess temperature (ΔT) occurs by adiabatic compression. Then, at first, the excess temperature was estimated and its effect was corrected. The expression of ΔT using temperature after adiabatic compression (T) is given by

$$\Delta T = T\left[1-\exp\left(\gamma_{\mathrm{G}}\int_0^P \frac{\mathrm{d}P}{K_S}\right)\right]$$

where γ_{G} denotes Grüneisen parameter.

Secondary, density and bulk and shear moduli of mineral at zero-pressure and high-temperature were calculated. The density of mineral $\rho(T)$ as a function of temperature T is expressed by

$$\rho(T)=\rho(T_0)\exp\left[-\int_{T_0}^{T}\alpha(T')\mathrm{d}T'\right]$$

where $\rho(T_0)$, T_0 and α are density at ambient condition, reference temperature and the thermal expansion coefficient, respectively. Using Anderson's (1988) dimensionless logarithmic anharmonic notation (DLA), the temperature dependence of an elastic modulus M (either adiabatic bulk modulus K_S or shear modulus G) of a mineral is

$$M(T)=M_0\left[\frac{\rho(T)}{\rho(T_0)}\right]^{\{M\}_P}$$

where

$$\{M\}_P = \left(\frac{\partial \ln M}{\partial \ln \rho}\right)_P = -\frac{1}{\alpha M}\left(\frac{\partial M}{\partial T}\right)_P$$

is assumed to be independent of temperature (Anderson, 1988). According to Duffy and Anderson (1989), value of Anderson-Grüneisen parameter $\{M\}_P$ is generally constant above ~500 K, then $\{M\}_P$ value at 600 K was calculated and used here. Adiabatic pressure derivatives of the elastic moduli $M'(T)$ are given by

$$M'(T) = M'_0\left[\frac{\rho(T)}{\rho(T_0)}\right]^{-1}.$$

In the third step, pressure effects for the density and elastic moduli were calculated at zero-pressure and high-temperature. This is done by the third-order Birch-Murnaghan equation of state (third-order Eulerian finite strain). It is expressed by

$$P = 3K_{S0}(1+2f)^{\frac{5}{2}}\left\{1+\frac{3}{2}(K'_S-4)f\right\},$$

$$K_S = K_{S0}(1+2f)^{\frac{5}{2}}\{1+(3K'_S-5)f\},$$

$$G = G_0(1+2f)^{\frac{5}{2}}\left\{1+\left(5-\frac{3K_{S0}G'}{G_0}\right)f\right\},$$

where

$$f = \frac{1}{2}\left\{\left(\frac{\rho}{\rho_0}\right)^{\frac{2}{3}}-1\right\}.$$

K_{S0}, K'_S, G_0, G' and ρ_0 are the values at zero-pressure and high-temperature. K_S, G and ρ are the values at high-pressure and high-temperature.

Elasticity data set

Thermoelastic calculation was conducted by using previously reported values of

thermoelasticity for related minerals. The thermoelastic parameters used in present calculation are listed in Table 4-2.

Bulk modulus (K_{S0}), its pressure derivative (K'_S), its temperature derivative ($(\partial K_S/\partial T)_P$) and thermal expansivity for Cpx in MORB are collected from Chapter 1 (Nishihara et al., 2003a). These parameters for Rw are collected from Chapter 2 (Nishihara et al., 2002b). Those parameters determined in Chapter 3 for MORB majorite are used for Grt in MORB garnetite (garnetite means the rock consists of Grt with small amount of St, see Fig. 4-2). Bulk moduli and their derivatives determined in previous chapters are isothermal values (K_{T0}, K'_T and $(\partial K_T/\partial T)_P$). However, as propagation of seismic wave is considered to be adiabatic process, we use adiabatic bulk moduli and their derivatives in the following calculations. The parameters derived in previous chapters are converted to adiabatic values by using thermodynamic identity $K_{S0} = K_{T0}(1 + \alpha\gamma_G T)$ for K_{S0} and $(\partial K_S/\partial T)_P$, and K'_S was derived from $K'_S \approx K'_T(1 + \alpha\gamma_G T)$.

Most of the other thermoelastic parameters are collected from the data set compiled by Vacher et al. (1998) (Table 4-2). This data set consists of the data properly selected from the literatures available in that time. After their compilation, EOS measurements with synchrotron-based X-ray diffraction and sound velocity measurements at high-pressure and high-temperature have largely increased both the number and accuracy of data relevant to mantle minerals. However, the most of recent results are generally consistent with previous studies, and no significant correction is required for the data set of Vacher et al. (1998). We describe some important aspects on the validity of thermoelastic parameters used in this study (Table 4-2).

The technique of P-V-V_P-V_S-T (P-V^3-T) measurements up to 8 GPa and above 1000°C using the ultrasonic measurements and synchrotron radiation is developed by Liebermann's research group (e.g. Li et al., 1998; 2001, Chen et al., 1998; Liebermann, 2000). This new technique makes it possible to measure the elasticity of minerals directly at the P-T conditions relevant to the Earth's mantle. However, significant inconsistencies in the high-temperature

elasticity are reported between this new technique and other techniques, for Wd (Li et al., 1998; 2001 (P-V^3-T) and Katsura et al., 2001, respectively), for MgO (Chen et al., 1998 (P-V^3-T) and Isaak, 1993, Matsui et al., 2000, respectively). The reason for this discrepancy is not clear, but the expected large temperature gradient in P-V^3-T measurements may be responsible. The temperature derivatives of elastic moduli ($(\partial K_S/\partial T)_P$, $(\partial G/\partial T)_P$) used in our calculations (from Vacher et al., 1998) are inconsistent with the results by P-V^3-T measurements, but generally consistent with other measurements (P-V-T measurement, zero-pressure elasticity measurement and molecular dynamic simulation).

For Opx, we used K_{S0} = 124 GPa and K'_S = 5.6 (Angel and Hugh-Jones, 1994; Hugh-Jones and Angel, 1994) following the compilation by Vacher et al. (1998). Angel and Hugh-Jones (1994) and Hugh-Jones and Angel (1994) proposed a change in the mechanism of compression at ~4 GPa based on their compression experiments to 8.5 GPa, and they concluded that the compression curve of $MgSiO_3$ orthoenstatite should be described by two independent EOSs with significant different values of K_{S0} and K'_S for below and above 4 GPa. The values used in this study are their recommended values at P = 4–8.5 GPa. However, recently, Angel and Jackson (2002) concluded that the compression of orthoenstatite can be expressed by single EOS with K_{T0} = 105.8 GPa and K'_T = 8.5, based on the analyses using not only the compression data but also the sound velocity data (Weidner et al., 1978; Flesch et al., 1998; Jackson et al., 1999). The difference would not affect the resultant density and seismic velocity profiles of pyrolite, because the amount of Opx in pyrolite is low (<13 wt%) and no significant pressure extrapolation is required for calculation (P = 5–11 GPa).

We used K'_S = 5.1–5.3 for Grt following Vacher et al. (1998) (except for MORB majorite). This value is based on ultrasonic velocity measurements only up to P = 3 GPa (Rigden et al., 1994). As discussed in Chapter 3, recent studies based on laser induced phonon spectroscopy (Brillouin scattering and impulsively stimulated scattering: Chai et al., 1997; Conrad et al., 1999;

Sinogeikin and Bass, 2000; 2002) on Grt at high-pressures (up to P = 10–20 GPa) generally result in K'_S = ~4, whereas recent studies with ultrasonic interferometry up to P = ~10 GPa yield much higher values K'_S = ~5–6.5 (e.g. Gwanmesia et al., 1998; Chen et al., 1999; Liu et al., 2000). The reason of this discrepancy is still unresolved clearly, this may caused by the non-hydrostatic condition and/or the porosity and grain-boundary scattering in the ultrasonic experiments.

Recent compression experiments (Zhang and Weidner. 1999; Kubo et al., 2000; Daniel et al., 2001) indicate that $MgSiO_3$ perovskite with small amount of Al_2O_3 has significantly lower bulk modulus than pure $MgSiO_3$ perovskite (e.g. ~10% lower bulk modulus for perovskite with 5 mol% Al_2O_3, Zhang and Weidner, 1999). On the contrary, Andrault et al. (2001) reported the higher bulk moduli for Al-bearing $MgSiO_3$ perovskite than that of $MgSiO_3$. The reason of this inconsistency is unclear, but it may be explained by a change in the substitution mechanism of Al in $MgSiO_3$ versus pressure, temperature and bulk composition (Brodholt, 2000; Andrault et al., 2001; Kojitani and Miyajima, 2002). Because the K_{S0} for MgPv used in our calculation is the value based on the experiments of MgPv with no-Al following Vacher et al. (1998) (Mao et al., 1991; Yeganeh-Haeri, 1994; Funamori et al., 1996), this K_{S0} values possibly too large for Al-bearing MgPv in MORB and pyrolite. Moreover, recent first principles calculation indicated that G_0 of $MgSiO_3$ is lowered by 6% substitution of 25 mol% $FeSiO_3$ (Kiefer et al., 2002).

We used G_0 = 127 GPa for Mw in pyrolite, which was obtained by conversion of the results of the ultrasonic measurements to 3 GPa (Jackson and Niesler, 1982; Duffy and Ahrens, 1995) from the forth-order finite-strain expressions of K_S at high-pressure to third-order expression with compositional correction (Vacher et al., 1998). Recent ultrasonic measurements revealed that G_0 is ~112 GPa for Mw with X_{Fe} = ~0.15, which relevant composition to Mw in pyrolite. (Jacobsen et al., 2002; Kung et al., 2002).

Because CaPv ($CaSiO_3$ perovskite) transforms to amorphous state at ambient condition, the sound velocity measurements on CaPv is technically difficult and no experimental data on shear

modulus (G_0) and its derivatives (G', $(\partial G/\partial T)_P$) have been reported yet. We used G_0 = 150 GPa, which derived by lattice dynamic calculation by Wolf and Jeanloz (1985) following the compilation by Vacher et al. (1998). Wolf and Jeanloz's (1985) calculation yields relatively large bulk modulus 274 GPa compared to the reliable results by the compression experiments ~230 GPa (Wang et al., 1996; Shim et al., 2000). On the other hand, recent first-principles calculations by Karki et al. (1998) results in K_{S0} = 236 GPa, which is nicely consistent with the experiments, and G_0 = 165 GPa. Sinelnikov et al. (1998) estimated G_0 of $CaSiO_3$ perovskite by the extrapolation from G_0 of $Ca(Ti,Si)O_3$ solid solutions. Their estimation results in G_0 = 112 GPa for $CaSiO_3$ perovskite, and this value is significantly lower than those obtained by theoretical calculations (Wolf and Jeanloz, 1985; Karki et al., 1998). Shear modulus (G_0) of CaPv is not constrained accurately and its derivatives (G', $(\partial G/\partial T)_P$) are much highly uncertain.

Thermoelastic data for Coe, St, HAP and CF are not presented in the compilation by Vacher et al. (1998), and collected from other literatures. For Coe, thermoelastic parameters are mainly collected from Levien and Prewitt (1981), Weidner and Carleton (1977) and Skinner (1962). There are no available data for derivatives of shear modulus of Coe. These parameters are assumed to be similar to those of other upper mantle minerals (e.g. Ol, Opx), and may possess considerable uncertainties. These uncertainties of thermoelastic parameters of Coe would not affect the resultant density and seismic velocity profiles, because of its low proportion in MORB (<6wt%).

For K_{S0}, K'_S, $(\partial K_S/\partial T)_P$ and α of St, the data determined by *P-V-T* experiments up to 23 GPa and 800°C by Nakayama et al. (2003) are used. Nakayama et al.'s (2003) results, based on the data collected at wide range of *P-T* conditions, are generally consistent with most of previous reliable studies on thermoelasticity of St (e.g. Weidner et al., 1982; Li et al., 1996; Liu et al., 1999), and it enables the robust estimation of the elasticity of St at the conditions of Earth's mantle. Data for G_0 and G' of St are from the ultrasonic velocity measurements to 3 GPa by Li et

al. (1996), and data for $(\partial G/\partial T)_P$ is from the elasticity systematics by Duffy and Anderson (1989).

For thermoelasticity of HAP and CF, there are few available data. Recently, Ono et al. (2002b, c) studied compressibility of HAP and CF in basaltic composition. The data for K_{S0} and K'_S of HAP and CF are converted from isothermal values reported by these studies. Other parameters for HAP and CF are assumed to be similar to those of other mantle minerals with similar bulk modulus (e.g. Rw, MgPv, Ak), and may possess considerable uncertainties.

Because the Grüneisen parameter γ_G is used only to correct the temperature increase concerned to adiabatic compression, this parameter have very little effect on the calculated density and seismic velocity profiles. We don't discuss validity of this parameter.

By the thermoelastic calculation using the parameters in Table 4-2, ρ, K_S and G for the individual minerals are derived. Derived values in MORB and pyrolite along the normal geotherm were depicted in Figs. 4-5, 4-6, 4-7 and 4-8.

Shear modulus of stishovite

Recent theoretical and experimental studies revealed that St undergoes second-order phase transition at ~50 GPa and room temperature from rutile-type (tetragonal) to $CaCl_2$-type (orthorhombic) caused by pressure-induced elastic instability (e.g. Cohen, 1992; Kingma et al., 1995; Karki et al., 1997a; Andrault et al., 1998; Ono et al., 2002a). This transition produce markedly nonlinear variations of the elastic constants around the transition pressure (e.g. Cohen, 1992; Karki et al., 1997b; Carpenter et al., 2000). Because MORB contains ~20% of St in lower mantle conditions (>27 GPa) (Fig. 4-2), this anomalous variations of elastic constants of St should affect significantly to the seismic velocities for bulk MORB. Therefore, we took in the effect of the transition for the shear modulus (G) of St by modifying Landau free energy expansion by Carpenter et al. (2000). Bulk modulus (K_S) of St does not change by the transition, and was calculated by the same manner as for other minerals.

Carpenter et al. (2002) evaluated the variations of elastic constants of SiO_2 around the rutile-type to $CaCl_2$-type transition at room temperature by using Landau free energy expansion. In that study, previously reported single crystal elasticity at ambient condition (Weidner et al., 1982), the results of first-principles calculation of elastic constants at high-pressures (Karki et al., 1997b) and soft optic mode data at high-pressures (Kingma et al., 1995) are used to constrain the parameters for Landau free energy expansion. The results of Carpenter et al. are shown as broken line in Fig. 4-9. However, since Carpenter et al. (2000) investigated the elasticity of St only at room temperature, their results cannot be applied directly to calculation of seismic velocities of MORB along the geotherms.

The rutile-$CaCl_2$ phase boundary at 300 K in SiO_2 is well constrained by experimental and theoretical studies to be ~50 GPa (Kingma et al., 1995; Karki et al., 1997a; Andrault et al., 1998). However, the high-pressure X-ray diffraction (XRD) by Ono et al. (2002a) is the only report on the transition at high-temperature. According to that study, the boundary is highly dependent on temperature and is placed at ~80 GPa at 2000°C. However, the slight distortion from tetragonal (rutile-type) to orthorhombic ($CaCl_2$-type) is quite difficult to be detected by XRD (Andrault et al., 1998; Ono et al., 2002a). The Clapeyron slope (dP/dT) of the phase boundary determined by Ono et al. is 0.012 GPa K^{-1}, whereas non-empirical lattice dynamical model by Kingma et al. (1995) predicts dP/dT = 0.004 GPa K^{-1}. We tentatively follow the phase boundary by Ono et al. (2002a), but it could be overestimated due to the experimental difficulty to detect the transition.

In order to apply the results of Carpenter et al. (2000) to high-temperatures (along geotherms), we consider the shift of transition pressure as well as the temperature dependence of elastic constants by the following way.

At first step, we modified the transition pressure (P^*_C) from the value at room temperature (P^*_C = 49 GPa in Carpenter et al., 2000) to the value along the geotherm (e.g. P^*_C = 77.5 GPa for the normal geotherm). In this extrapolation, four parameters P^*_C, P_C, C^O_{11} and C^O_{12} in Landau

expansion are varied, where P_C is critical pressure and C^O_{ij} are bare (i.e. excluding the influence of the phase transition) elastic constants. By changing the four parameters, the transition pressure was adjusted to the objective pressure with fixed zero-pressure values of elastic constants. An example of calculated variations of single-crystal elastic constants of St (P^*_C = 77.5 GPa) are shown as bold solid lines in Fig. 4-9.

From the results, the upper and lower bounds of aggregate shear modulus (G) was calculated by Voigt and Reuss bounds, respectively. The arithmetic average of the two bounds is also calculated (Voigt-Reuss-Hill average; VRH). The variations of VRH for St as a function of pressure are depicted in Fig. 4-10a (bold broken line). For comparison, the G calculated by third-order Birch Murnaghan equation of state (BM3) with the parameters in Table 4-2 is also shown in the figure (open circles). It is clearly recognized that G of St decreases extremely around the phase transition, and the G value drops to half of that by BM3 just at the transition (P = 77.5 GPa).

In the second step, temperature effects for shear modulus G were incorporated by using the ratio of G at room temperature and that along geotherm calculated by BM3. The variations of G at room temperature and along the normal geotherm calculated by BM3 with parameters in Table 4-2 are shown in Fig. 4-10 (open and solid circles, respectively). We assumed that the ratio of these values is directly applicable to G derived by Landau theory. The obtained VRH of G is also shown in Fig. 4-10a and 4-10b (bold solid lines), and those for Voigt and Reuss bounds are shown in Fig. 4-10b (bold dotted dashed lines). It is clearly seen that G of Reuss bound, assuming uniform stress throughout the aggregate, vanishes just at the transition pressure (Fig. 4-10b). We used these values for G of St to obtain seismic velocities of MORB along the geotherms in subsequent calculations. Derived ρ, K_S and G for St along the normal geotherm were depicted in Figs. 4-5 and 4-7.

Density and seismic velocities of bulk rock

The Hill average of Voigt and Reuss bounds (Watt et al., 1976) were used for calculating the elastic moduli (K_S, G) of the composite phase assemblage

$$M_{\mathrm{V}} = \sum_i v_i M_i \ ,$$

$$M_{\mathrm{R}} = \frac{1}{\sum_i \frac{v_i}{M_i}},$$

$$M_{\mathrm{VRH}} = \frac{\left(M_{\mathrm{V}} + M_{\mathrm{R}}\right)}{2},$$

where M represents adiabatic bulk modulus (K_S) and shear modulus (G), v_i is volume proportion of i-th phase, and subscripts V, R and VRH denote the Voigt and Reuss bounds and Hill average, respectively. Bulk sound velocity (V_Φ), P-wave velocity (V_P) and S-wave velocity (V_S) are expressed by

$$V_\Phi = \sqrt{\frac{K_S}{\rho}} \ ,$$

$$V_\mathrm{P} = \sqrt{\frac{K_S + \frac{4}{3}G}{\rho}} \ ,$$

$$V_\mathrm{S} = \sqrt{\frac{G}{\rho}} \ .$$

4-4 Results

Fig. 4-11 shows variations of calculated density (ρ) and seismic velocities (V_Φ, V_P, V_S) for MORB and pyrolite along the three geotherms to 800 km depth, respectively. Fig. 4-12 shows those along only normal geotherm up to 2900 km depth (core-mantle boundary). The density differences relative to pyrolite along the normal geotherm are shown in Fig. 4-13. Two globally

averaged seismic models for Earth's interior (PREM; Dziewonski and Anderson, 1981, ak135; Kennett et al., 1995) are also shown in Figs. 4-11 and 4-12. The depth in the Earth's interior corresponding to each pressure was calculated by using the data in PREM. Bulk sound velocity V_Φ was calculated by

$$V_\Phi = \sqrt{\frac{K_S}{\rho}} = \sqrt{V_P{}^2 - \frac{4}{3}V_S{}^2} .$$

Density and seismic velocities to 800 km depth

At first, we see the results of calculation along the normal geotherm to 800 km depth, which corresponds to ~30 GPa (Fig. 4-11).

In order to assess the uncertainties of calculated profiles, test calculations were made for some depth conditions (with 100 km intervals) by varying each thermoelastic parameter within the estimated uncertainties (Vacher et al., 1998; references in Table 4-2), and the largest uncertainty value was adopted to be representative error for each mineral. The errors of coexisting minerals were combined for each depth condition and these for the properties along the normal geotherm are indicated in Fig. 4-14 (error bars for MORB and pyrolite). The uncertainties of estimated (non-experimental) values and values without nominal error were overestimated intentionally. The errors for density (ρ) are so small and similar to the width of lines in some cases. The errors for seismic velocities, especially for V_S, are large. The relatively large errors in V_P and V_S are due to the large uncertainties in the derivatives of shear modulus for concerned minerals. The size of the errors for the profiles along HT and LT geotherms are considered to be similar to those along normal geotherm.

The density of pyrolite along geotherm shows good agreement with those based on seismic observations (PREM, ak135). However, the V_P and V_S of pyrolite in the transition zone (410–660 km), and the V_Φ, V_P and V_S in the upper most part of lower mantle (660–800 km) deviate

significantly from the seismic observations and show relatively larger values. Moreover, the gradients of V_P and V_S of pyrolite versus depth are relatively gentle compared to the observations. These deviations in the transition zone from the seismic observations may be resolved by adopting olivine-poor composition of the mantle (e.g. piclogite, Duffy and Anderson, 1989; komatiite, Nishihara and Takahashi, 2001). The piclogite is the compositional model for the mantle containing lesser amount of Ol than that of pyrolite; typical Ol content in piclogite is 20–50% (e.g. Bass and Anderson, 1984; Duffy and Anderson, 1989; Ita and Stixrude, 1992) while that for pyrolite is ~60% (e.g. Ringwood, 1962).

The density of MORB along the normal geotherm is larger than those of pyrolite and the seismic observations throughout the upper mantle (<660 km) (Fig. 4-11 and 4-13). Pyrolite becomes denser than MORB at 660 km depth because of the transformation to perovskite lithology (see Fig. 4-3), but once MORB transforms to lower mantle assemblage at 730 km depth (see Fig. 4-2), it is denser than pyrolite again. These relations are generally consistent with previous studies (e.g. Irifune et al., 1986; Irifune and Ringwood, 1993; Hirose et al., 1999). Irifune et al. (1986) did not observed Coe, and their density profile of MORB do not have density gap corresponds to the Coe-St phase transition. On the other hand, the Coe-St transition is incorporated in this study based on Aoki and Takahashi (2002), and it is apparent from the density profile for MORB around 300 km depth (see Figs. 4-11 and 4-13). Although weight fractions of Coe and St in MORB are as few as 6%, the jumps for density and seismic velocities of MORB caused by the Coe-St transition are large because the very large difference between their physical properties (ρ, K_S, G, see Fig. 4-5).

The V_P of MORB is slightly larger than that of pyrolite at <410 km depth, and slightly smaller at 410–660 km. At 660km depth, the difference of V_P become larger caused by the transition to perovskite lithology in pyrolite, but once MORB transforms to lower mantle assemblage at 730 km depth, the V_P values of MORB and pyrolite become very close (Fig. 4-11).

The behavior of V_Φ for MORB is quite similar to that of V_P (Fig. 4-11). The V_S of MORB is larger than that of pyrolite at <410 km depth, and have similar value in the transition zone (410–660 km depth). As similar to ρ, V_P and V_Φ, the difference of V_S between MORB and pyrolite becomes large at 660–730 km. After the transitions in MORB at 730 km, the V_S of MORB is slightly larger than pyrolite (Fig. 4-11).

At <~450 km, temperature effects for the density and seismic velocities of MORB are relatively large, as recognized from relatively wide intervals of lines between the properties along the normal, HT and LT geotherms shown in Fig. 4-11. This is due to the temperature dependence of Cpx/Grt ratio in MORB (Aoki and Takahashi, 2002). According to Aoki and Takahashi (2002), Cpx increases with increasing temperature in MORB composition. Then, increase of temperature decreases the density and seismic velocities for bulk MORB not only by normal thermal effects (thermal expansion, temperature effect on elastic moduli) but also by the change of mineral proportions.

Density and seismic velocities in the lower mantle

Next, we see the density and seismic velocities of MORB and pyrolite in the lower mantle conditions (up to 2900 km). It should be noted that we used some assumed parameters for HAP and CF, and recently reported compositional dependencies for elastic moduli of some lower mantle minerals (MgPv, Mw, CaPv) are not included in this study. Then, the calculated profiles for MORB and pyrolite in the lower mantle may possess considerable uncertainties.

The density of pyrolite in the lower mantle (660–2900 km depth) shows excellent agreement with seismic models (Fig. 4-12). However, the seismic velocities (V_Φ, V_P, V_S) of that are systematically larger than the seismic models. This possibly suggests that the composition of the Earth's lower mantle is not pyrolitic, but the use of new data for elasticity of MgPv, Mw and CaPv may cancel the discrepancy. As described above, according to recent reports, K_{S0} of MgPv,

G_0 of Mw and G_0 of CaPv may be lower than those used in present calculation. The testing calculations for pyrolite by using these new data were carried out: K_{S0} = 232 GPa for MgPv (Zhang and Weidner , 1999), G_0 = 112 GPa for Mw (Jacobsen et al., 2002; Kung et al., 2002), G_0 = 112 GPa for CaPv (Sinelnikov et al., 1998). The results are shown in Fig. 4-15 as blue dashed lines. The resultant profiles for V_Φ, V_P and V_S are nearly consistent with the seismic observations, while the gradients against depth are relatively larger than the seismic models. On the contrary, the density of pyrolite becomes slightly larger, and consistency with the seismic models becomes worse. More accurate determination on the elasticity of these minerals at high-pressure and high-temperature is required to constrain the composition of the Earth's lower mantle.

The density of MORB is larger than that of pyrolite and seismic observations throughout the lower mantle. On the contrary, Ono et al. (2001) estimated that the density of MORB intersects that of the pyrolitic mantle at 1500–2000 km depth based on the phase equilibrium experiments and thermoelastic calculation. Their results, however, may be due to scatters in the experimental data and too much extrapolation in density. In our calcilation, V_Φ of MORB is very close to that of pyrolite and larger than seismic observations (Fig. 4-12).

The V_P and V_S shows anomalous variations in the lower mantle by the effect of the second-order phase transition in SiO_2 caused by elastic instability (Fig. 4-12). The V_P and V_S of MORB calculated with VRH average of St have close values to those of pyrolite at the top and the base of lower mantle. At the mid lower mantle, V_P and V_S of MORB significantly decreases. Especially, the decrease for V_S is drastic, and the decreases just at the transition pressure (77.5 GPa corresponds to 1800 km depth) are very sharp (see Fig. 4-12).

We used three isotropic averaged shear moduli for St (VRH average, Voigt and Reuss bounds) to calculate V_P and V_S of MORB in the lower mantle. Because of its large anisotropy, the VRH average, Voigt and Reuss bounds for St differ significantly (Fig. 4-10; Carpenter et al., 2000). Because of the lack of information on the stress-strain condition of stishovite in MORB

subducted to the lower mantle, it is only possible to say that its elastic properties are within the bound of the two average methods. Similarly, it is also unclear what is plausible method to calculate composite elastic moduli of MORB. Coexistence of elastically different material (very low G_0 of St at around the transition) yields large deviations in the results, when different methods are used to calculate composite elastic moduli. Here, we used VRH average to calculate the composite elastic moduli. If St in MORB exists as isolated mineral grains, bulk elasticity should become close to Voigt bound and have larger values of V_P and V_S. On the contrary, if mineral grains of St interconnect in MORB, bulk elasticity should become close to Reuss bound and have smaller values of V_P and V_S. In the extreme case, V_S for MORB vanishes just at the transition by using the Reuss bound for average shear modulus of St and the Reuss bound to calculate composite shear modulus of MORB.

Because St becomes extremely anisotropic and soft at just around the transition against shear stress (Karki et al., 1997b), it is possible that preferred orientation or layered structure is developed under heterogeneous stress conditions. This may yields large anisotropy in the seismic velocities of MORB.

4-5 Discussion

Behavior of the oceanic crust entrained within mantle plumes

The significance of recycled old oceanic crust in hotspot magma genesis has been pointed out (e.g. Hofmann and White, 1982; Hauri, 1996; Takahashi et al., 1998; Takahashi and Nakajima, 2002). Takahashi and Nakajima (2002) showed that two magma types in Hawaiian volcanoes can be explained by the basalt/peridotite hybrid melting in relatively narrow range of temperature from the melting experiments. Moreover, based on the growth history of some Hawaiian volcanoes, Takahashi and Nakajima (2002) proposed that blocks of former oceanic crust as large as ~1000 km^3 are entrained in the mantle plume. However, it is still not clarified how the oceanic

crust, denser than the ambient mantle, can ascend to Earth's surface.

The density difference between MORB and pyrolite derived from our calculations would present very useful information to investigate the behavior of the oceanic crust in the Earth's mantle. In order to investigate whether the large block of former oceanic crust (~1000 km^3, Takahashi and Nakajima, 2002) can ascend in the mantle plume, we made calculations based on the method similar to Yasuda and Fujii (1998) by using densities of the oceanic crust and the ambient mantle derived in this study (Figs. 4-11).

Detail of the calculation based on Stokes' law is described in Yasuda and Fujii (1998). The calculations were carried out only on the upper mantle (>~660 km). In the calculation, we fixed parameters to be ΔT = 300ºC, a_b = 12.4 km and E = 200ºC, where ΔT, a_b and E are temperature excess, diameter of a block of oceanic crust and arbitrary parameter which expresses the effect of excess temperature on the viscosity in the diapir, respectively. The a_b = 12.4 km corresponds to 1000 km^3 for volume of the oceanic crust block (Takahashi and Nakajima, 2002). If absolute ascending velocity $V = V_d - V_b$ is positive thoughout the upper mantle, we judged that the oceanic crust can ascend to Earth's surface, where V_d and V_b are ascent velocity of composite plume and descent velocity of the oceanic crust relative to the ascending plume, respectively. We used viscosity profile by Steinberger (2000) with some modifications for the mantle viscosity.

As a result, the plume with a_d = 300 km can bring the 8.5 vol% oceanic crust block at the maximum, where a_d is diameter of the diapir. The minimum size of the plume which can bring the oceanic crust block is a_d = 165 km. Compared to the results by Yasuda and Fujii (1998), present results show that it is more difficult to bring the oceanic crust up to Earth's surface by the mantle plume. This is mainly due to the use of the phase diagram of MORB by Aoki and Takahashi (2002). The Cpx/Grt ratio in MORB determined by Aoki and Takahashi (2002) is much lower than that by Irifune et al. (19686), which was used for the calculation by Yasuda and Fujii (1998). The higher content of Grt makes MORB denser at the depths <~450 km, as a

consequence, it makes difficult to bring the oceanic crust up. It is obvious that more strict calculations (e.g. including deformation of diapir) are needed for more qualitative discussion on this issue.

Seismic heterogeneity at the top of the lower mantle

As shown above, the differences between the oceanic crust (MORB) and the ambient mantle (pyrolite) in V_P and V_S become large at 300–400 and 660–730 km depths (Fig. 4-11, 4-14). The differences are 4 ± 2% for V_P and 8 ± 2% for V_S at 300–400 km depth, and –7 ± 2% for V_P and –8 ± 3% for V_S at 700 km depth (Fig. 4-14). These large differences may be detectable by seismic observations.

Recently, seismic heterogeneities at the top of the lower mantle (710–900 km depth) around the Mariana slab are found by Krüger et al. (2001) and Kaneshima (2003). Some of the seismic heterogeneities locate at deeper depths compared to the depth of the large velocity difference between the oceanic crust and pyrolite (660–730 km). However, if the slow kinetics of Grt → MgPv phase transformation is taken into account, Grt in the oceanic crust may survive to deeper region (~1000 km depth) in the subducting slab (Kubo et al., 2002), and the large velocity difference may be preserved even at 900 km depth. Thus, these seismic heterogeneities could be explained as the former oceanic crust (Krüger et al., 2001; Kaneshima, 2003).

Seismic scatterers in the mid lower mantle

The seismic scattering bodies were found in the mid lower mantle by recent seismic array analyses of short period or broad band waveforms (e.g. Kaneshima and Helffrich, 1998, 1999, 2003; Castle and Creager, 1999). Kaneshima and Helffrich (1998, 1999, 2003) detected a conversion from S to P-wave within a low seismic velocity layer (>4% V_S difference compared to the surrounding mantle) in the mid lower mantle (~1000–1850 km depth) east of the Mariana and

Izu-Bonin subduction zones. The low velocity layer (~8 km thick) is at least 500 km by 300 km. Judged from its large velocity contrast and sharpness, the scattering body is estimated to be the subducted oceanic crust. However, the lack of data has been prevented to examine whether the low seismic velocity is plausible as the oceanic or not.

As shown above, the V_P and V_S for the oceanic crust (MORB) show drastic decrease in the mid lower mantle conditions (~1400–2100 km depths) by the effect of the phase transition of St (Fig. 4-12). The depth conditions of the mid-lower mantle scatterers (Kaneshima and Helffrich, 1998, 1999, 2002) are generally within the depth interval of the drastic decrease in V_P and V_S of the oceanic crust. The calculation with VRH average of G for St and VRH average for composite shear modulus (St-G_{VRH} in Fig. 4-12) yields >4% lower V_S for MORB than that for pyrolite at 1690–1890 km depths. The seismic scatterers can be explained as the subducted oceanic crust in terms of elasticity. It should be noted that our calculation includes considerable uncertainties. If we assume the phase boundary between rutile-type and $CaCl_2$-type in SiO_2 is independent of temperature, the sharp decrease in V_P and V_S would become shallow to ~1200 km depth. In this case, the low velocities region of MORB would show excellent match with depths of the seismic scatterers. The V_P and V_S of MORB around the transition is quite variable with calculation methods for aggregate shear modulus of St and elasticity of composite rock (see Fig. 4-12 and previous discussion).

From the calculated seismic velocities of MORB (Fig. 4-12), it is suspected that the subducted oceanic crust in the deep mantle would be detected more easily at ~1400–2100 km depths by seismic observation. Most of recent reports on the seismic scatterers in the mantle locate in the mid lower mantle (e.g. Kawakatsu and Niu, 1994, Le Stunff et al., 1995, Castle and Creager, 1999). These might be also related to the subducted oceanic crust with low seismic velocities.

The oceanic crust, which has been subducted from ~4.5 Ga, would be the most important

chemical and physical heterogeneity in the Earth's deep mantle. However, its behavior in the mantle is still not understood yet: Is it accumulated at the base of transition zone or at the core-mantle boundary? dispersed in the whole mantle? etc.. Present results provide powerful information to investigate these issues.

Acknowledgements

I am grateful to Prof. Eiichi Takahashi for his valuable advice, continuing encouragement, discussion and review of this manuscript. Thanks are also due to S. Kaneshima, T. Tsuchiya, Y. Takei and I. Kumagai for useful discussions. Constructive comments by T. Katsura, T. Irifune, K. Hirose, S. Maruyama and K. Kawamura are very helpful in improving the manuscript. I also like to thank the members of our laboratory and others who have given advice and encouragement. Y.N. is grateful for the Research Fellowships of the Japan Society of the Promotion id Science for Young Scientists.

References

Akaogi, M., Akimoto, S., 1979. High-pressure phase equilibria in a garnet lherzolite, with special reference to Mg^{2+}-Fe^{2+} partitioning among constituent minerals. Phys. Earth Planet. Int. 19, 31–51.

Akaogi, M., Navrotsky, A., Yagi, T., Akimoto, S., 1987. Pyroxene-garnet transformation: thermochemistry and elasticity of garnet solid solutions, and application to a pyrolite mantle. In: Manghnani, M.H., Syono, Y. (Eds.), High-Pressure Reserch in Mineral Physics. Am. Geophys. Union, Washington, DC, pp. 251–260.

Akaogi, M., Ito, E., Navrotsky, A., 1989. Olivine-modified spinel-spinel transitions in the system Mg_2SiO_4-Fe_2SiO_4: calorimetric measurements, thermochemical calculation, and geophysical application. J.Geophys. Res. 94, 15671–15685.

Akaogi, M., Hamada, Y., Suzuki, T., Kobayashi, M., Okada, M., 1999. High pressure transitions in the system $MgAl_2O_4$-$CaAl_2O_4$: a new hexagonal aluminous phase with implication for the lower mantle. Phys. Earth Planet. Int. 115, 67–77.

Akaogi, M., Tanaka, A., Ito, E., 2002. Garnet-ilmenite-perovskite transitions in the system $Mg_4Si_4O_{12}$-$Mg_3Al_2Si_3O_{12}$ at high pressures and high temperatures: phase equilibria, calorimetry and implications for mantle structure. Phys. Earth Planet. Int. 132, 303–324.

Anderson, D.L., 1988. Temperature and pressure derivatives of elastic constants with application to the mantle. J. Geophys. Res. 93, 4688–4700.

Andrault, D., Fiquet, G., Guyot, F. Hanfland, M., 1998. Pressure-induced Landau-type transition in stishovite. Science 282, 720–724.

Andrault, D., Bolfan-Casanova, N., Guignot, N., 2001. Equation of state of lower mantle (Al,Fe)-$MgSiO_3$ perovskite. Earth Planet. Sci. Lett. 193, 501–508.

Angel, R.J., Hugh-Jones, D.A., 1994. Equation of state and thermodynamic properties of enstatite. J. Geophys. Res. 99, 19777–19783.

Angel, R.J., Jackson, J.M., 2002. Elasticity and equation of state of orthoenstatite, $MgSiO_3$. Am. Mineral. 87, 558–561.

Aoki, I., Takahashi, E., 2002. Density of MORB eclogite in the upper mantle. Phys. Earth Planet. Int. (submitted).

Bass, J.D., Anderson, D.L., 1984. Composition of the upper mantle: geophysical tests of two petrological models. Geophys. Res. Lett. 11, 237–240.

Brodholt, J.P., 2000. Pressure-induced changes in the compression mechanism of aluminous perovskite in the Earth's mantle. Nature 407, 620–622.

Brown, J.M., Shankland, T.J., 1981. Thermodynamic parameters in the Earth as determined from seismic profiles. Geophys. J. R. astr. Soc. 66, 579–596.

Carpenter, M.A., Hemley, R.J., Mao, H.-k., 2000. High-pressure elasticity of stishovite and the

$P4_2/mnm$ = Pnnm phase transition. J. Geophys. Res. 105, 10807–10816.

Castle, J.C., Creager, K.C., 1999. A steeply dipping discontinuity in the lower mantle beneath Izu-Bonin. J. Geophys. Res. 104, 7279–7292.

Chai, M., Brown, J.M., Slutsky, L.J., 1997. The elastic constants of a pyrope-grossular-almandine garnet to 20 GPa. Geophys. Res. Lett. 24, 523–526.

Chen, G., Liebermann, R.C., Weindner, D.J., 1998. Elasticity of single-crystal MgO to 8 gigapascals and 1600 kelvin. Science 280, 1913–1916.

Chen, G., Cooke, J.A., Gwanmesia, G.D., Liebermann, R.C., 1999. Elastic wave velocoties of $Mg_3Al_2Si_3O_{12}$-pyrope garnet to 10 GPa. Am. Mineral. 84, 384–388.

Cohen, R.E., 1992. First-principles predictions of elasticity and phase transitions in high pressure SiO_2 and Geophysical implications. In: Syono, Y., Manghnani, M.H. (Eds.), High-Pressure Reserch: Application to Earth and Planetary Sciences. Am. Geophys. Union, Washington, DC, pp. 425–431.

Conrad, P.G., Zha, C.-s., Mao, H.-k., Hemley, R.J., 1999. The high-pressure, single-crystal elasticity of pyrope, grossular, and andradite. Am. Mineral. 84, 374–383.

Daniel, I., Cardon, H., Fiquet, G., Guyot, F., Mezouar, M., 2001. Equation of state of Al-bearing perovskite to lower mantle pressure conditions. Geophys. Res. Lett. 28, 3789–3792.

Dubrovinsky, L.S., Dubrovinskaia, N.A., Saxena, S.K., Tutti, F., Rekhi, S., Le Bihan, T., Shen, G., Hu, J., 2001. Pressure-induced transformations of cristobalite. Chem. Phys. Lett. 333, 264–270.

Duffy, T.S., Anderson, D.L., 1989. Seismic velocities in mantle minerals and the mineralogy of the upper mantle. J. Geophys. Res. 94, 1895–1912.

Duffy, T.S., Ahrens, T.J., 1995. Compressional sound velocity, equation of state, and constitutive response of shock-compressed magnesium oxide. J. Geophys. Res. 100, 529–542.

Dziewonski, A.M., Anderson, D.L., 1981. Preliminary reference Earth model. Phys. Earth Planet.

Int. 25, 297–356.

Flesch, L.M., Li, B., Liebermann, R.C., 1998. Sound velocities of polycrystalline $MgSiO_3$-orthopyroxene to 10 GPa at room temperature. Am. Mineral. 83, 444–450.

Funamori, N., Yagi, T., Utsumi, W., Kondo, T., Uchida, T., Funamori, M., 1996. Thermoelastic properties of $MgSiO_3$ perovskite determined by in situ X ray observations up to 30 GPa and

2000 K. J. Geophys. Res. 101, 8257–8269.

Gwanmesia, G.D., Chen, G., Liebermann, R.C., 1998. Sound velocities in $MgSiO_3$-garnet to 8 GPa. Geophys. Res. Lett. 25, 4553–4556.

Hauri, E.H., 1996. Major-element variability in the Hawaiian mantle plume. Nature 382, 415–419.

Hirose, K., Fei, Y., Ma, Y., Mao, H.-k., 1999. The fate of subducted basaltic crust in the Earth's lower mantle. Nature 397, 53–56.

Hirose, K., 2002. Phase transitions in pyrolitic mantle around 670-km depth: implications for upwelling of plumes from the lower mantle. J. Geophys. Res. 107, 10.1029/2001JB000597.

Hirose, K., Fei, Y., 2002. Subsolidus and melting phase relations of basaltic composition in the uppermost lower mantle. Geochim. Cosmochim. Acta 66, 2099–2108.

Hofmann, A.W., White, W.M., 1982. Mantle plumes from ancient oceanic crust. Earth Planet. Sci. Lett. 57, 421–436.

Hugh-Jones, D.A., Angel, R.J., 1994. A compressional study of $MgSiO_3$ orthoenstatite up to 8.5 GPa. Am. Mineral. 79, 405–410.

Irifune, T., Sekine, T., Ringwood, A.E., Hibberson, W.O., 1986. The eclogite-garnetite transformation at high pressure and some geophysical implications. Earth Planet. Sci. Lett. 77, 245–256.

Irifune, T., 1987. An experimental investigation of the pyroxene-garnet transformation in a

pyrolite composition and its bearing on the constitution of the mantle. Phys. Earth Planet. Int. 45, 324–336.

Irifune, T., Ringwood, A.E., 1987. Phase transformations in primitive MORB and pyrolite compositions to 25 GPa and some geophysical implications. In: Manghnani, M.H., Syono, Y. (Eds.), High-Pressure Reserch in Mineral Physics. Am. Geophys. Union, Washington, DC, pp. 231–242.

Irifune, T., Ringwood, A.E., 1993. Phase transformations in subducted oceanic crust and buoyancy relationships at depths of 600–800 km in the mantle. Earth Planet. Sci. Lett. 117, 101–110.

Irifune, T., 1994. Absence of an aluminous phase in the upper part of the Earth's lower mantle. Nature 370. 131–133.

Irifune, T., Isshiki, M., 1998. Iron partitioning in a pyrolite mantle and the nature of the 410-km seismic discontinuity. Nature 392, 702–705.

Isaak, D., 1993. The mixed P, T derivatives of elastic moduli and implications on extrapolating throughout Earth's mantle. Phys. Earth Planet. Int. 80, 37–48.

Ita, J., Stixrude, L., 1992. Petrology, elasticity, and composition of the mantle transition zone. J. Geophys. Res. 97, 6849–6866.

Ito, E., Yamada, H., 1982. Stability relations of silicate spinels, ilmenites, and perovskites. In: Akimoto, S., Manghnani, M.H. (Eds.), High-Pressure Reserch in Geophysics. CAPJ, Tokyo, pp. 405–419.

Ito, E., Katsura, T., 1989. A temperature profile of the mantle transition zone. Geophys. Res. Lett. 16, 425–428.

Ito, H., Kawada, K., Akimoto, S., 1974. Thermal expansion of stishovite. Phys. Earth Planet. Int. 8, 277–281.

Jackson, I., Niesler, H., 1982. The elasticity of periclase to 3 GPa and some geophysical

implications. In: Akimoto, S., Manghnani, M.H. (Eds.), High-Pressure Research in Geophysics. CAPJ, Tokyo, pp. 93–113.

Jackson, M.J., Sinogeikin, S.V., Bass, J.D., 1999. Elasticity of $MgSiO_3$ orthoenstatite. Am. Mineral. 84, 677–680.

Jacobsen, S.D., Reichmann, H.J., Spetzler, H.A., Mackwell, S.J., Smyth, J.R., Angel, R.J., McCammon, C.A., , 2002. Structure and elasticity of single-crystal (Mg,Fe)O and a new method of generating shear waves for gigahertz ultrasonic interferometry. J. Geophys. Res. 107, 10.1029/2001JB000490.

Kneshima, S., 2003. Small scale heterogeneity at the top of the lower mantle around the Mariana slab. Earth Planet. Sci. Lett., (submitted).

Kaneshima, S., Helffrich, G., 1998. Detection of lower mantle scatterers northeast of the Mariana subduction zone using short-period array data. J. Geophys. Res. 103, 4825–4838.

Kaneshima, S., Helffrich, G., 1999. Dipping low-velocity layer in the mid-lower mantle: evidence for geochemical heterogeneity. Science 283, 1888–1891.

Kaneshima, S., Helffrich, G., 2003. Subparallel dipping heterogeneities in the mid-lower mantle. J. Geophys. Res., in press.

Karki, B.B., Warren, M.C., Stixrude, L., Ackland, G.J., Crain, J., 1997a. Ab initio studies of high-pressure structural transformations in silica. Phys. Rev. B 55, 3465–3471. (Erratum, Phys. Rev. B 56, 2884–2884, 1997)

Karki, B.B., Stixrude, L., Crain, J., 1997b. Ab initio elasticity of three high-pressure polymorphs of silica. Geophys. Res. Lett. 24, 3269–3272.

Karki, B.B., Crain, J., 1998. First-principles determination of elastic properties of $CaSiO_3$ perovskite at lower mantle pressures. Geophys. Res. Lett. 25, 2741–2744.

Katsura, T., Mayama, N., Shouno, K., Sakai, M., Yoneda, A., Suzuki, I., 2001. Temperature derivatives of elastic moduli of $(Mg_{0.91}Fe_{0.09})_2SiO_4$ modified spinel. Phys. Earth Planet. Int.

124, 163–166.

Kawakatsu, H., Niu, F., 1994. Seismic evidence for a 920-km discontinuity in the mantle. Nature 371, 301–305.

Kennett, B.L.N., Engdahl, E.R., Buland, R., 1995. Constraints on seismic velocities in the Earth from traveltimes. Geophys. J. Int. 122, 108–124.

Kesson, S.E., Fitz Gerald, J.D., Shelly, J.M.G., 1994. Mineral chemistry and density of subducted basaltic crust at lower-mantle pressures. Nature 372, 767–769.

Kesson, S.E., Fitz Gerald, J.D., Shelley, J.M., 1998. Mineralogy and dynamics of a pyrolite lower mantle. Nature 393, 252–255.

Kiefer, B., Stixrude, L., Wentzcovitch, R.M., 2002. Elasticity of $(Mg,Fe)SiO_3$-perovskite at high pressures. Geophys. Res. Lett. 29, 10.1029/2002GL014683.

Kingma, K.J., Cohen, R.E., Hemley, R.J., Mao, H.-k., 1995. Transformation of stishovite to a denser phase at lower-mantle pressures. Nature 374, 243–245.

Kojitani, H., Miyajima, N., 2002. Mineral chemistry of Al-bearing materials in the Earth's lower mantle. Rev. High Pres. Sci. Tech. 12, 126–137.

Krüger, F., Baumann, M., Scherbaum, F., Weber, M., 2001. Mid mantle scatterers near the Mariana slab detected with a double array method. Geophys. Res. Lett. 28, 667–670.

Kubo, A., Yagi, T., Ono, S., Akaogi, M., 2000. Compressibility of $Mg_{0.9}Al_{0.2}Si_{0.9}O_3$ perovskite. Proc. Jpn. Acad. 76, 103–107.

Kubo, T., Ohtani, E., Kondo, T., Kato, T., Toma, M., Hosoya, T., Sano, A., Kikegawa, T., Nagase, T., 2002. Metastable garnet in oceanic crust at the top of the lower mantle. Nature 420 803–806.

Kung, J., Li, B., Weidner, D.J., Zhang, J., Liebermann, R.C., 2002. Elasticity of $(Mg_{0.83},Fe_{0.17})O$ ferropericlase at high pressure: ultrasonic measurements in conjunction with X-radiation techniques. Earth Planet. Sci. Lett. 203, 557–566.

Le Stunff, Y., Wicks Jr., C.W., Romanovicz, B., 1995. P´P´ precursors under Africa: evidence for mid-mantle reflectors. Science 270, 74–77.

Levien, L., Prewitt, C.T., 1981. High-pressure crystal structure and compressibility of coesite. Am. Mineral. 66, 324–333.

Li, B., Rigden, S.M., Liebermann, R.C., 1996. Elasticity of stishovite at high pressure. Phys. Earth Planet. Int. 96, 113–127.

Li. B., Liebermann, R.C., Weidner, D.J., 1998. Elastic moduli of wadsleyite (β-Mg_2SiO_4) to 7 gigapascals and 873 kelvin. Science 281, 675–677.

Li, B., Liebermann, R.C., Weidner, D,J., 2001. P-V-V_P-V_S-T measurements on wadsleyite to 7 GPa and 873 K: Implications for the 410-km seismic discontinuity. J. Geophys. Res. 106, 30575–30591.

Liebermann, R.C., 2000. Elasticity of mantle minerals (experimental studies). In: Karato, S.-i., Forte, A., Liebermann, R., Masters, G., Stixrude, L. (Eds.), Earth's Deep Interior: Mineral Physics and Tomography From the Atomic to the Global Scale. Am. Geophys. Union, Washington, DC, pp. 181–199.

Liu, J., Zhang, J., Flesch, L., Li, B., Weidner, D.J., Liebermann, R.C., 1999. Thermal equation of state of stishovite. Phys. Earth Planet. Int. 112, 257–266.

Liu, J., Chen, G., Gwanmesia, G., Liebermann, R.C., 2000. Elastic wave velocities of pyrope-majorite garnets ($Py_{62}Mj_{38}$ and $Py_{50}Mj_{50}$) to 9 GPa. Phys. Earth Planet. Int. 120, 153–163.

Mao, H.K., Hemley, R.J., Fei, Y., Shu, J.F., Chen, L.C., Jephcoat, A.P., Wu, Y., 1991. Effect of pressure, temperature, and composition on lattice parameters and density of (Fe,Mg)SiO_3-perovskites to 30 GPa. J. Geophys. Res. 96, 8069–8079.

Matsui, M., Parker, S.C., Leslie, M., 2000. The MD simulation of the equation of state of MgO: Application as a pressure calibration standard at high temperature and high pressure. Am. Mineral. 85, 312–316.

Miyajima, N., Yagi, T., Hirose, K., Kondo, T., Fujino, K., Miura, H., 2001. Potential host phase of aluminum and potassium in the Earth's lower mantle. Am. Mineral. 86, 740–746.

Nakayama, K., Nishihara, Y., Takahashi, E., Iguchi, T., Funakoshi, K., 2002. P-V-T equation of state of stishovite to 23 GPa and 1073 K. Phys. Earth Planet. Int. (in prep.).

Nishihara, Y., Takahashi, E., 2001. Phase relation and physical properties of an Al-depleted komatiite to 23 GPa. Earth Planet. Sci. Lett. 190, 65–77.

Nishihara, Y., Takahashi, E., Matsukage, K., Kikegawa, T., 2003a. Thermal equation of state of omphacite. Am. Mineral. 88, 80–86.

Nishihara, Y., Takahashi, E., Matsukage, K., Iguchi, T., Nakayama, K., Funakoshi, K., 2003b. Thermal equation of state of $(Mg_{0.91}Fe_{0.09})_2SiO_4$ ringwoodite. Phys. Earth Planet. Int., (submitted).

Ono, S., Yasuda, A., 1996. Compositional change of majoritic garnet in a MORB composition from 7 to 17 GPa and 1400 to 1600ºC. Phys. Earth Planet. Int. 96, 171–179.

Ono, S., Ito, E., Katsura, T., 2001. Mineralogy of subducted basaltic crust (MORB) from 25 to 37 GPa, and chemical heterogeneity of the lower mantle. Earth Planet. Sci. Lett. 190, 57–63.

Ono, S., Hirose, K., Murakami, M., Isshiki, M., 2002a. Post-stishovite phase boundary in SiO_2 determined by in situ X-ray observations. Earth Planet. Sci. Lett. 197, 187–192.

Ono, S., Hirose, K., Isshiki, M., Mibe, K., Saito, Y., 2002b. Equation of state of hexagonal aluminous phase in basaltic composition to 63 GPa at 300 K. Phys. Chem. Minerals 29, 527–531.

Ono, S., Hirose, K., Kikegawa, T., Saito, Y., 2002c. The compressibility of a natural composition calcium ferrite-type aluminous phase to 70 GPa. Phys. Earth Planet. Int. 131, 311–318.

Ringwood, A.E., 1962. A model for the upper mantle. J. Geophys. Res. 67, 857–867.

Silver, P.G., Carlson, R.W., Olson, P., 1988. Deep slabs, geochemical heterogeneity, and the

large-scale structure of mantle convection: investigation of an enduring paradox. Ann. Rev. Earth Planet. Sci. 16, 477–541.

Shim, S.-H., Duffy, T.S., Shen, G., 2000. The equation of state of $CaSiO_3$ perovskite to 108 GPa at 300 K. Phys. Earth Planet. Int. 120, 327–338.

Sinelnikov, Y.D., Chen, G., Liebermann, R.C., 1998. Elasticity of $CaTiO_3$-$CaSiO_3$ perovskites. Phys. Chem. Minerals 25, 515–521.

Sinogeikin, S.V., Bass, J.D., 2000. Single-crystal elasticity of pyrope and MgO to 20 GPa by Brillouin scattering in the diamond cell. Phys. Earth Planet. Int. 120, 43–62.

Sinogeikin, S.V., Bass, J.D., 2002a. Elasticity of majorite and a majorite-pyrope solid solution to high pressure: implications for the transition zone. Geophys. Res. Lett. 29, 10.1029/2001GL013937.

Skinner, B.J., 1966. Thermal expansion. In: Clark Jr., S.P., (Eds.), Handbook of Physical Constants, Geol. Soc. Am. Mem., pp. 75–95.

Smyth, J.R., McCormick, T.C., 1995. Crystallographic data for minerals. In: Ahrens, T.J. (Eds.), A Handbook of Physical Constants: Mineral Physics and Crystallography. Am. Geophys. Union, Washington, DC, pp. 1–17.

Steinberger, B., 2000. Slab in the lower mantle - results of dynamic modelling compared with tomographic images and the geoid. Phys. Earth Planet. Int. 118, 241–257.

Takahashi, E., 1986. Melting of a dry peridotite KLB-1 up to 14 GPa: implications on the origin of peridotitic upper mantle. J. Geophys. Res. 91, 9367–9382.

Takahashi, E., Nakajima, K., Wright, T.L., 1998. Origin of the Columbia River basalts: melting model of a heterogeneous plume head. Earth Planet. Sci. Lett. 162, 63–80.

Takahashi, E., Nakajima, K., 2002. Melting process in the Hawaiian plume: an experimental study. In: Takahashi, E., Lipman, P.W., Garcia, M.J., Naka, J., Aramaki, S. (Eds.), Hawaiian Volcanoes: Deep Underwater Perspectives. Am. Geophys.Union, Washington,

DC, pp. 403–418.

Vacher, P., Mocquet, A., Sotin, C., 1996. Comparison between tomographic structures and models of convection in the upper mantle. Geophys. J. Int. 124, 45–56.

Vacher, P., Mocquet, A. ,Sotin, C., 1998. Computation of seismic profiles from mineral physics: the importance of the non-olivine components for explaining the 660 km depth discontinuity. Phys. Eart Planet. Int. 106, 275–298.

Wang, Y., Weinder, D.J., Guyot, F., 1996. Thermal equation of state of $CaSiO_3$ perovskite. J. Geophys. Res. 101, 661–672.

Watanabe, H., 1982. Thermochemical properties of synthetic high-pressure compounds relevant to the Earth's mantle. In: Akimoto, S., and Manghnani, M.H. (Eds.), High-Pressure Research in Geophysics, pp. 441–464.

Watt, J.P., Davies, G.F., O'Connell, R.J., 1976. The elastic properties of composite materials. Rev. Geophys. Space Phys. 14, 541–563.

Weidner, D.J., Carleton, H.R., 1977. Elasticity of coesite. J. Geophys. Res. 82, 1334–1346.

Weidner, D.J., Wang, Y., 1998. Chemcal- and Clapeyron-induced buoyancy at the 660 km discontinuity. J. Geophys. Res. 103, 7431–7441.

Weidner, D.J., Wang, H., Ito, J., 1978. Elasticity of orthoenstatite. Phys. Earth Planet. Int. 17, P7–P13.

Weidner, D.J., Bass, J.D., Ringwood, A.E., Sinclair, W., 1982. The single-crystal elastic moduli of stishovite. J. Geophys. Res. 87, 4740–4746.

White, R., McKenzie, D., 1989. Magmatism at rift zones: the generation of volcanic continental margins and flood basalts. J. Geophys. Res. 94, 7685–7729.

Wolf, G.H., Jeanloz, R., 1985. Lattice dynamics and structural distortions of $CaSiO_3$ and $MgSiO_3$ perovskite. Geophys. Res. Lett. 12, 413–416.

Wood, B.J., 2000. Phase transformations and partitioning relations in peridotite under lower

mantle conditions. Earth Planet. Sci. Lett. 174, 341–354. (Erratum, Earth Planet. Sci. Lett. 176, 543–543, 2000)

Yasuda, A., Fujii, T., Kurita, K., 1994. Melting phase relations of an anhydrous mid-ocean ridge basalt from 3 to 20 GPa: implications for the behavior of subducted oceanic crust in the mantle. J. Geophys. Res. 99, 9401–9414.

Yasuda, A., Fujii, T., 1998. Ascending subducted oceanic crust entrained within mantle plumes. Geophys. Res. Lett. 25, 1561–1564.

Yeganeh-Haeri, A., 1994. Synthesis and re-investigation of the elastic properties of single-crystal magnesium silicate perovskite. Phys. Earth Planet. Int. 87, 111–121.

Zhang, J., Herzberg, C., 1994. Melting experiments on anhydrous peridotite KLB-1 from 5.0 to 22.5 GPa. J. Geophys. Res. 99, 17729–17742.

Zhang, J., Li, B., Utsumi, W., Liebermann, R.C., 1996. In situ X-ray observations of the coesite-stishovite transition: reversed phase boundary and kinetics. Phys. Chem. Minerals 23, 1–10.

Zhang, J., Weidner, D.J., 1999. Thermal equation of state of alminum-enriched silicate perovskite. Science 284, 782–784.

Table 4-1. Chemical compositions of mineral

Mineral	Ol	Wd	Rw	Opx	Ak
X_{Fe}[a]	0.09	0.10	0.11	0.08	0.04

Mineral	Cpx[b]		MgPv		Mw
	MORB	Pyrolite	MORB	Pyrolite	
X_{Fe}[a]	0.20	0.11	0.36	0.09	0.15

[a] X_{Fe} = Fe/(Mg + Fe) in molar ratio. [b] X_{Jd} = 0.35 and 0.15 for Cpx in MORB and pyrolite, respectively, X_{Jd} = Jd/(Di + Hd + Jd) in molar ratio, Di; diopside, Hd; hedenbergite; Jd; jadeite.

Table 4-2. Thermoelastic parameters of minerals

Mineral	Ol	Wd	Rw	Grt		Cpx		Opx
					Garnetite	MORB	Pyrolite	
ρ_0 (g cm^{-3})	3.328	3.596	3.691	$3.565+0.760X_{Fe}+0.032X_{Ca}-0.05X_{Mj}$		3.309	3.276	3.279
K_{S0} (GPa)	128	170	184[b]	$173+7X_{Fe}-5X_{Ca}-10X_{Mj}$	168[c]	127[d]	109.4	124
K'_S	4.3	4.2	5.1[b]	$5.3-0.4X_{Ca}$	5[c]	4[d]	5.8	5.6
$(\partial K_S/\partial T)_P$ (GPa K^{-1})	–0.016	–0.018	–0.025[b]	$-0.021+0.006X_{Ca}$	–0.026[c]	–0.012[d]	–0.013	–0.012
G_0 (GPa)	78	104	115	$92+7X_{Fe}+15X_{Ca}-3X_{Mj}$		72	69	76.1
G'	1.4	1.5	1.7	$2.0-0.4X_{Ca}$		1.7	1.7	1.4
$(\partial G/\partial T)_P$ (GPa K^{-1})	–0.014	–0.014	–0.014	$-0.010-0.002X_{Ca}$		–0.011	–0.010	–0.011
$\alpha = a + bT - cT^{-2} + dT^{-1}$								
a (10^{-5} K^{-1})	2.832	2.711	2.1[b]	$2.81-0.21X_{Ca}$	2.2[c]	2.2[d]	3.206	2.86
b (10^{-8} K^{-2})	0.758	0.6885	1.2[b]	$0.316+0.019X_{Ca}$	1.4[c]	–	0.811	0.72
c (K)	–	0.5767	–	$0.4587+0.235X_{Ca}$	–	–	1.8167	–
d (10^{-2})	–	–	–	–	–	–	0.1347	–
γ_G	1.13[a]	1.42[a]	1.24[a]	$1.24-0.18X_{Fe}-0.19X_{Ca}$[a]		1.04[a]	1.05[a]	0.97[a]

Table 4-2. (continued)

Mineral	MgPv	Mw	CaPv	Coe	St	HAP	CF	Ak
ρ_0 (g cm^{-3})	4.108+1.07X_{Fe}	3.926	4.210	2.909[q]	4.287[q]	4.145[n]	4.138[o]	3.854
K_{S0} (GPa)	264	167	235	96[f]	296[j]	200[n]	256[o]	212
K'_S	4	3.6	4.9	8.6[f]	4.5[j]	4.1[n]	3.6[o]	5.6
$(\partial K_S/\partial T)_P$ (GPa K^{-1})	–0.015	–0.019	–0.022	–0.020[g]	–0.037[j]	–0.016[e]	–0.021[e]	–0.017
G_0 (GPa)	177	127	150	62[h]	217[k]	140[e]	150[e]	130
G'	1.6	1.9	1.9	1.5[e]	1.8[k]	1.6[e]	1.6[e]	1.7
$(\partial G/\partial T)_P$ (GPa K^{-1})	–0.028	–0.024	–0.023	–0.014[e]	–0.018[l]	–0.014[e]	–0.014[e]	–0.017
$\alpha = a + bT - cT^{-2} + dT^{-1}$								
a (10^{-5} K^{-1})	1.982	3.681	3.01	0.543	1.3	2.5[e]	2.5[e]	2.27
b (10^{-8} K^{-2})	0.818	0.9283	0.43	0.8351	1.2[j]	–	–	0.682
c (K)	0.474	0.7445	–	0.0605[i]	–	–	–	–0.385
d (10^{-2})	–	–	–	–	–	–	–	–0.1808
γ_G	1.96[a]	1.47[a]	1.96[a]	0.35[g]	1.52[m]	1.5[e]	1.5[e]	1.5[p]

ρ_0; zero-pressure density, K_{S0}; adiabatic bulk modulus, G_0; shear modulus, K'_S and G'; pressure derivative of the moduli, $(\partial K_S/\partial T)_P$ and $(\partial G/\partial T)_P$; temperature derivative of moduli, α; thermal expansivity, γ_G; Grüneisen parameter. X_{Fe} is same as Table 4-1. X_{Ca} = Ca/(Mg+Fe+Ca) in molar ratio. X_{Mj} is majorite ($(Mg,Fe,Ca)_4Si_4O_{12}$) content. Data without annotation are collected from compilation by Vacher et al. (1998). Other data sources are [a] Ita and Stixrude (1992), [b] Chapter 2, [c] Chapter 3, [d] Chapter 1, [e] Assumed value, [f] Levien and Prewitt (1981), [g] Watanabe (1982), [h] Weidner and Carleton (1977), [i] Skinner (1966), [j] Nakayama et al. (2002), [k] Li et al. (1996), [l] Duffy and Anderson (1989), [m] Ito et al. (1974), [n] Ono et al. (2002b), [o] Ono et al. (2002c), [p] Weidner and Wang (1998), [q] Smyth and McCormick (1995).

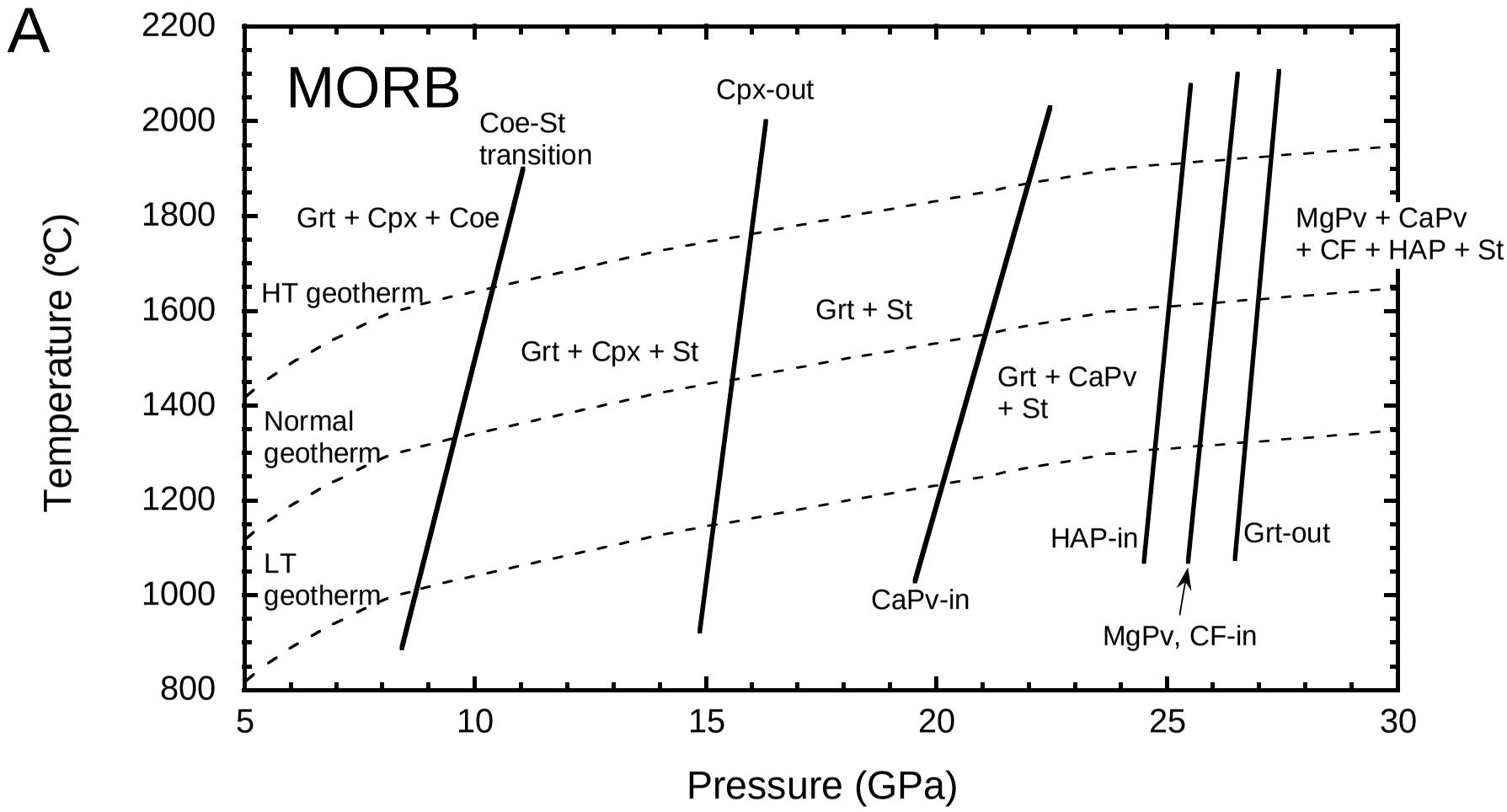
A
MORB
Coe-St
transition
Cpx-out
Grt + Cpx + Coe
HT geotherm
Grt + Cpx + St
Grt + St
Grt + CaPv
+ St
MgPv + CaPv
+ CF + HAP + St
Normal
geotherm
LT
geotherm
CaPv-in
HAP-in
Grt-out
MgPv, CF-in
Temperature (°C)
Pressure (GPa)
2200
2000
1800
1600
1400
1200
1000
800
5
10
15
20
25
30

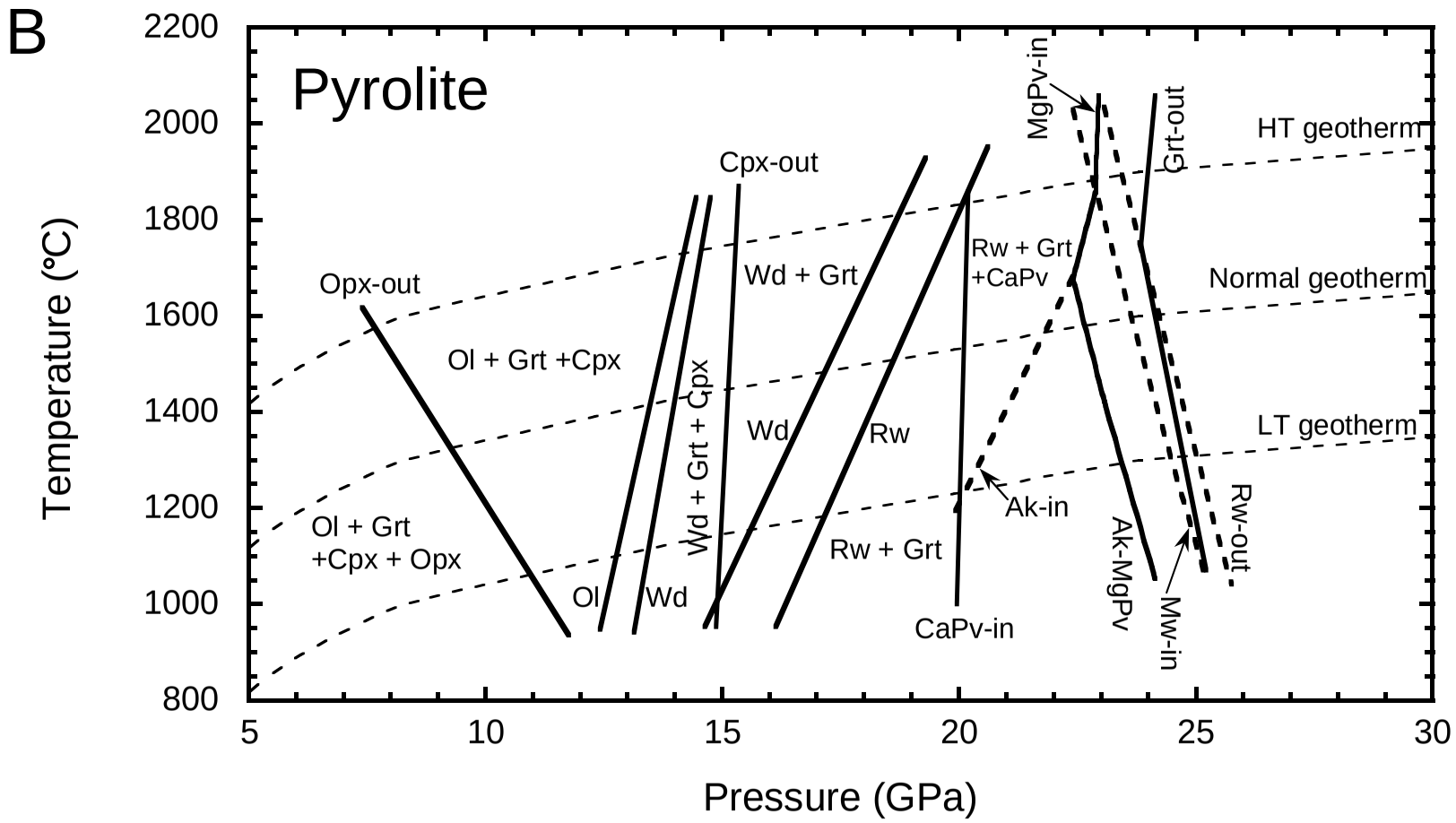

Fig. 4-1. Pressure -temperature phase diagram of (a) MORB and (b) pyrolite at 5-30 GPa and 800-2200℃. Bold lines are phase boudaries. Thin broken lines are normal geotherm (middle, Brown and Shankland, 1981), and +300℃ and -300℃ geotherms. abbreviations are Ol; olivine, Wd; wadsleyite, Rw; ringwoodite, Grt; garnet, Cpx; Ca-rich clinopyroxene, Opx; orthopyroxene, MgPv; Mg-rich silicate perovskite, Mw; magnesiowüstite, CaPv; Ca-rich silicate perovskite, Coe; coesite, St; stishovite, HAP; hexagonal aluminous phase, CF; Ca ferrite-type aluminous phase, Ak; akimotoite.

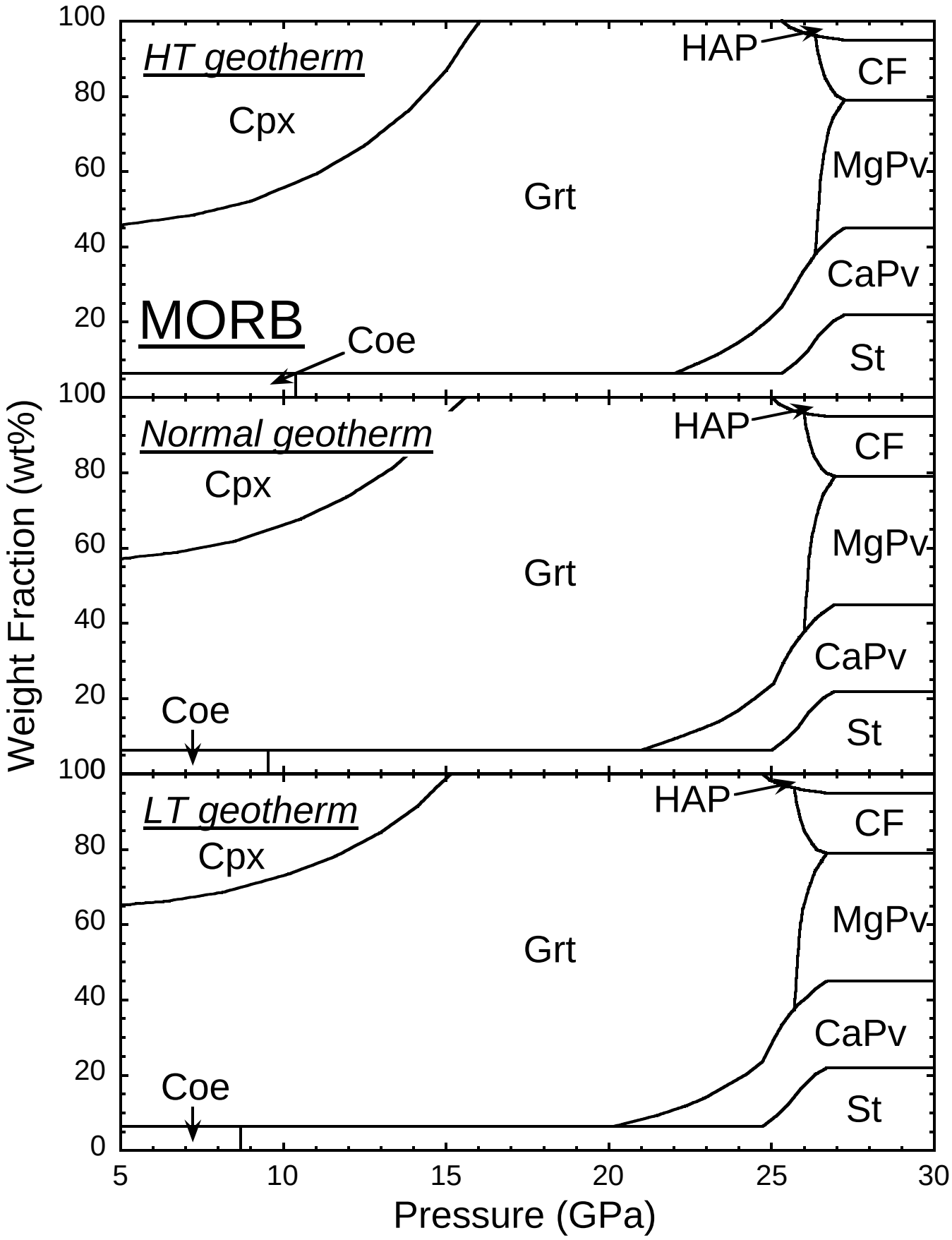

Fig. 4-2. Weight fractions in MORB along the three geotherms.

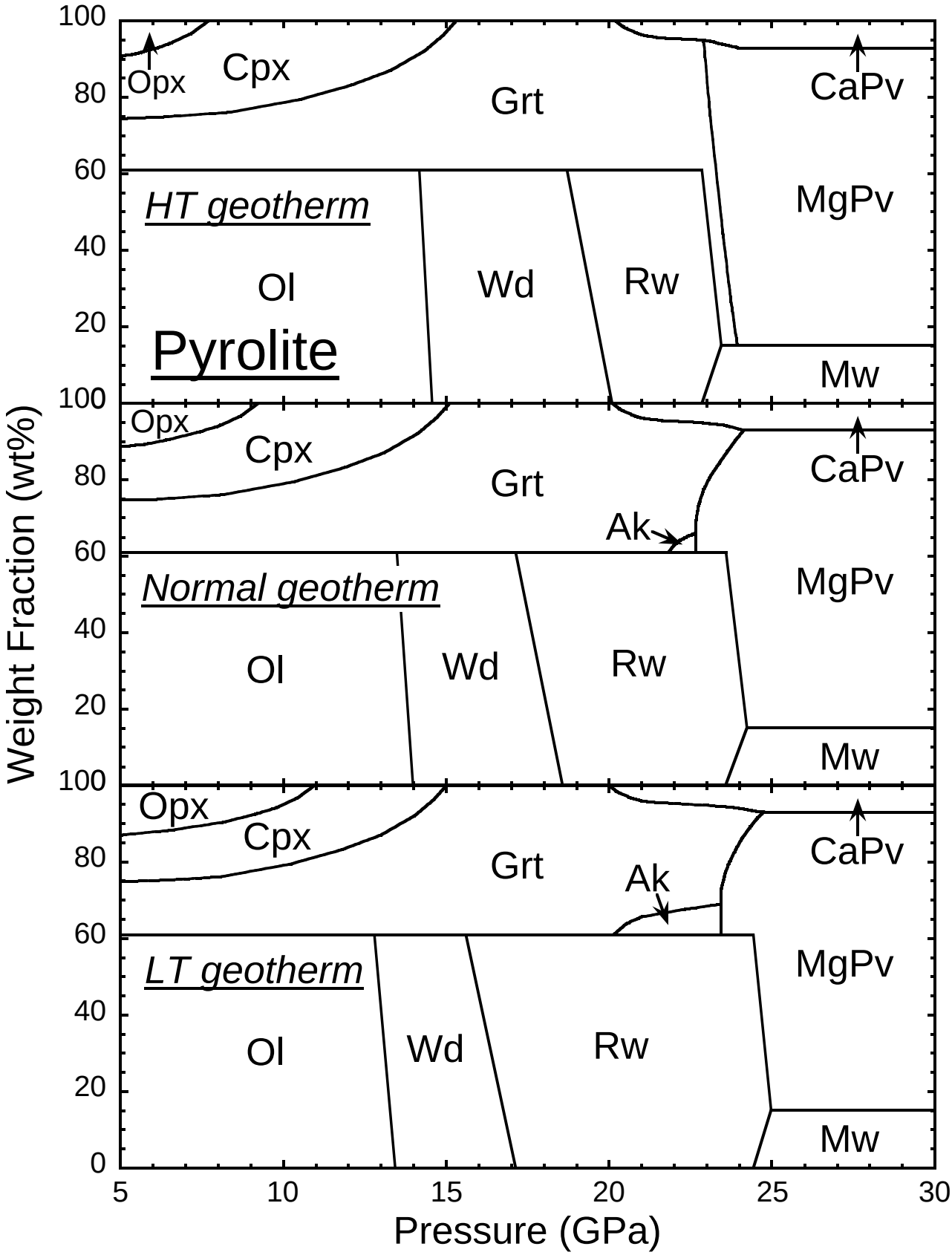

Fig. 4-3. Weight fractions in pyrolite along the three geotherms.

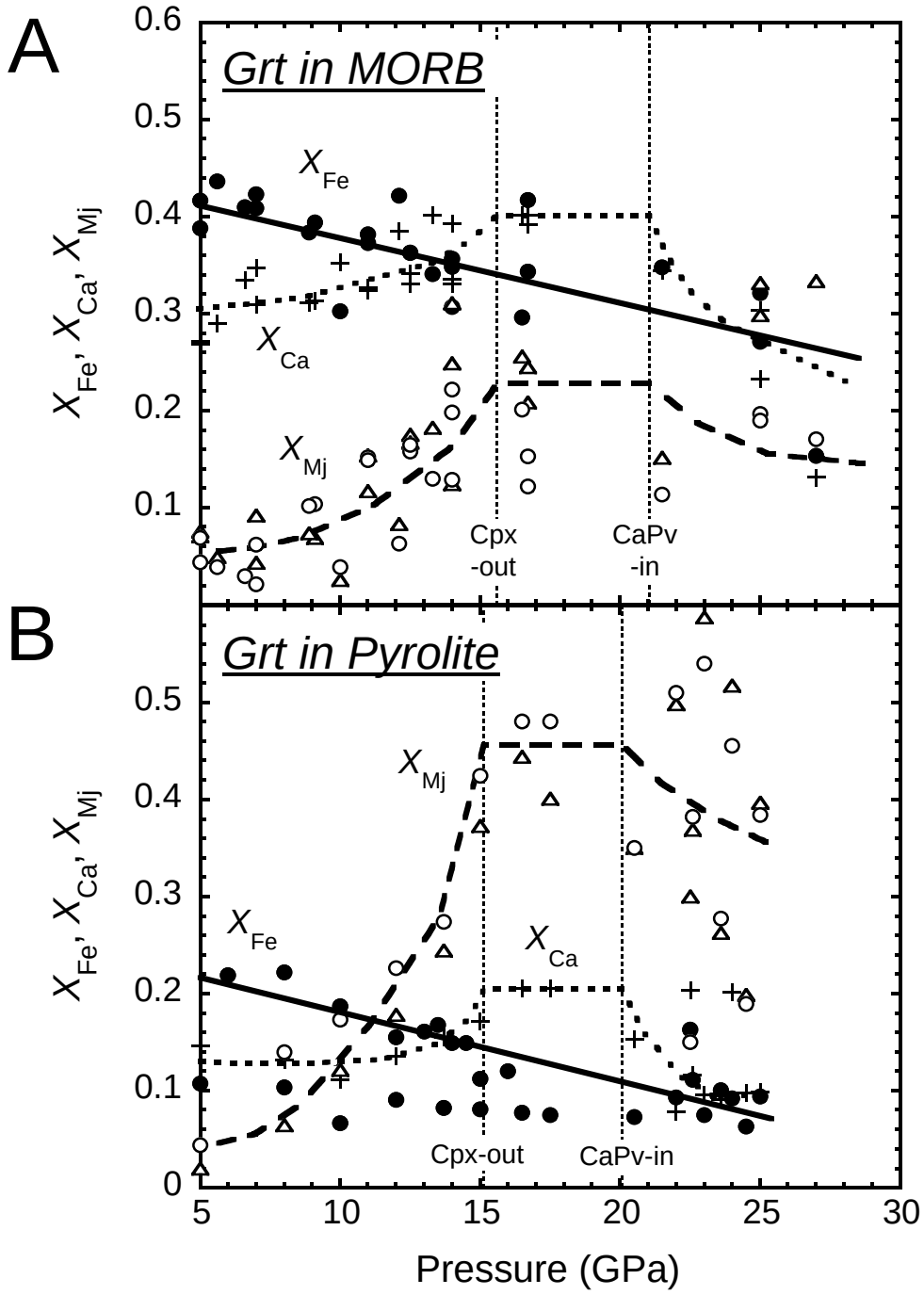

Fig. 4-4. Chemical compositions of garnet in (a) MORB and (b) pyrolite. Symbols are data by various phase equiriblium experiments. Solid cirecles and crosses are X_{Fe} and X_{Ca}, respectively. Open circles and triangles are X_{Mj} calculated from Al and Si contents, respectively. Bold lines are compositions used for calculating thermoelastic parameters along normal geotherm (Table 4-2). Pressures of Cpx-out and CaPv-in along the normal geotherm are shown by thin dotted lines. Data are from Irifune et al. (1986), Irifune and Ringwood (1993), Ono and Yasuda (1996), Ono et al. (2001) and Aoki and Takahashi (2002) for Grt in MORB, from Irifune (1987, 1994), Irifune and Ringwood (1987), Irifune and Isshiki (1998), Hirose (2002) for Grt in pyrolite.

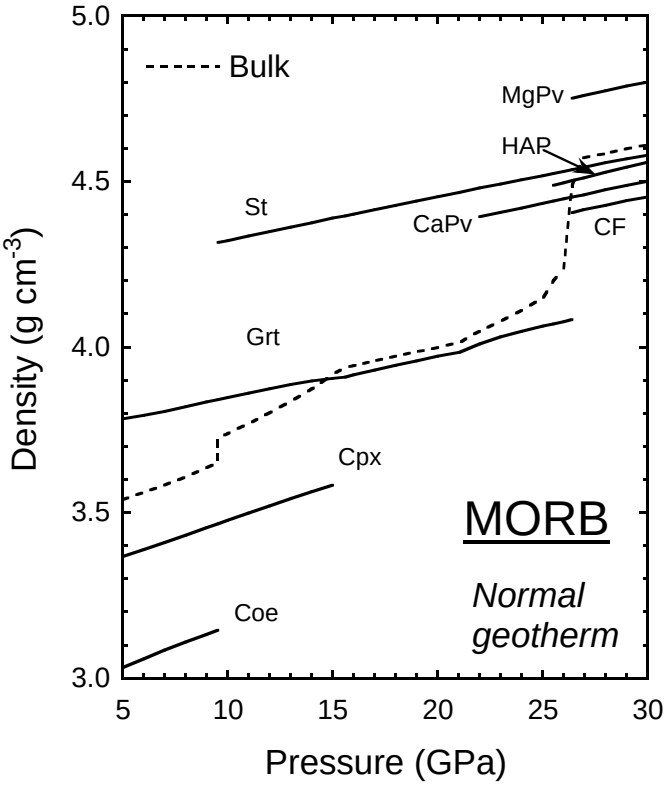

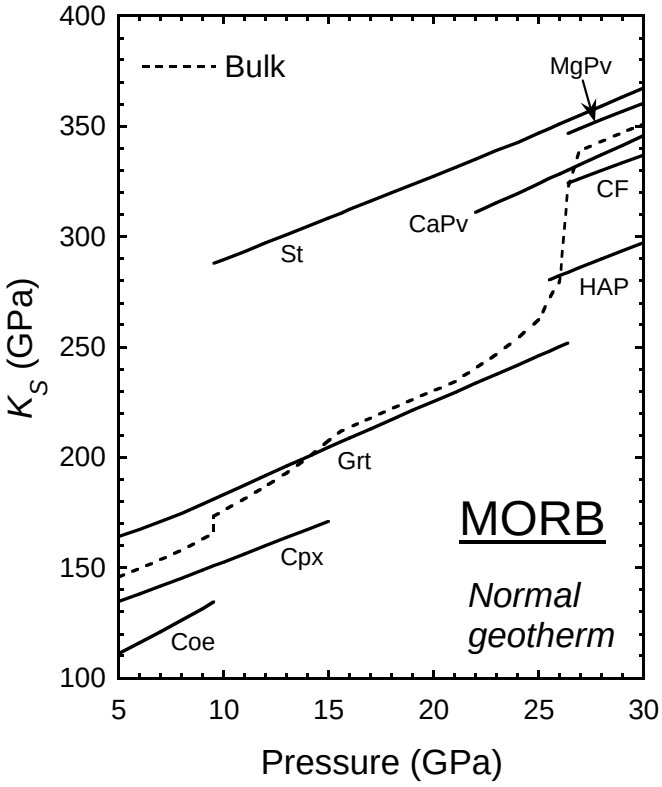

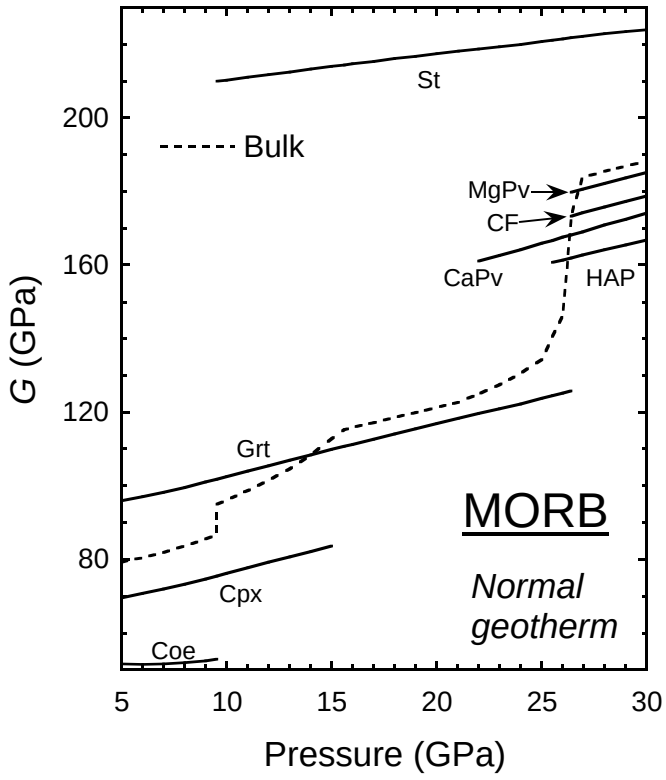

Fig. 4-5. Density and bulk and shear moduli of minerals in MORB along the normal geotherm to 30 GPa. Broken lines represent MORB bulk. VRH average of shear modulus of stishovite is plotted.

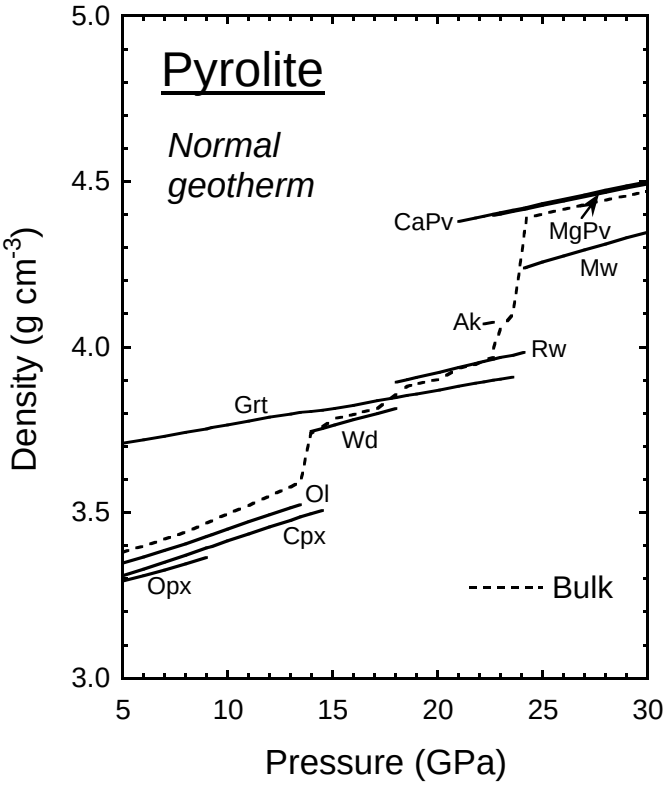

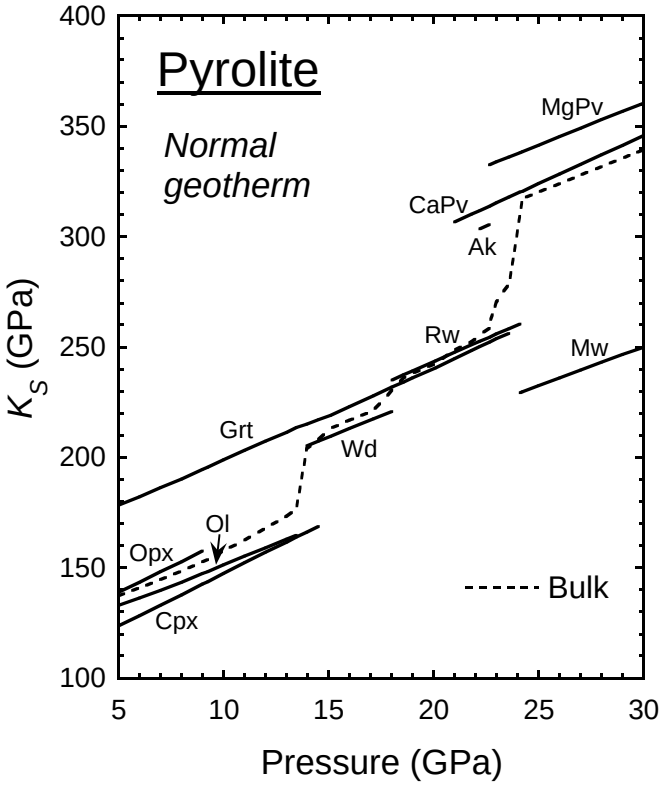

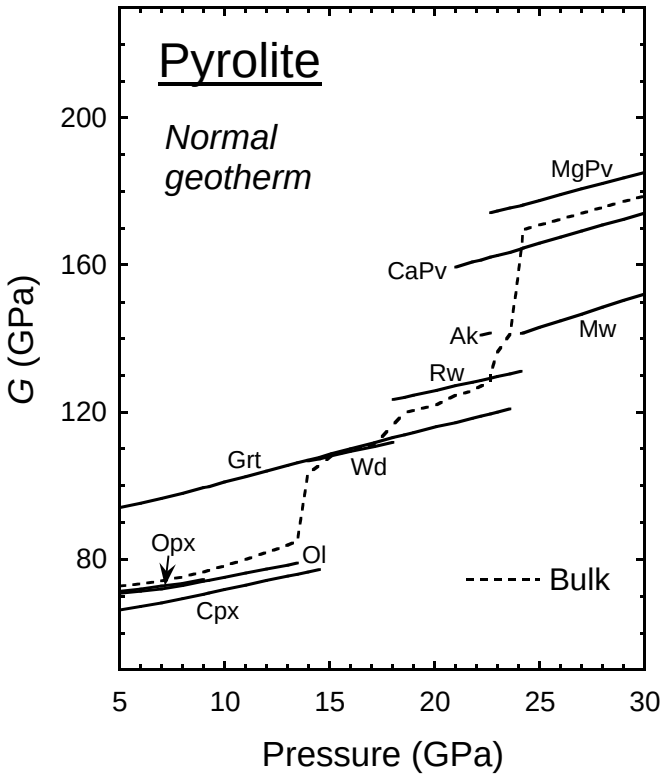

Fig. 4-6. Density and bulk and shear moduli of minerals in pyrolite along the normal geotherm to 30 GPa. Broken lines represent pyrolite bulk.

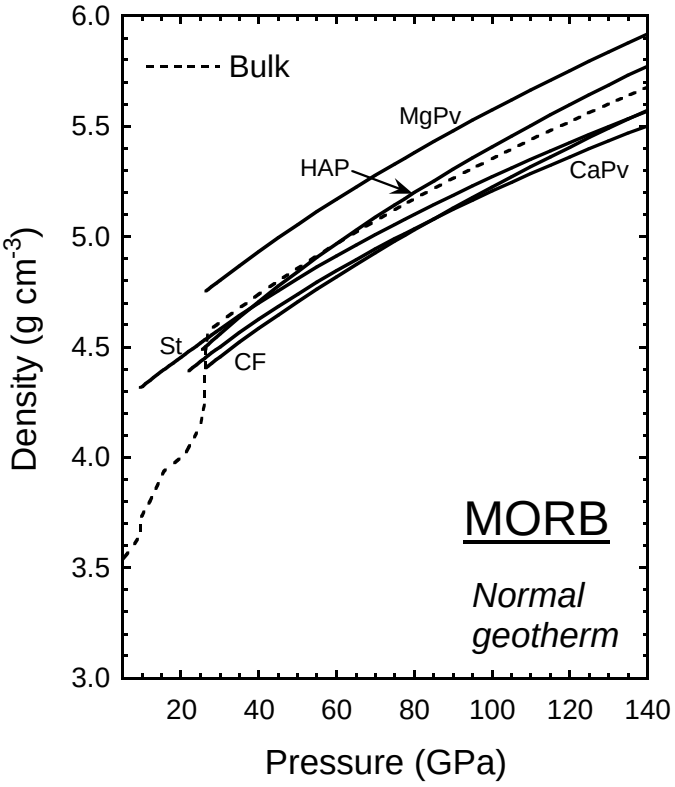

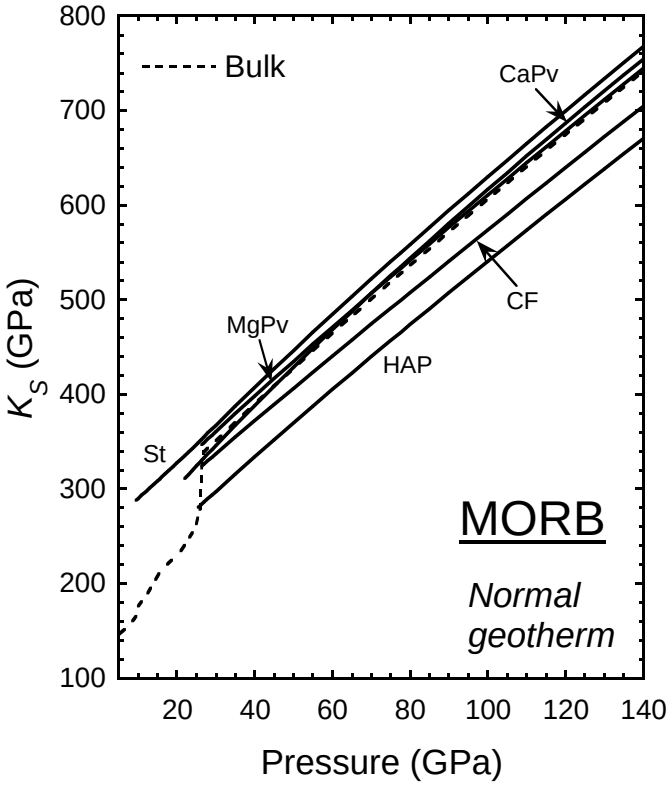

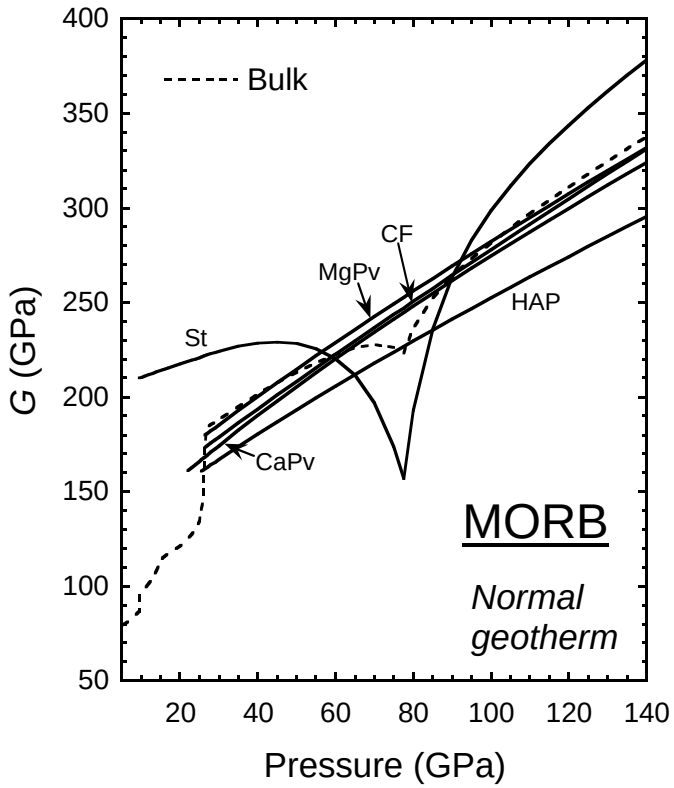

Fig. 4-7. Density and bulk and shear moduli of minerals in MORB along the normal geotherm to 140 GPa. Broken lines represent MORB bulk. VRH average of shear modulus of stishovite is plotted.

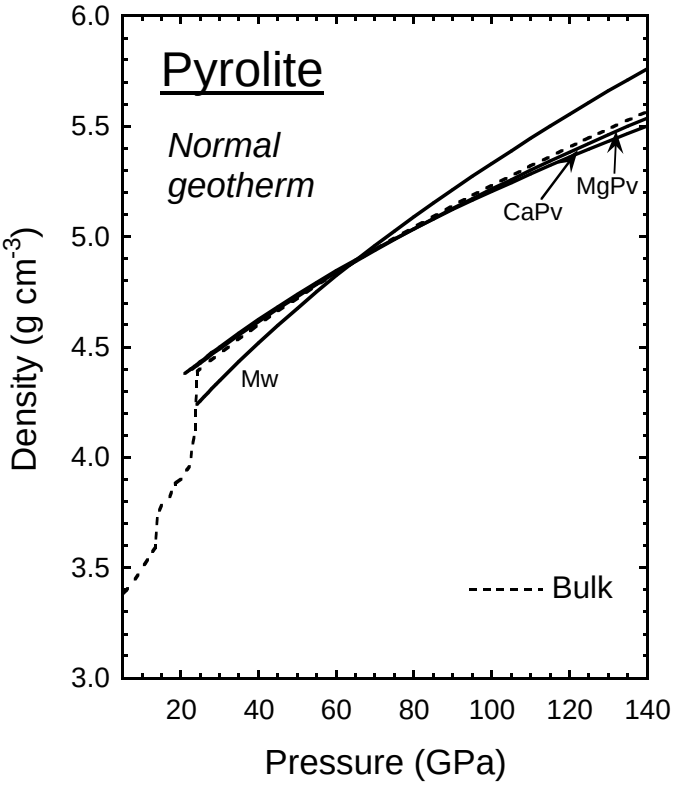

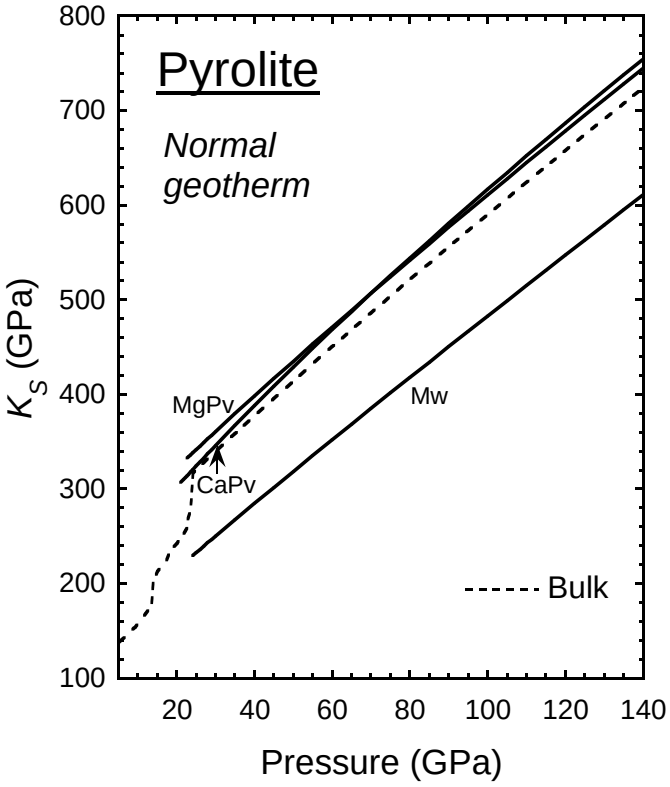

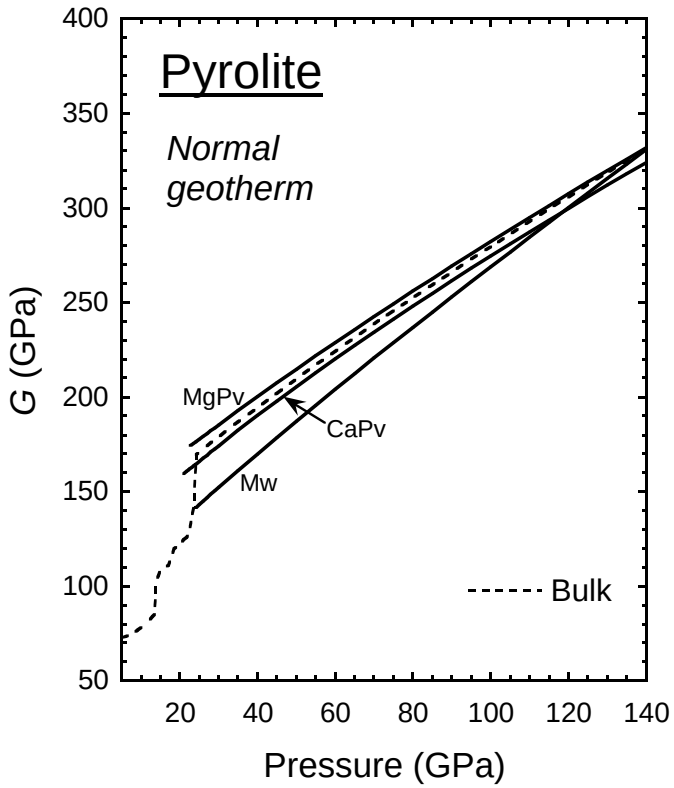

Fig. 4-8. Density and bulk and shear moduli of minerals in pyrolite along the normal geotherm to 140 GPa. Broken lines represent pyrolite bulk.

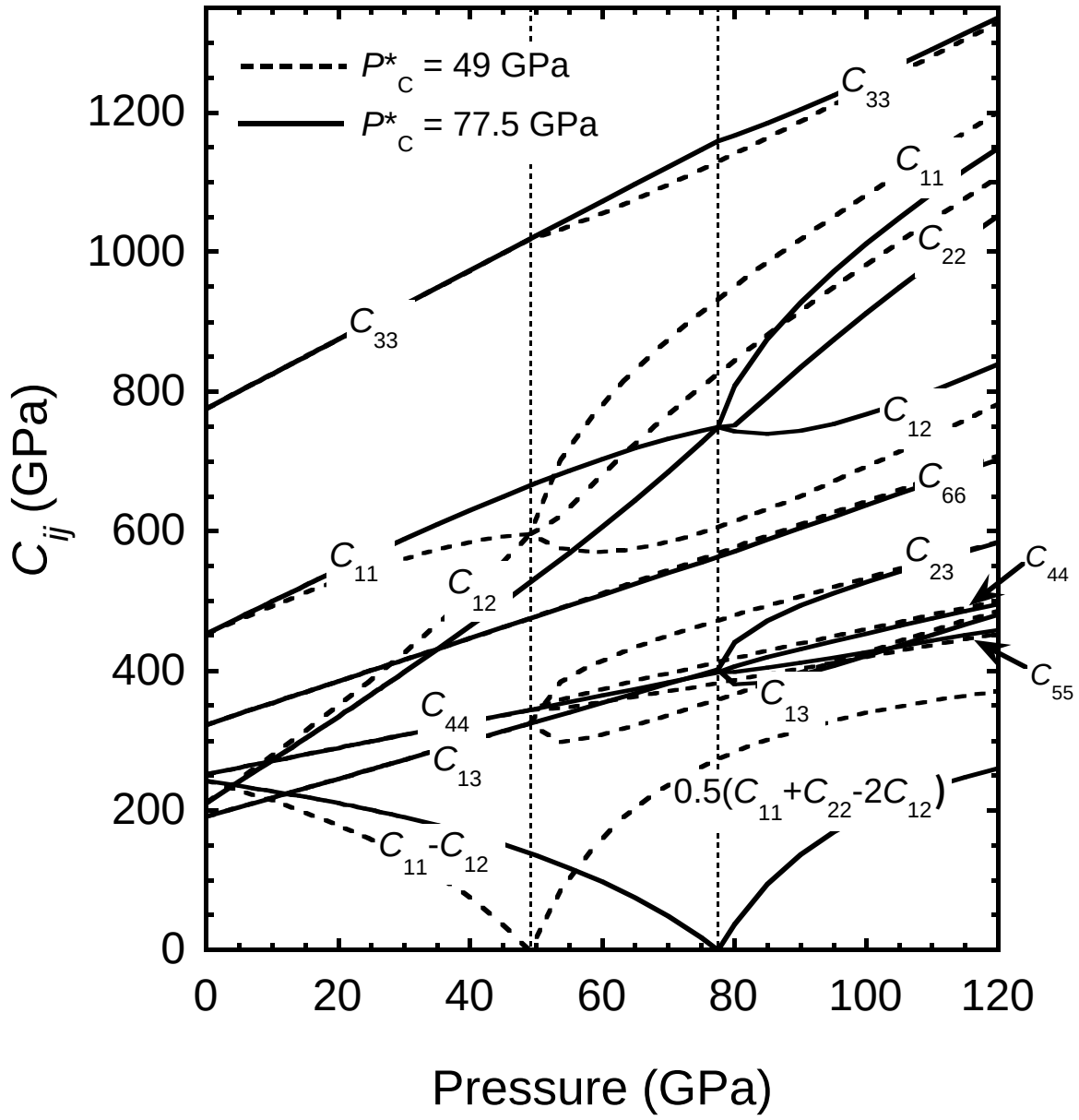

Fig. 4-9. Variations of elastic constants of stishovite. Broken lines are same as Fig. 4 of Carpenter et al. (2000). Solid lines are calculated with the modified transition pressure (P^*_C = 77.5 GPa) based on Landau theory. Pressures of the rutile-type to $CaCl_2$-type phase transition are shown by thin dotted line.

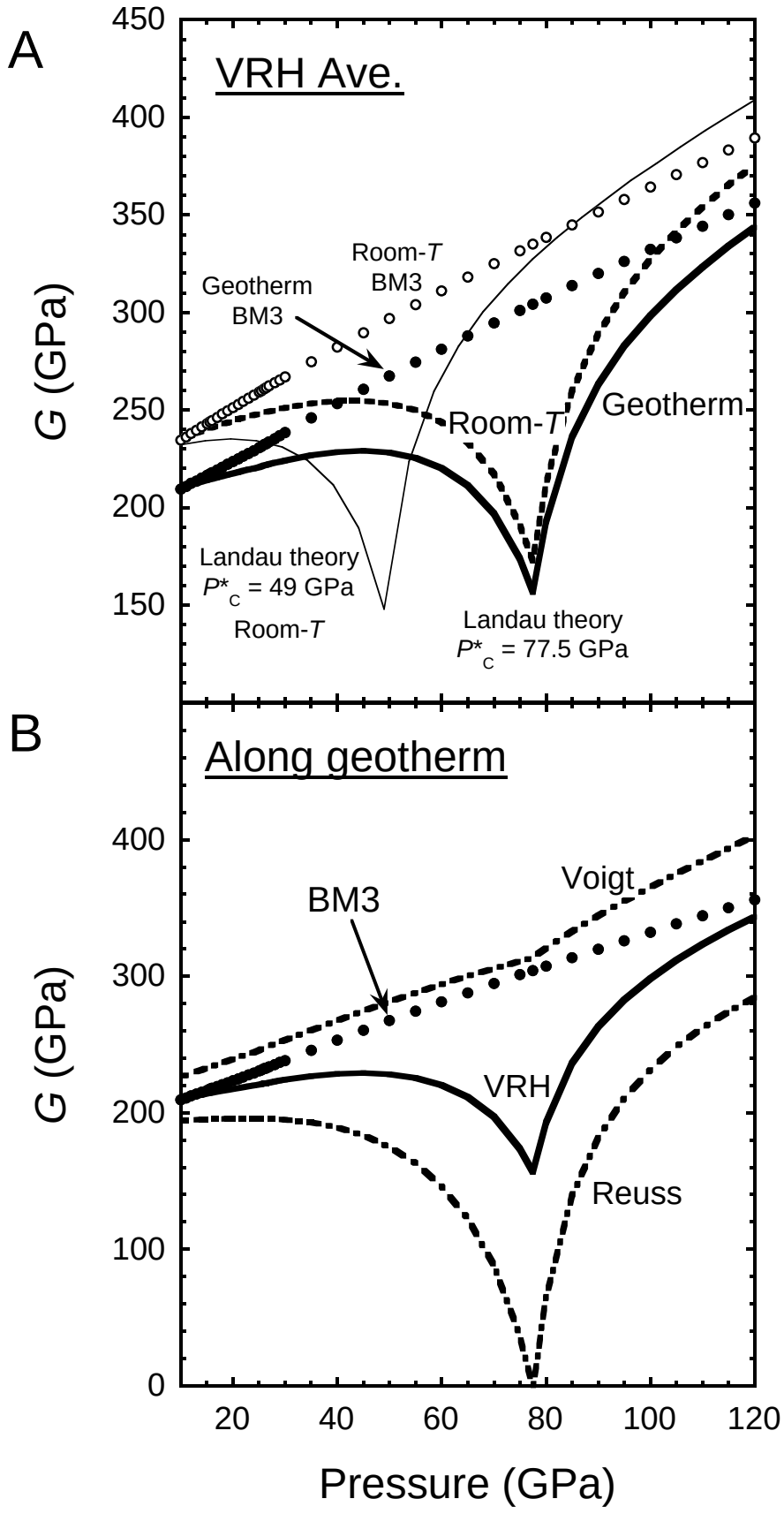

Fig. 4-10. Shear moduli of stishovite as a function of pressure. (a) Voigt-Reuss-Hill average (VRH) calculated from single crystal elastic constants (Fig. 4-9) and results of third order Birch-Murnaghan equation of state (BM3) using thermoelastic parameters listed in Table 4-2. (b) VRH (bold solid line) and Voigt and Reuss bounds (bold dotted dased lines) with results of BM3 (solid circles) along normal geotherm.

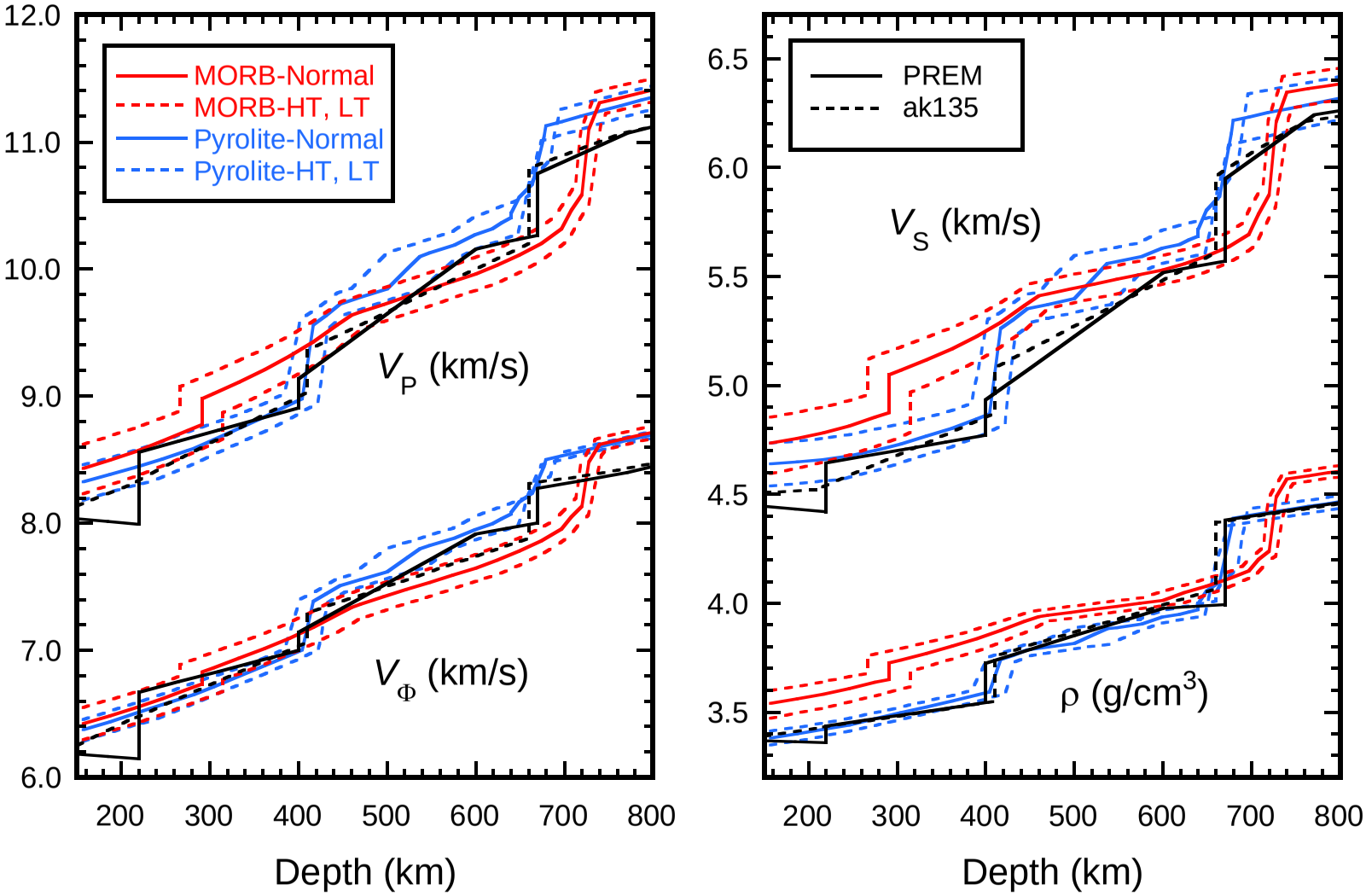

Fig. 4-11. Calculated density and seismic velocities of MORB and pyrolite to 800 km depth. Seismic models (PREM; Dziewonski and Anderson, 1981, ak135; Kennett et al., 1995) are also shown for comparison. Broken lines above and below solid lines are the results along the HT and LT geotherms, respectively.

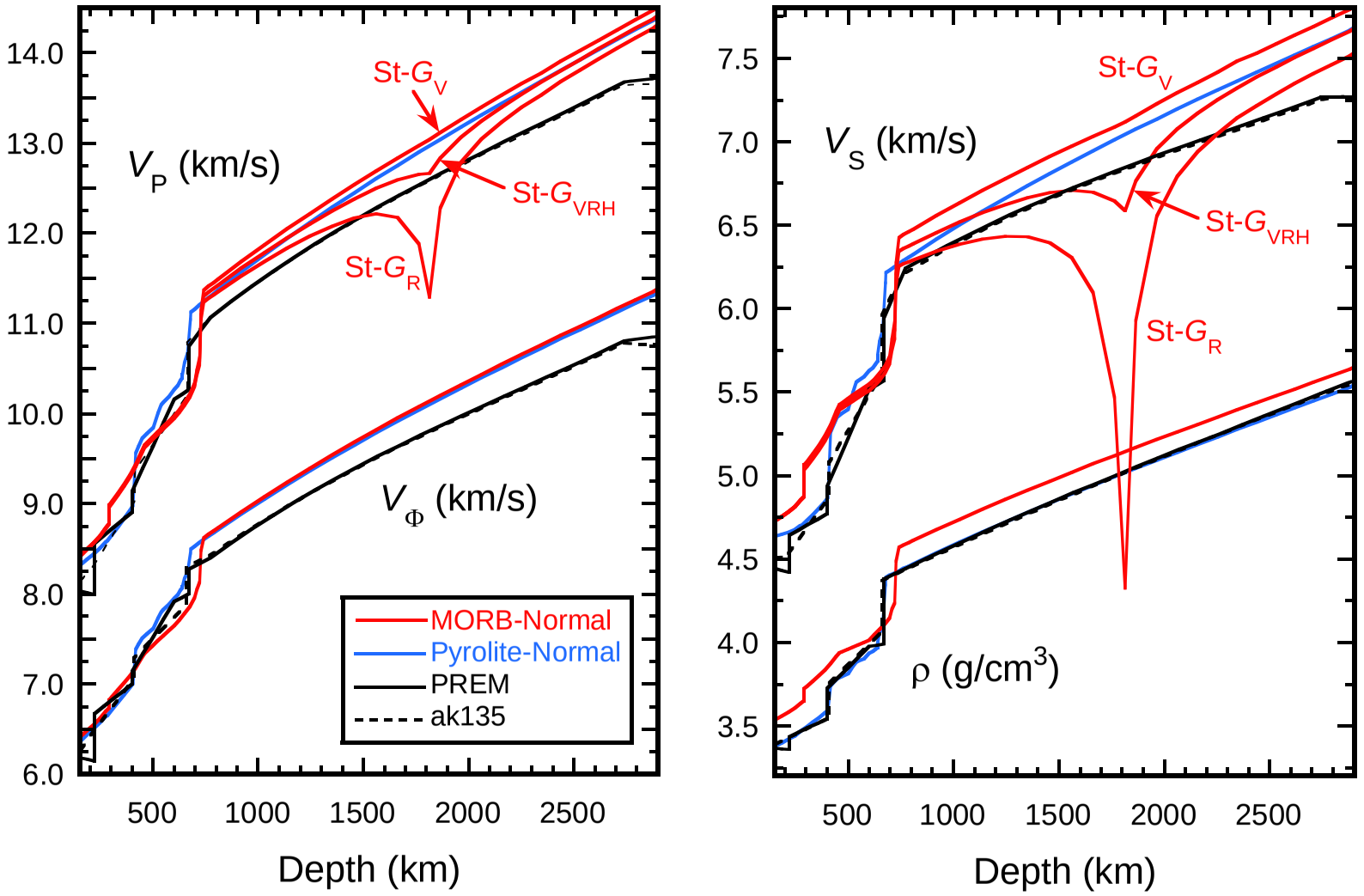

Fig. 4-12. Calculated density and seismic velocities of MORB and pyrolite to 2900 km depth along the normal geotherm. V_P and V_S of MORB are calculated by using VRH average (St-G_{VRH}), Voigt bound (St-G_V) and Reuss bound (St-G_R) of sher modulus of stishovite. Seismic models (PREM; Dziewonski and Anderson, 1981, ak135; Kennett et al., 1995) are also shown for comparison.

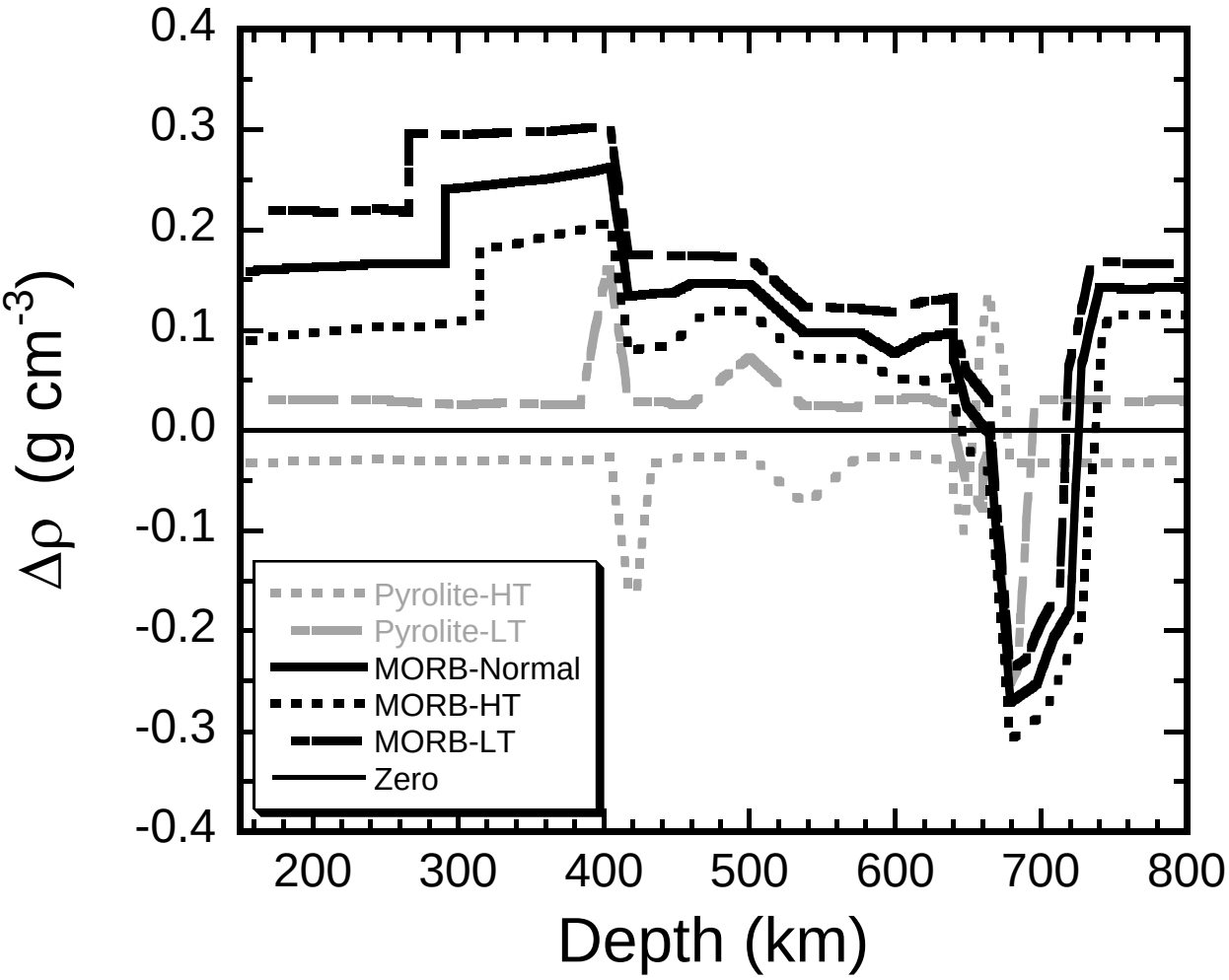

Fig. 4-13. Density differences relative to pyrolite along the normal geotherm. Black and gray lines are MORB and pyrolite, respectively. Solid, dotted and dasshed dotted lines are along the normal, HT and LT geotherms, respectively.

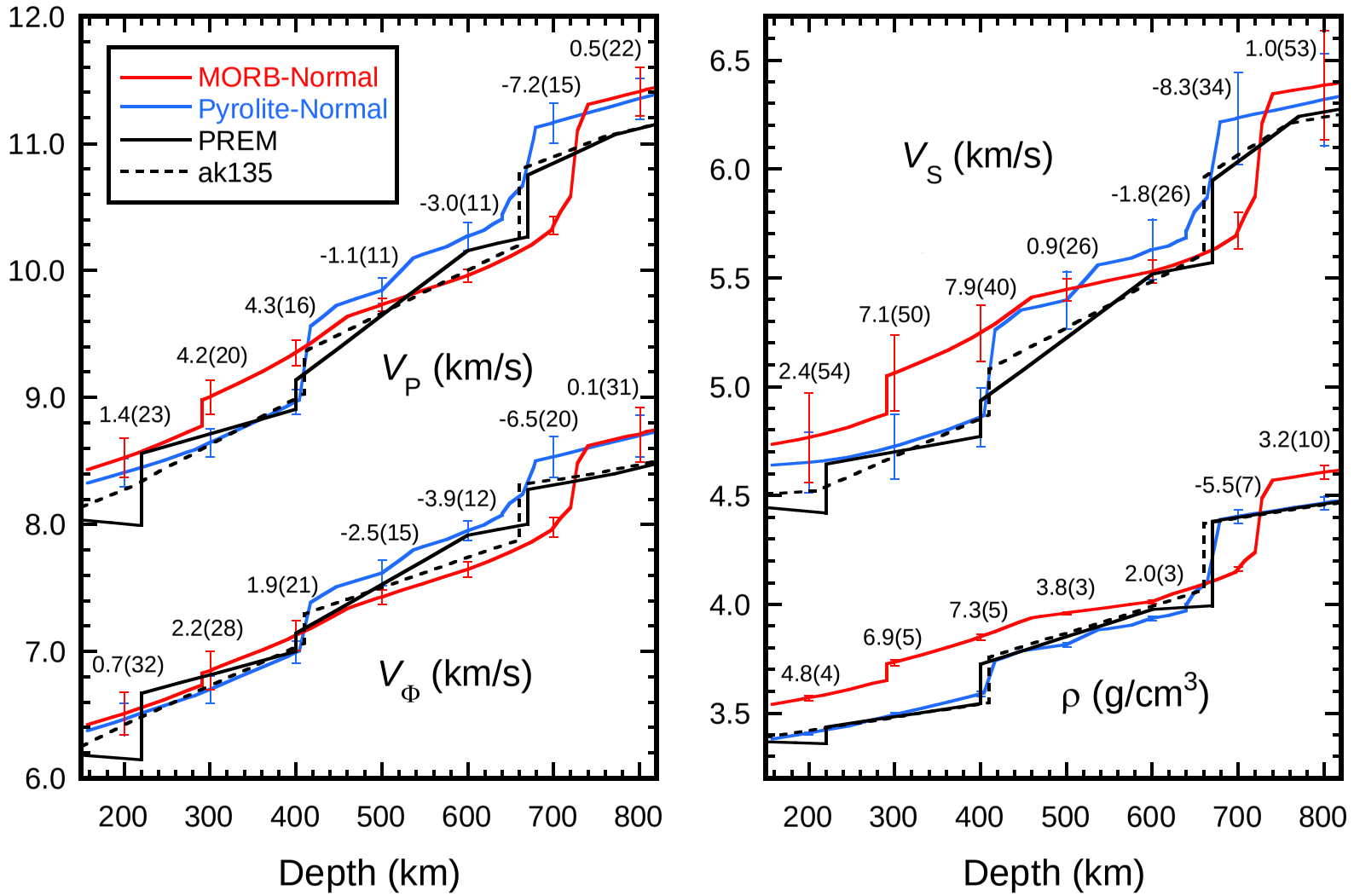

Fig. 4-14. Calculated density and seismic velocities of MORB and pyrolite along the normal geotherm to upper most part of the lower mantle with estimated uncertainties (error bars). Numbers are differences of the properties for MORB with pyrolite in %.

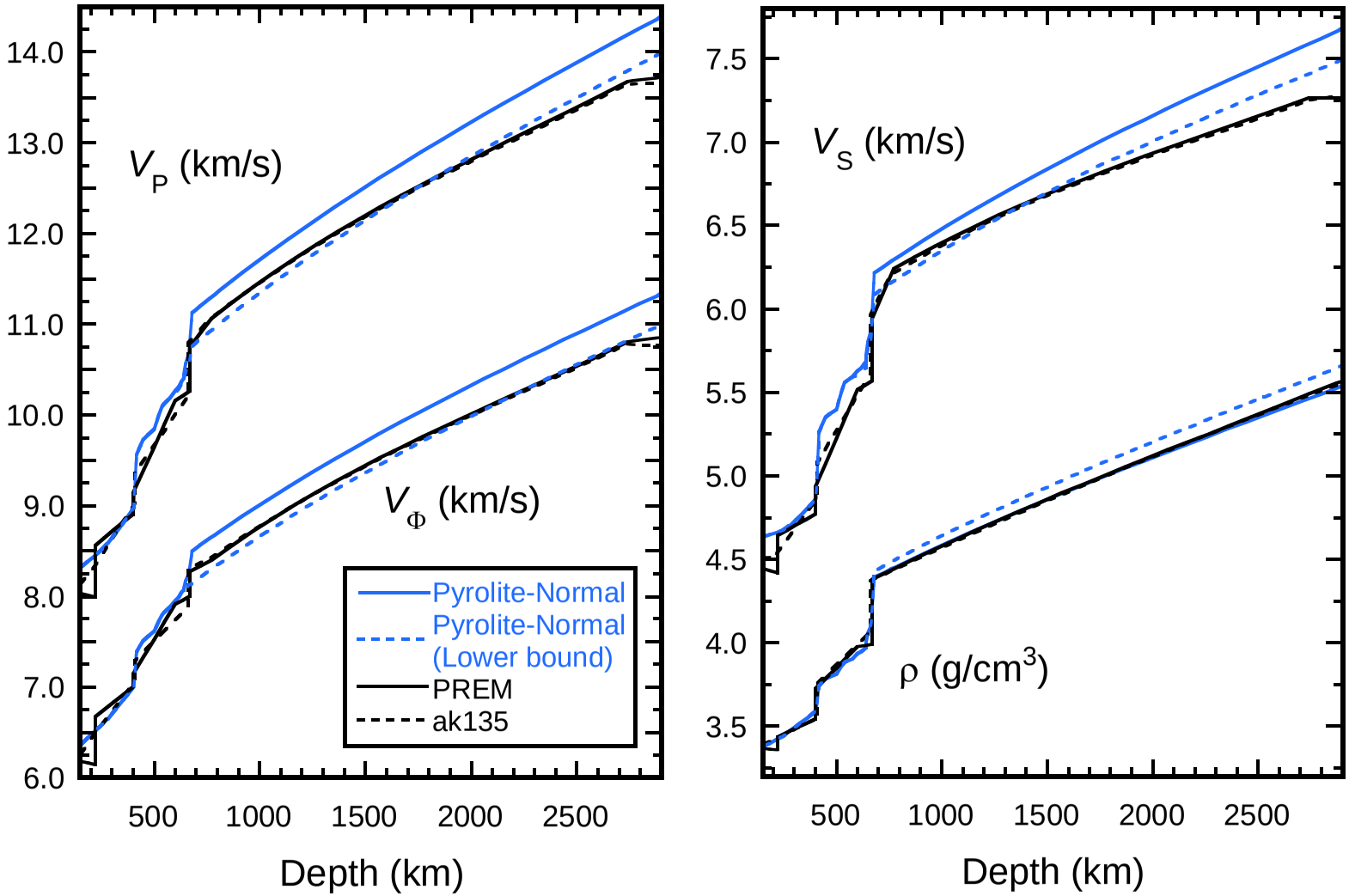

Fig. 4-15. Calculated density and seismic velocities of pyrolite to 2900 km depth along the normal geotherm. Solid blue lines are calculated from thermoelastic parameters listed in Table 4-2. Dashed bule lines are calculated from the lower elastic moduli for MgPv, Mw and CaPv by recent studies (see text). Seismic models (PREM; Dziewonski and Anderson, 1981, ak135; Kennett et al., 1995) are also shown for comparison.

Appendix
Technical aspects in determination of thermal equation of state

A-1 Techniques of *P-V-T* experiments

Experiments on omphacite with MAX-III (Chapter 1)

In Chapter 1, the *P-V-T* experiments of omphacite were carried out using the synthetic sample. Fig. A-1 shows back scattered electron image of the sample omphacite coexisting with garnet and coesite. The coexistence of these minerals is also observed by X-ray diffraction pattern (Fig. 1-2). Because of the overlaps of the diffraction peaks from omphacite and the coexisting minerals, the number of available peaks for the lattice parameter calculation is limited to be 8–11. Table A-1 shows an example of lattice parameter analyses. The number of used peaks is not enough to constrain the lattice parameters of a monoclinic symmetry mineral accurately, and the error for *a*, *b*, *c* and β is estimated to be relatively large (Table1-3 and A-1).

Fig. A-2 shows pressure-versus-load curve for MAX-III in our experiments (Chapter 1). Pressure increases linearly with increasing load up to 80 ton. The separate two experiments (Run#1 and #2) show very consistent results in terms of pressure generation. The generated pressures are consistent with the results of a run using 4 mm straight sintered diamond anvils by Wang et al. (1998a). The temperature-electric power relationship of the Run#1 at various loads is shown in Fig. A-3. It is recognized from the figure that, at given power, temperature decreases slightly with increasing load.

Experiments with SPEED-1500 (Chapter 2 and 3)

In Chapter 2 and 3, we used newly developed high-pressure cell assembly for *P-V-T* experiments (Fig. 2-1 and 3-1). Fig. A-4 shows back scattered electron image of the recovered

cell assembly. From this figure, it is clear that a thermocouple is placed vertically and the samples and pressure marker are placed horizontally. The new high-pressure design enables us to observe two or more samples even when the anvil gap is extremely narrowed.

Table A-2 and A-3 show examples of lattice parameter analyses on $(Mg_{0.91}Fe_{0.09})_2SiO_4$ ringwoodite and MORB majorite, respectively. In these analyses, observed and calculated values of *d*-spacing are very consistent for every diffraction peak, and the calculated lattice parameters are estimated to be very accurate.

We used NaCl and MgO capsules for *P*-*V*-*T* experiments with SPEED-1500 apparatus, but we have also tested BN capsule with the high-pressure cell assembly shown in Fig. 2-1. The low yield strength and the high symmetry of hexagonal BN (hBN) is suitable for the capsule for *P*-*V*-*T* experiments (e.g. Zhao et al., 1997; Nishihara et al., 2003; Chapter 1). Because of its kinetic property, the hBN can persist at further out of their thermodynamic stability field (e.g. Solozhenko, 1995). The testing experiment using the hBN capsule with the conditions of P = ~20 GPa, T = 1200°C and t = 1 hour was carried out. The micro-focused X-ray diffraction analysis on the recovered cell showed that hBN transformed to wurtzitic BN (wBN), which is the dense polymorph of BN with no thermodynamic stability field (e.g. Solozhenko, 1995). It was found that the wBN is very hard and difficult to be polished flatly. Then, the large yield strength of wBN is suggested. This may cause large non-hydrostatic stress in the sample within the BN capsule, and the BN capsule is considered to be unsuitable for our *P*-*V*-*T* experiments up to ~20 GPa and ~1000°C.

Fig. A-5 shows pressure-versus-load curve for SPEED-1500 in our experiments (Chapter 2 and 3). Pressure increases linearly with increasing load up to ~500 ton, and above this load the efficiency of pressure generation gradually becomes lower. The generated pressures are consistent with those by Kuroda et al. (2000), who used the same apparatus (SPEED-1500), the same size of truncation (3 mm) and different pressure medium [MgO, (Mg,Co)O] with us.

We used both TiC + diamond (1:1 in weight ratio) and WC + diamond (39:15 in weight) disk heaters in our test experiments. The volume ratio of WC or TiC to diamond are adjusted to be same. We confirmed that TiC + diamond and WC + diamond heaters work well with similar heat efficiency at ~15 GPa and at least up to 1500°C and 1200°C, respectively. For *P-V-T* experiments, we adopted the TiC + diamond heater, which has been frequently used by some authors (e.g. Irifune et al., 1998). However, the TiC + diamond heater yields very low oxygen fugacity and often reduces FeO in the sample in the phase equilibrium experiments, and this problem is slightly improved by using the WC + diamond (N. Nishiyama, private communication). The use of WC + diamond heater may be the better choice for the experiments in the system including FeO. The temperature-electric power relationship of the experiment S648 (TiC + diamod heater, NaCl capsule) at various loads is shown in Fig. A-6. It is recognized from the figure that, at given power, temperature decreases significantly with increasing load.

A-2 Comparison of pressure scales of Au

Equation of state of Au is widely used as a pressure standard for in situ X-ray diffraction experiments (e.g. Funamori et al., 1996; Irifune et al., 1998; Chapter 2 and 3). However, it is well known that several reported equations of state of Au yield significant differences in the calculated value of pressure especially at high-temperatures (e.g. Funamori et al., 1996; Hirose et al., 2001). Because some important phase boundary of the mantle minerals are determined based on the Au pressure scale, the discrepancy of the equation of state of Au affects significantly the model for the Earth's interior (e.g. Irifune et al., 1998; Hirose et al., 2001). In the case of the equation of state study, the derived results are also largely affected from the difference of the pressure scale because the differences of calculated pressure by EOS of Au changes systematically (e.g. Funamori et al., 1996; Chapter 2 and 3). Therefore, we will present comparison of the calculated pressures and thermoelastic parameters of Au collected from the three EOSs of Au (Jamieson et

al., 1982; Anderson et al., 1989l; Shim et al., 2002). The comparison of derived thermoelastic parameters of ringwoodite based on the three pressure scales are also shown.

Anderson et al.'s (1989) pressure scale has been widely used for in situ X-ray diffraction experiments in the last decade (e.g. Meng et al., 1994; Funamori et al., 1996; Irifune et al., 1998; Fei, 1999). However, Anderson et al. derived the EOS based on the measured elastic and thermodynamic properties of Au at temperatures only less than 550 K, where the electronic contribution to thermal expansion is expected to be small. Moreover, it has been pointed out that calculated pressure using Anderson et al.'s scale yields large discrepancy between post-ringwoodite phase boundary of Mg_2SiO_4 based on the in situ X-ray observations (Irifune et al., 1998) and the observed 660 km seismic discontinuity (e.g. Shim et al., 2001; Chudinovskikh and Boehler, 2001, Matsui and Nishiyama, 2002).

On the other hand, Jamieson et al.'s (1982) scale based on shock wave data yields ~2 GPa higher pressure than Anderson et al.'s scale around *P-T* conditions corresponding to the 660 km depths (~23 GPa and ~1900 K) (Fig. A-7), and post-ringwoodite boundary of Mg_2SiO_4 become consistent with the seismic discontinuity (e.g. Ono et al., 2001; Hirose et al., 2001). Very recently, Shim et al. (2002) reported a new *P-V-T* equation of state of Au based on the inversion of recent quasi-hydrostatic compression (Takemura, 2001) and shock wave data. Fig. A-7 shows comparison of these pressure scales of Au, as the calculated pressure differences by Anderson et al. (1989) with Shim et al. (2002) and Jamieson et al. (1982).

We analyzed these three EOSs of Au by using frequently used formalisms of thermal equation of state (high-temperature Birch-Murnaghan EOS, thermal pressure EOS, Mie-Grüneisen-Debye EOS). The formalisms of these thermal EOS are described in elsewhere: high-temperature Birch-Murnaghan EOS (e.g. Funamori et al., 1996; Wang et al., 1998b; Chapter 1–3), thermal pressure EOS (e.g. Jackson and Rigden, 1996; Chapter 2), Mie-Grüneisen-Debye EOS (e.g. Jackson and Rigden, 1996). The results of analysis are indicated in Table A-4. It is clearly

seen that thermoelastic parameters are significantly different between the three EOSs of Au (Jamieson et al., 1982; Anderson et al., 1989; Shim et al., 2002). For example, for the pressure derivative of bulk modulus K'_T, Jamieson et al. (1982) yields the largest value, while Anderson et al. (1989) yields the smallest value, and the difference is as large as 1.

Obviously, these differences in thermoelastic parameters of Au affect the experimentally determined equation of state derived using Au as a pressure scale. We analyzed *P-V-T* data of $(Mg_{0.91}Fe_{0.09})_2SiO_4$ ringwoodite (Chapter 2) based on above three pressure scales of Au by using the three formalisms of thermal equation of state. The results are shown in Table A-5. The fixed Debye temperature θ_0 (904 K) is calculated from data by Weidner et al. (1984) (Poirier, 2000). As simply expected, the thermoelastic properties of ringwoodite directly correlate with the same thermoelastic properties of Au pressure standard (see Table A-4 and A-5).

From our data, we cannot judge which equation of state of Au is the most appropriate. Zha et al. (2000) measured both cell volume and sound velocity of MgO at high-pressures and room-temperature, and determined pressure directly without recourse to any prior pressure standard using the finite strain theory. Such measurement on Au at simultaneous high-pressure and high-temperature conditions may enable to derive accurate *P-V-T* equation of state of Au.

A-3 Comparison of the data derived using NaCl and MgO capsule

We employed NaCl and MgO capsules for *P-V-T* experiments using the SPEED-1500 apparatus at SPring-8 (Chapter 2 and 3). Because of their simple cubic symmetry, NaCl and MgO sample capsules do not yield serious overlap of X-ray diffraction lines from sample and capsule. Additionally, these materials are stable under relatively wide *P-T* conditions. Thus, these materials are widely used as the sample capsule for in situ X-ray observation using multi-anvil apparatus (e.g. Irifune et al., 1998; Wang et al., 1998b). Because NaCl is relatively soft (low yield strength), it is known that non-hydrostatic stress is effectively released by heating at relatively

low temperatures (~700 K) (Weidner et al., 1994). However, MgO is a relatively strong (high yield strength) material (e.g. Weidner et al., 1994), and high temperature is required to release non-hydrostatic stress in MgO. This property of MgO may affects accuracy of the *P*-*V*-*T* data when MgO is used for the sample capsule. Therefore, from the consistency of derived *P*-*V*-*T* data, we observed the effect of macroscopic differential stress in the sample within NaCl and MgO capsules.

Figs. A-8 and A-9 show the comparisons of *P*-*V*-*T* data of $(Mg_{0.91}Fe_{0.09})_2SiO_4$ ringwoodite and MORB majorite, respectively, collected using NaCl and MgO capsules. In these figures, the isotherms, those are calculated from the thermoelastic parameters preferred in Chapter 2 and 3, are shown. The data collected with NaCl capsule after heating to 873 and 1073 K are in reasonably good agreement, and the data collected at same temperature are fitted well by a single smooth line (Figs. A-8a, A-9a). On the other hand, the data collected with MgO capsule show significant deviations, and only the data collected after heating to 1273 K, which is the highest temperature in our experiments, show good agreement with the data with NaCl capsule (Figs. A-8b, A-9b). This probably means, in the case of MgO capsule, heating below 1273 K is insufficient to release macroscopic differential stress in the sample. This is generally consistent with the stress analysis of polycrystalline MgO at 8 GPa and high-temperatures by Weidner et al. (1994). We used Au as a pressure standard, which is characterized by very low yield strength. Then, we regarded that the determined pressure is free from the effect of macroscopic differential stress.

Most data collected with MgO capsule after heating to 873 and 1073 K shift to higher cell volume relative to preferred compression curves (Figs. A-8b, A-9b). This suggests that vertical stress component is larger than horizontal components in the sample (a horizontal goniometer is used for X-ray diffraction). Some data of majorite collected after heating to 873 K slightly shift to lower cell volume relative to preferred compression curves (Fig. A-9b). This is possibly due to

the stress heterogeneity between ringwoodite and majorite, or the microscopic deviatric stress caused by the inter-grain friction in the sample.

Because we used powdered sample for *P-V-T* experiments, the microscopic deviatric stress may be present in the sample. It is well known that the microscopic deviatric stress can be detected from the full-width-at-half-maximum (FWHM) of X-ray diffraction peaks (e.g. Weidner et al., 1994; Li et al., 1996). We investgated the FWHM of ringwoodite at various *P-T* conditions.

Fig. A-10 shows FWHM of X-ray diffraction peaks (311 and 440) of $(Mg_{0.91}Fe_{0.09})_2SiO_4$ ringwoodite against temperature. Plotted data are collected from X-ray diffraction patterns used for a thermal EOS analysis in Chapter 2. It is clearly seen that FWHM of the data collected after heating to 873 K is systematically larger than those after heating to 1073 and 1273 K and those at ambient condition. This suggests that the ringwoodite after heating at 873 K is still under the condition of the microscopic deviatric stress. The deviation of the *P-V-T* data (Fig. 2-4) may be partly due to this microscopic deviatric stress.

No systematic difference is detected between data obtained by using NaCl and MgO capsules. One datum at ambient condition shows relatively large FWHM compared to other data at ambient condition (Fig. A-10). This datum was collected after decompression of run S649, in which maximum heating temperature is 873 K. The large FWHM of the data may suggest that the microscopic deviatric stress still remains even at ambient condition. The FWHM of diffraction lines of Au is small and insensitive to the heating temperature suggesting that the microscopic deviatric stress in the pressure marker is extremely low.

References

Akella, J., Kennedy, G.C., 1971. Melting of gold, silver, and copper-proposal for a new high-pressure calibration scale. J. Geophys. Res. 76, 4969–4977.

Anderson, O.L., Isaak, D.G., Yamamoto, S., 1989. Anharmonicity and the equation of state for

gold. J. Appl. Phys. 65, 1534–1543.

Chudinovskikh, L., Boehler, R., 2001. High-pressure polymorphs of olivine and the 660-km seismic discontinuity. Nature 411, 574–577.

Fei, Y., 1999. Effects of temperature and composition on the bulk modulus of (Mg,Fe)O. Am. Mineral. 84, 272–276.

Funamori, N., Yagi, T., Utsumi, W., Kondo, T., Uchida, T., Funamori, M., 1996. Thermoelastic properties of $MgSiO_3$ perovskite determined by in situ X ray observations up to 30 GPa and 2000 K. J. Geophys. Res. 101, 8257–8269.

Hirose, K., Fei, Y., Ono, S., Yagi, T., Funakoshi, K., 2001. In situ measurements of the phase transition boundary in $Mg_3Al_2Si_3O_{12}$: implications for the nature of the seismic discontinuities in the Earth's mantle. Earth Planet. Sci. Lett. 184, 567–573.

Irifune, T., Nishiyama, N., Kuroda, K., Inoue, T., Isshiki, M., Utsumi, W., Funakoshi, K., Urakawa, S., Uchida, T., Katsura, T., Ohtaka, O., 1998. The postspinel phase boundary in Mg_2SiO_4 determined by in situ X-ray diffraction. Science 279, 1698–1700.

Jackson, I., Rigden, S.M., 1996. Analysis of P-V-T data: constraints on the thermoelastic properties of high-pressure minerals. Phys. Earth Planet. Int. 96, 85–112.

Jamieson, J.C., Fritz, J.N., Manghnani, M.H., 1982. Pressure measurement at high temperature in X-ray diffraction studies: gold as a primary standard. In: Akimoto, S., Manghnani, M.H. (Eds.), High-Pressure Research in Geophysics. CAPJ, Tokyo, pp. 27–48.

Kuroda, K., Irifune, T., Inoue, T., Nishiyama, N., Miyashita, M., Funakoshi, K., Utsumi, W., 2000. Determination of the phase boundary between ilmenite and perovskite in $MgSiO_3$ by in situ X-ray diffraction and quench experiments. Phys. Chem. Minerals 27, 523–532.

Li, B., Rigden, S.M., Liebermann, R.C., 1996. Elasticity of stishovite at high pressure. Phys. Earth Planet. Int. 96, 113–127.

Matsui, M., Nishiyama, N., 2002. Coparison between the Au and MgO pressure calibration

standards at high temperature. Geophys. Res. Lett. 29, 10.1029/2001GL014161.

Meng, Y., Fei, Y., Weidner, D.J., Gwanmesia, G.D., Hu, J., 1994. Hydrostatic compression of γ-Mg_2SiO_4 to mantle pressures and 700 K: thermal equation of state and related thermoelastic properties. Phys. Chem. Minerals 21, 407–412.

Nishihara, Y., Takahashi, E., Matsukage, K., Kikegawa, T., 2003. Thermal equation of state of omphacite. Am. Mineral. 88, 80–86.

Ono, S., Katsura, T., Ito, E., Kanzaki, M., Yoneda, A., Walter, M.J., Urakawa, S., Utsumi, W., Funakoshi, K., 2001. In situ observation of ilmenite-perovskite phase transition in $MgSiO_3$

Poirier, J.P., 2000. Introduction to the physics of the Earth's interior. Cambridge University Press, Cambridge.

Shim, S.-H., Duffy, T.S., Shen, G., 2001. The post-spinel transformation in Mg_2SiO_4 and its relation to the 660-km seismic discontiniuty. Nature 411, 571–574.

Shim, S.-H., Duffy, T.S., Takemura, K., 2002. Equation of state of gold and its application to the phase boundaries near 660 km depth in Earth's mantle. Earth Planet. Sci. Lett. 203, 729–739.

Solozhenko, V.L., 1995. Boron nitride phase diagram: state of the art. High Pres. Res. 13, 199–214.

Wang, Y., Getting, I.C., Weidner, D.J., Vaughan, M.T., 1998a. Performance of tapered anvils in a DIA-type, cubic-anvil, high-pressure apparatus for X ray diffraction studies. In: Manghnani, M.H., Yagi, T. (Eds.), Properties of Earth and Planetary Materials at High Pressure and Temperature. Am. Geophys. Union, Washington, DC, pp. 35–39.

Wang, Y., Weidner, D.J., Zhang, J., Gwanmesia, G.D., Liebermann, R.C., 1998b. Thermal equation of state of garnets along the pyrope-majorite join. Phys. Earth Planet. Int. 105, 59–71.

Weidner, D.J., Sawamoto, H., Sasaki, S., Kumazawa, M., 1984. Single-crystal elastic properties

of the spinel phase of Mg_2SiO_4. J. Geophys. Res. 89, 7852-7860.

Weidner, D.J., Wang, Y., Vaughan, M.T., 1994. Yield strength at high pressure and temperature. Geophys. Res. Lett. 21, 753–756.

Zha, C.-S., Mao, H.-K., Hemley, R.J., 2000. Elasticity of MgO and a primary pressure scale to 55 GPa. Proc. Natl. Acad. Sci. USA 97, 13494–13499.

Zhao, Y., Von Dreele, R.B., Shankland, T.J., Weidner, D.J., Zhang, J., Wang, Y., Gasparik, T., 1997. Thermoelastic equation of state of jadeite $NaAlSi_2O_6$: An energy-dispersive Rietveld refinement study of low symmetry and multiple diffraction. Geophys. Res. Lett. 24, 5–8.

Table A-1.
An example of observed and calculated d-spacings of omphacite at 10.15 GPa and 1000 K

h	k	l	d_{obs} (Å)	d_{calc} (Å)	Δd (Å)
1	1	0	6.2208	6.2293	-0.0085
0	2	0	4.2926	4.2950	-0.0024
0	2	1	3.2408	3.2401	0.0007
2	2	0	3.1149	3.1147	0.0002
$\overline{2}$	2	1	2.8970	2.8988	-0.0018
$\overline{3}$	1	0	2.8474	2.8454	0.0020
0	4	1	1.9698	1.9692	0.0006
5	1	0	1.7706	1.7705	0.0001
$\overline{1}$	5	0	1.6877	1.6878	-0.0002
5	3	1	1.3719	1.3720	-0.0001

The corresponding spectrum is given in Fig. 1-2. d_{obs} is obseved d-spacing. d_{calc} is calculated d-spacing based on the lattice parameters [a = 9.425(3) Å, b = 8.590(2) Å, c = 5.142(5) Å, β = 106.29(4)º].

Table A-2.
An example of observed and calculated d-spacings of $(Mg_{0.91}Fe_{0.09})_2SiO_4$ ringwoodite at 21.16 GPa and 1073 K

h	k	l	d_{obs} (Å)	d_{calc} (Å)	Δd (Å)
2	2	0	2.7837	2.7844	0.0008
3	1	1	2.3736	2.3740	0.0004
4	0	0	1.9681	1.9684	0.0003
4	2	2	1.6070	1.6074	0.0003
5	1	1	1.5148	1.5148	0.0000
4	4	0	1.3912	1.3910	-0.0002

The corresponding spectrum is given in Fig. 2-2. d_{obs} is obseved d-spacing. d_{calc} is calculated d-spacing based on the lattice parameter [a = 7.8712(6) Å].

Table A-3.
An example of observed and calculated d-spacings of MORB majorite at 21.16 GPa and 1073 K

h	k	l	d_{obs} (Å)	d_{calc} (Å)	Δd (Å)
4	0	0	2.8259	2.8263	0.0004
3	3	2	2.4102	2.4108	0.0006
6	1	1	1.8330	1.8326	-0.0004
4	4	4	1.6314	1.6315	0.0001
6	4	0	1.5673	1.5673	0.0000

The corresponding spectrum is given in Fig. 3-2. d_{obs} is obseved d-spacing. d_{calc} is calculated d-spacing based on the lattice parameters [a = 11.3019(7) Å].

Table A-4

Thermoelastic parameters of Au derived from three different fromalisms of thermal EOS

Parameter	Anderson	Shim	Jamieson
K_{T0} (GPa)	166(1)	167(1)	167(1)
K'_T	5.5(1)	5.0(1)	5.9(1)
High-temperature Birch-Murnaghan equation of state			
$(\partial K_T/\partial T)_P$ (GPa K^{-1})	–0.044	–0.033	–0.041
$\alpha = a + bT$			
a (10^{-5} K^{-1})	3.2	3.7	4.0
b (10^{-8} K^{-2})	2.3	1.3	1.6
Thermal pressure equation of state			
α_0 (10^{-5} K^{-1})	4.28	4.26	4.66
$(\partial K_T/\partial T)_V$ (GPa K^{-1})	–0.011	0.000	0.000
$(\partial^2 P/\partial T^2)_P$ (10^{-7} GPa K^{-2})	0.00	0.46	–0.25
Mie-Grüneisen-Debye equation of state			
γ_0	2.93	2.93	3.19
q	2.7	1.0	1.0
θ_0 (K)	[170]	[170]	[170]

Equations of state of Au are from Jamieson et al. (1982), Anderson et al. (1989) and Shim et al. (2002). Square brackets indicate fixed value in the calculation. Number in brackets are deviation in K_{T0} and K'_T by using three different formulas of thermal equation of state.

Table A-5
Thermoelastic parameters of $(Mg_{0.91}Fe_{0.09})_2SiO_4$ derived from three different formalisms of thermal EOS

Parameter	Anderson	Shim	Jamieson
K_{T0} (GPa)	[187]	[187]	[187]
K'_T	4.3(1)	4.0(1)	4.9(1)
High-temperature Birch-Murnaghan equation of state			
$(\partial K_T/\partial T)_P$ (GPa K^{-1})	–0.028(5)	–0.015(5)	–0.026(5)
$\alpha = a + bT$			
a (10^{-5} K^{-1})	1.9(2)	2.1(2)	2.3(2)
b (10^{-8} K^{-2})	1.2(4)	0.7(4)	1.1(4)
Thermal pressure equation of state			
α_0 (10^{-5} K^{-1})	2.48(14)	2.44(14)	2.81(14)
$(\partial K_T/\partial T)_V$ (GPa K^{-1})	–0.006(4)	0.006(4)	0.003(4)
$(\partial^2 P/\partial T^2)_P$ (10^{-7} GPa K^{-2})	[0]	[0]	[0]
Mie-Grüneisen-Debye equation of state			
γ_0	1.13(3)	1.30(3)	1.43(3)
q	[1.0]	[1.0]	[1.0]
θ_0 (K)	[904]	[904]	[904]

P-V-T data are from Chapter 2. Pressure scales are Jamieson et al. (1982), Anderson et al. (1989) and Shim et al. (2002). Square brackets indicate fixed value in the calculation. Number in brackets for K'_T denotes deviation by using three different formulas of thermal equation of state.

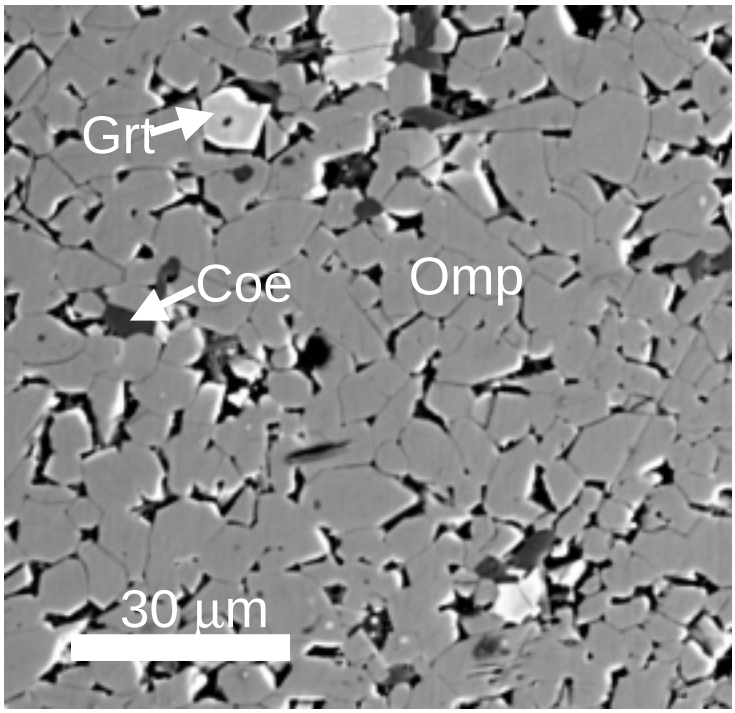

Fig. A-1. Back scattered electron image of the starting material for the P-V-T experiments (Chapter 1). Omphacite (Omp) and small amount of garnet (Grt) and coesite (Coe) are detected.

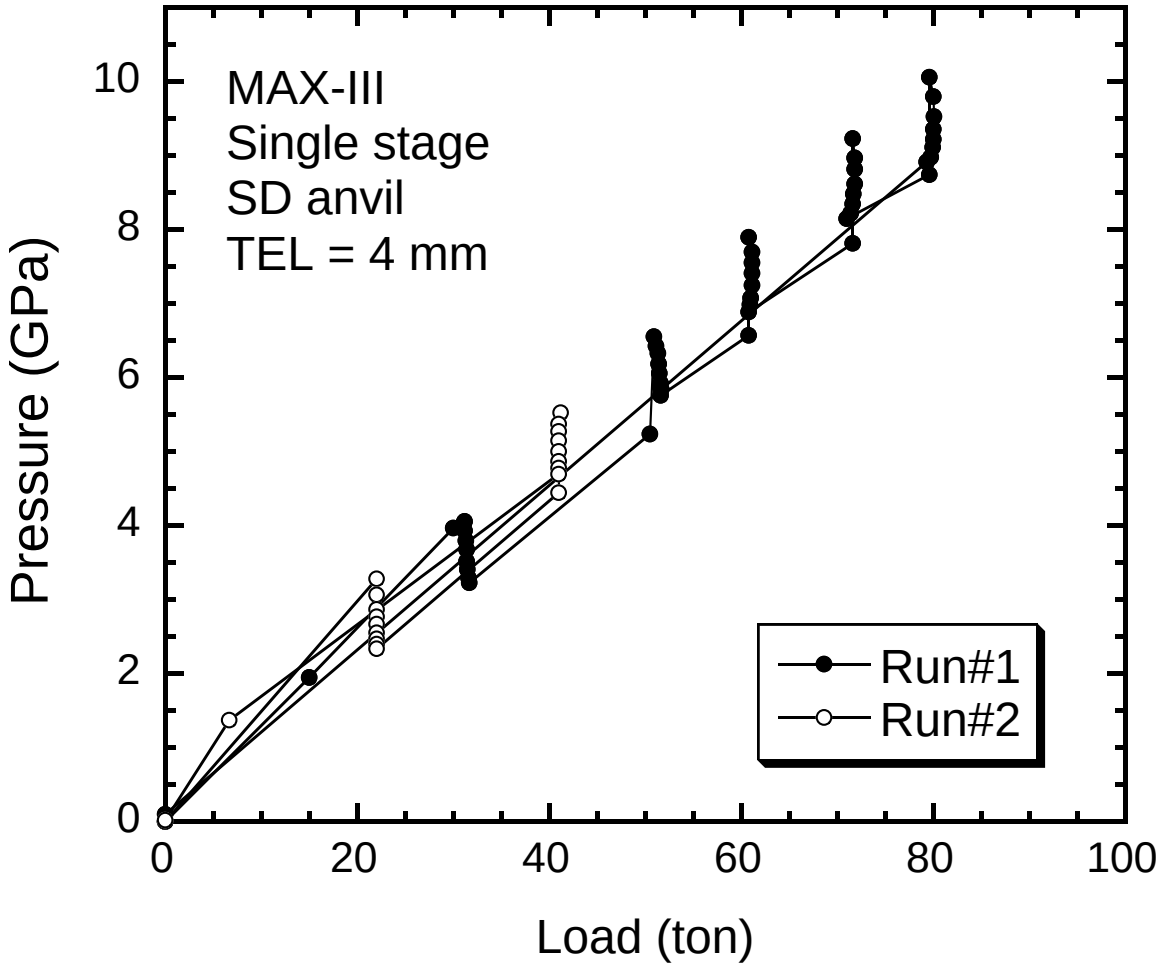

Fig. A-2. Pressure versus ram load for MAX-III with the cell used in chapter 1 (Fig. 1-1). Sintered diamond anvils with 4 mm truncation edge length are used. Data are same as those of Table 1-3 and Fig. 1-3.

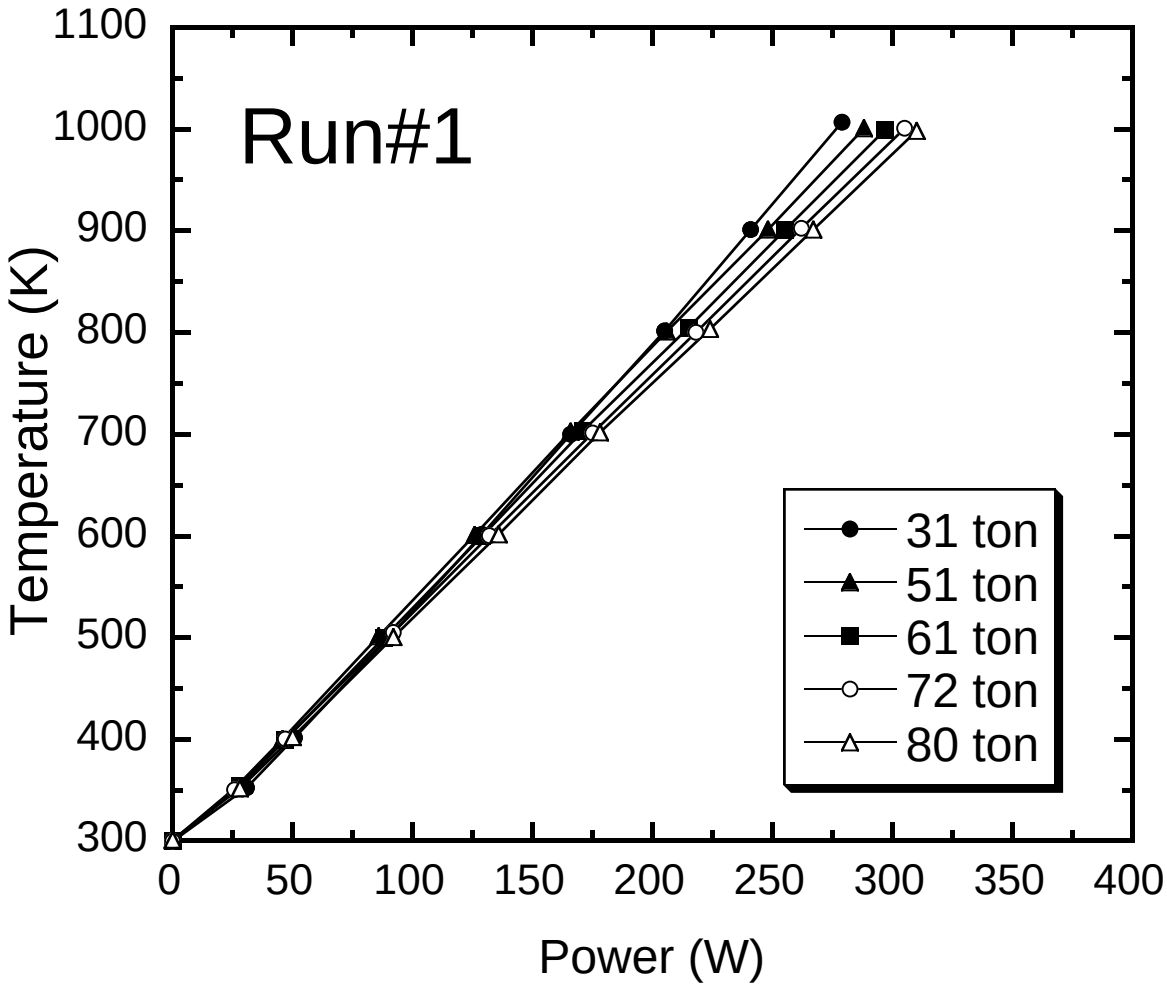

Fig. A-3. The temperature-power relationship of the Run#1 at various loads (31, 51, 61, 72 and 80 ton; see Fig. A-2).

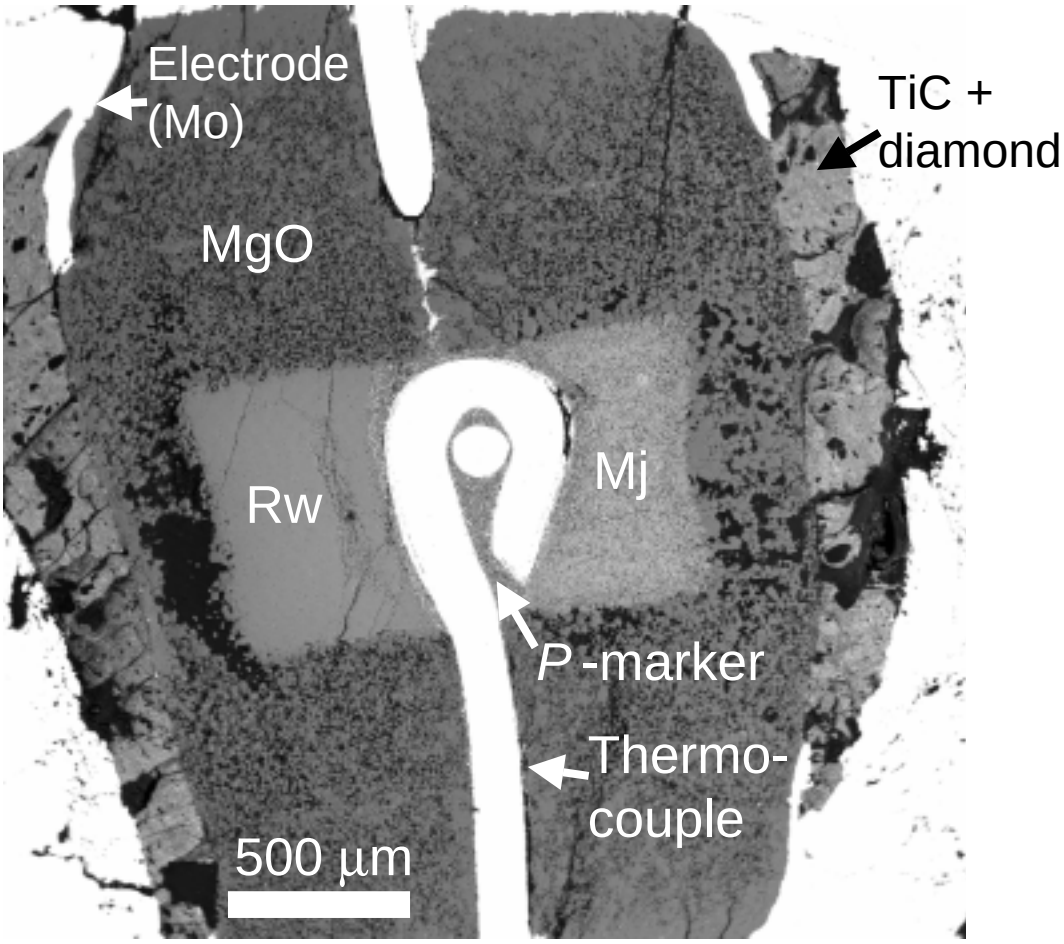

Fig. A-4. Back scattered electron image of the high-pressure cell assembly for the P-V-T experiments with MgO capsules (Chapter 2 and 3).

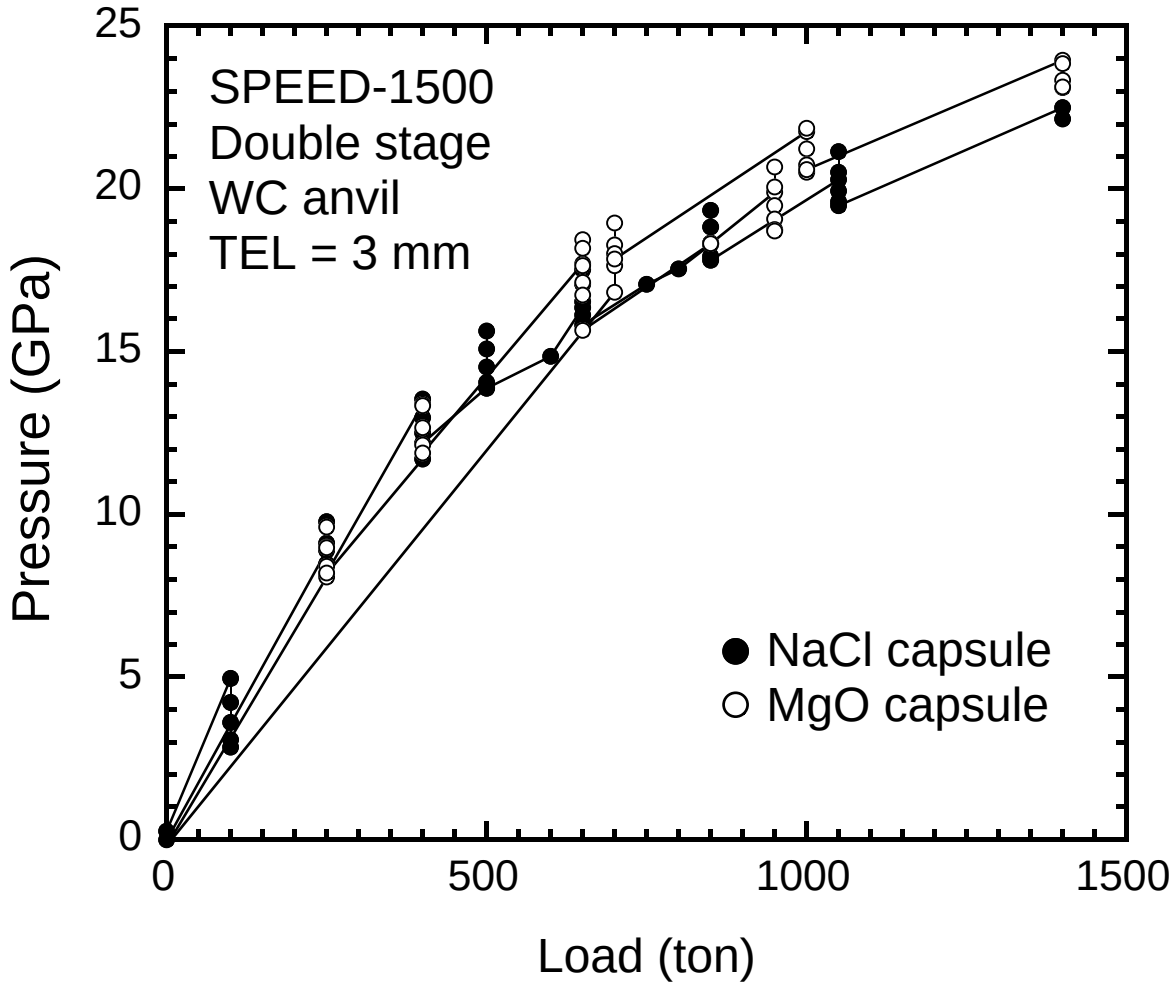

Fig. A-5. Pressure versus ram load for SPEED-1500 with the cell used in chapter 2 and 3 (Fig. 2-1). WC anvils with 3 mm truncation edge length are used. Data collected in the loading paths are plotted. Solid and open circles are data collected with NaCl abd MgO capsules, respectively.

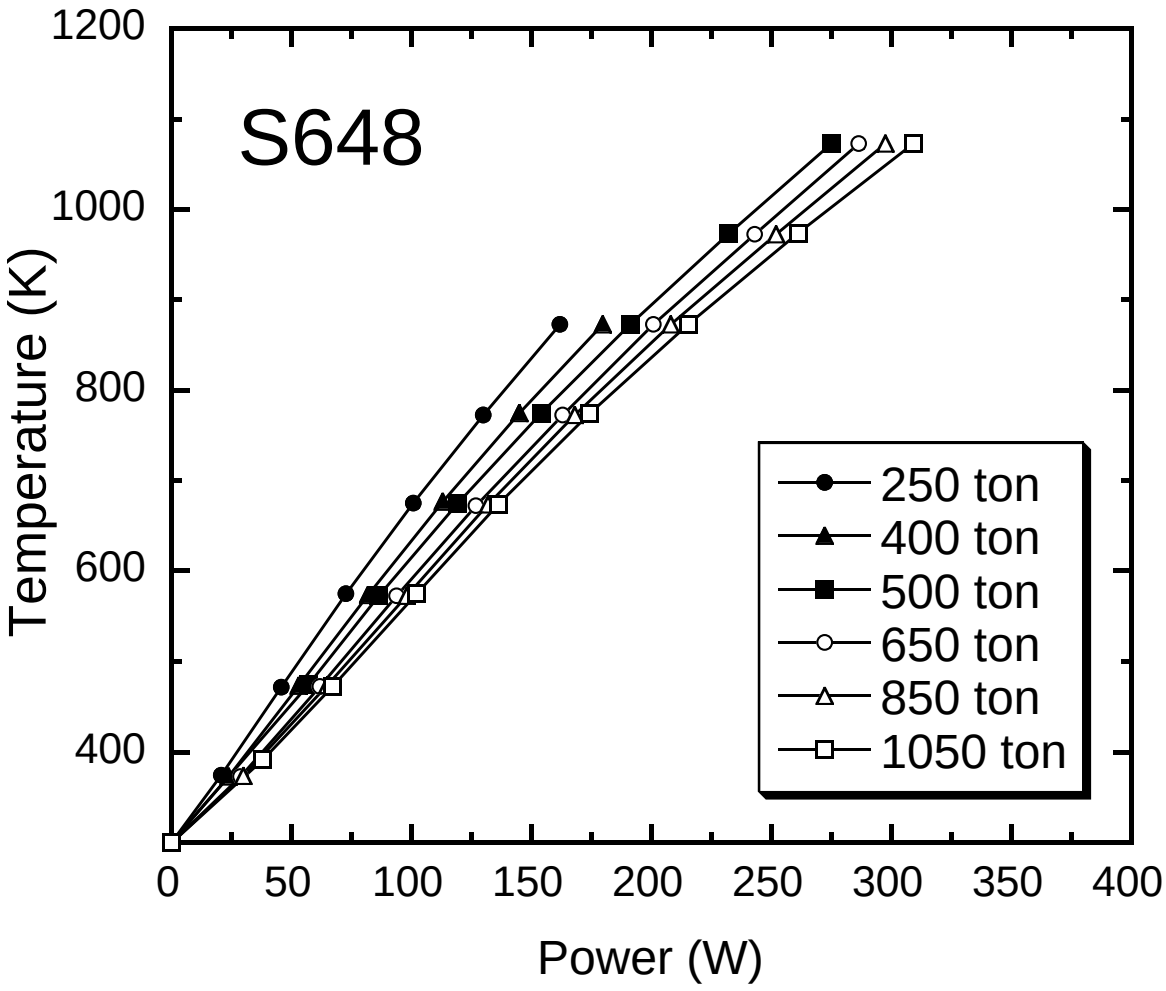

Fig. A-6. The temperature-power relationship of the experiment S648 at various loads (250, 400, 500, 650, 850 and 1050 ton).

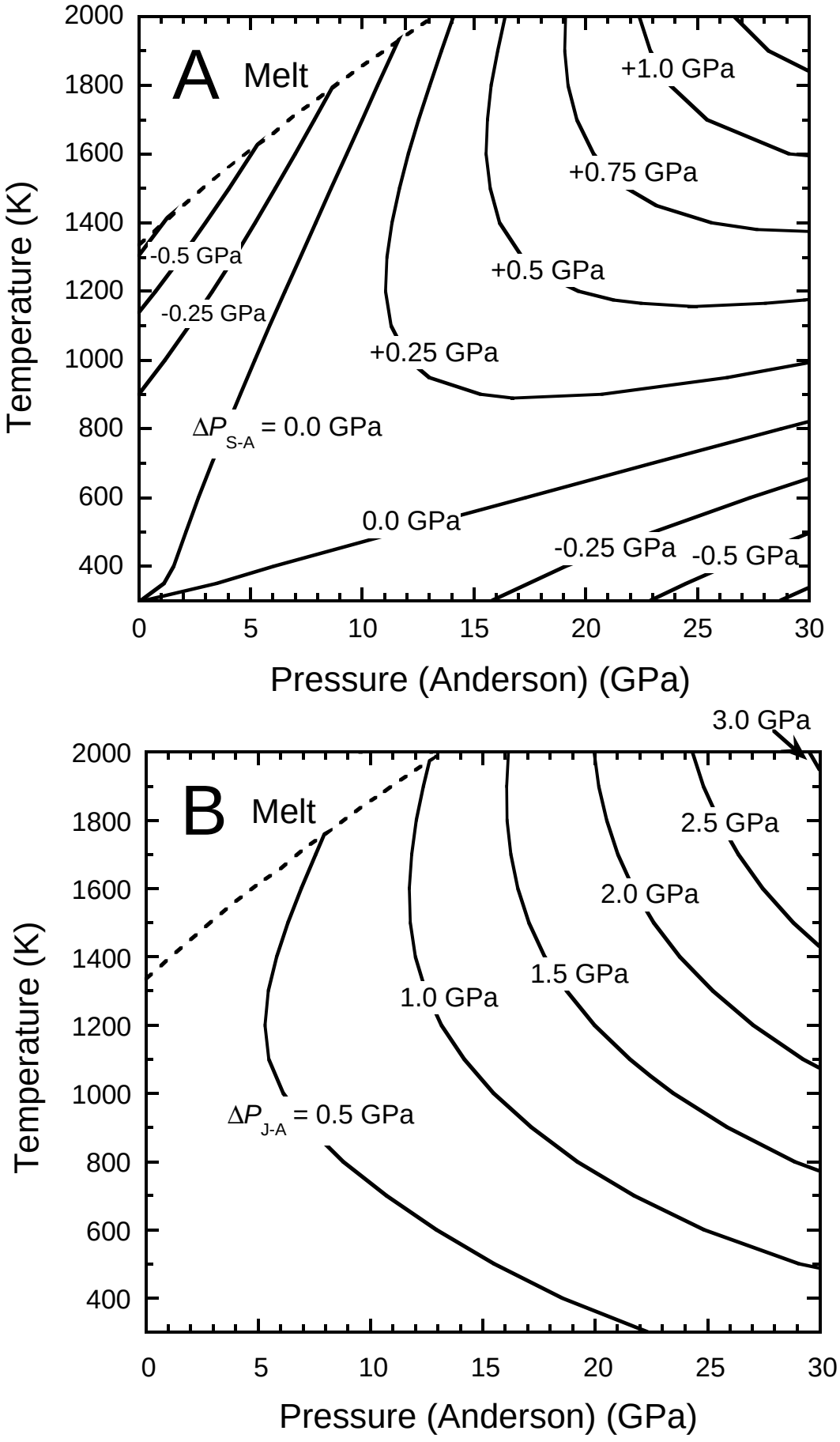

Fig. A-7. Pressure differences calculated from the EOS of Au by Anderson et al. (1989) with (a) Shim et al. (2002) and (b) Jamieson et al. (1982). Melting cureves are (dashed lines) from Akella and Kennedy (1971).

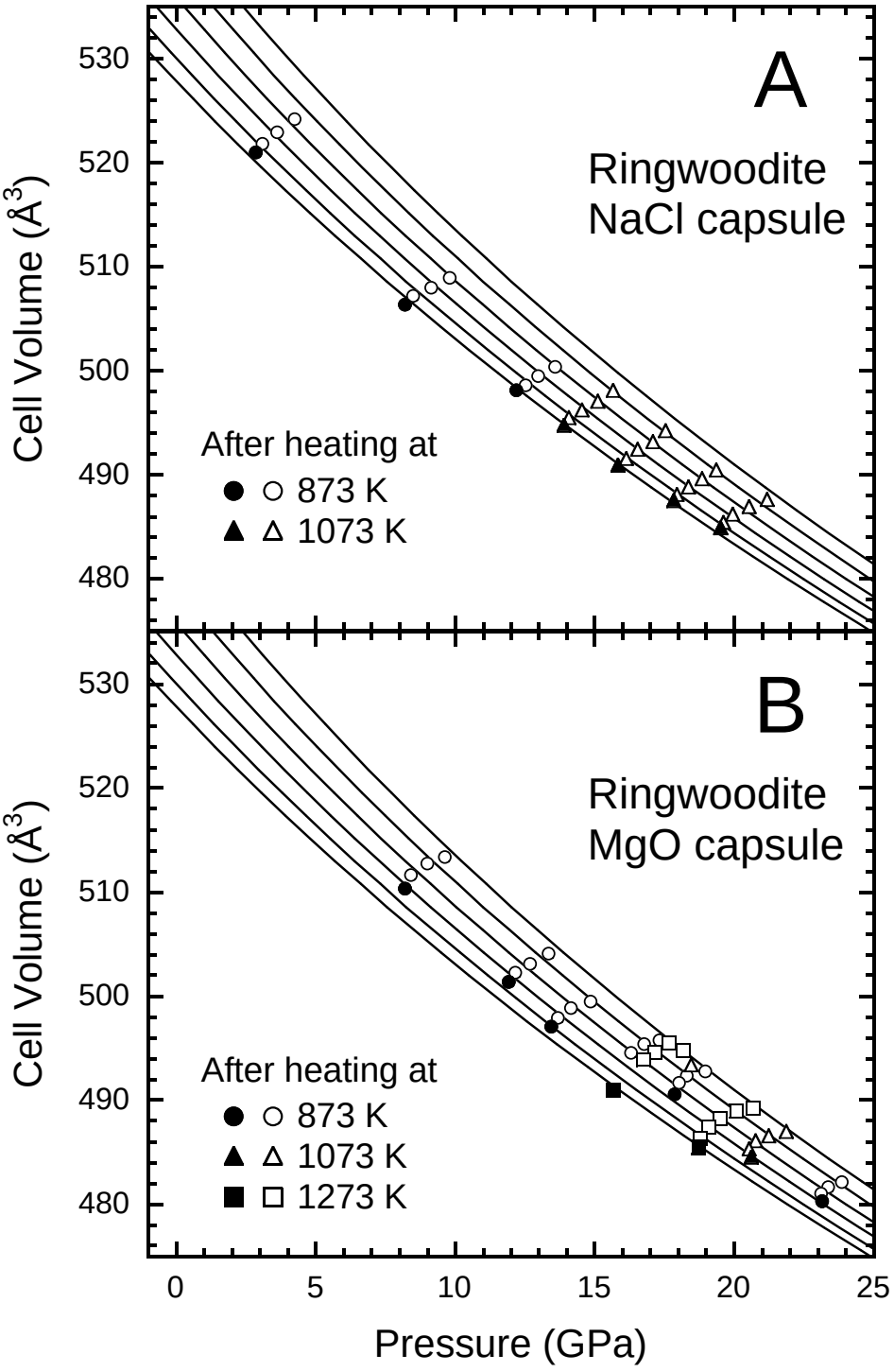

Fig. A-8. Comparison of *P-V-T* data of ringwoodite collected using different capsule materials (a; NaCl capsule, b; MgO capsule) and collected after heating at different temperatures. Circles, triangles and squares are data collected after heating at 873, 1073 and 1273 K, respectively. Solid symbols are data at 300 K. Isotherms (300, 473, 673, 873, 1073 and 1273 K), indicated as solid lines, are calculated from thermoelastic parameters derived with fixed value of K_{T0}= 187 GPa (Table 2-2).

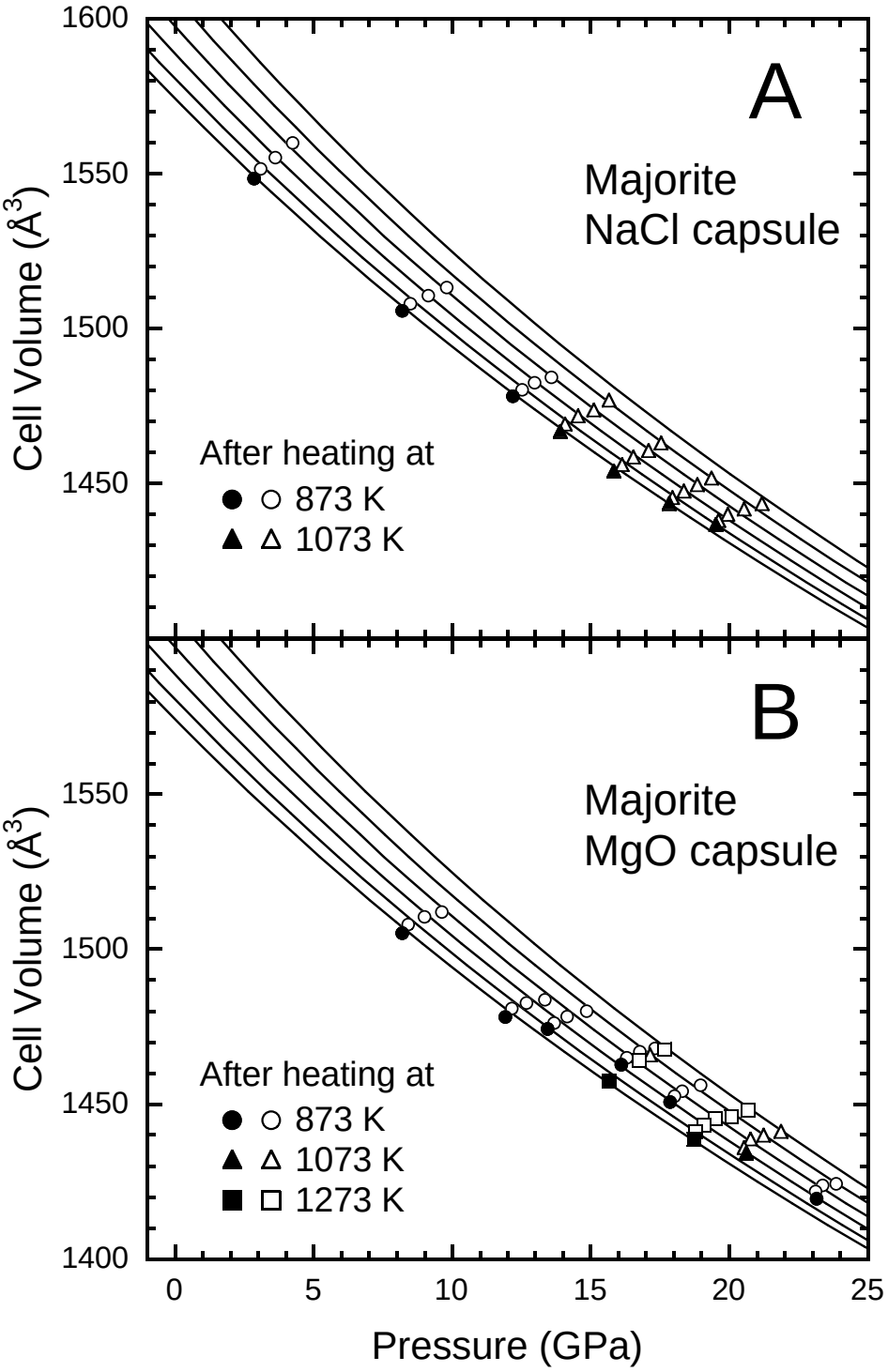

Fig. A-9. Comparison of *P-V-T* data of majorite collected using different capsule materials (a; NaCl capsule, b; MgO capsule) and collected after heating at different temperatures. Circles, triangles and squares are data collected after heating at 873, 1073 and 1273 K, respectively. Solid symbols are data at 300 K. Isotherms (300, 473, 673, 873, 1073 and 1273 K), indicated as solid lines, are calculated from thermoelastic parameters derived with fixed value of $K' = 4$ (Table 3-4).